Optical tools towards the improvement of optogenetic stimulation

Maddalena, L.

DOI
10.4233/uuid:b7f2378b-01df-48f0-b71d-089f17b7b378

Publication date
2022

Document Version
Final published version

Citation (APA)
Maddalena, L. (2022). *Optical tools towards the improvement of optogenetic stimulation*. [Dissertation (TU Delft), Delft University of Technology]. https://doi.org/10.4233/uuid:b7f2378b-01df-48f0-b71d-089f17b7b378

Optical tools towards the improvement of optogenetic stimulation

Optical tools towards the improvement of optogenetic stimulation

Proefschrift

ter verkrijging van de graad van doctor
aan de Technische Universiteit Delft,
op gezag van de Rector Magnificus prof.dr.ir T.H.J.J. van der Hagen,
voorzitter van het College voor Promoties,
in het openbaar te verdedigen op 14 november 2022 om 10.00 uur

door

Laura Maddalena

Master of Science in Physics,
Università La Sapienza di Roma, Italie
geboren te Teramo, Italie.

Dit proefschrift is goedgekeurd door de promotor:

promotor: Dr. ir. Jacob P. Hoogenboom
copromotor: Dr. Elizabeth C.M. Carroll

Samenstelling promotiecommissie:

Rector Magnificus,	voorzitter
Dr. ir. J. P. Hoogenboom,	Technische Universiteit Delft
Dr. E. C. M. Carroll,	Technische Universiteit Delft

Onafhankelijke leden:

Prof. dr. S. Shoham,	NYU Langone Health
Prof. dr. V. Emiliani,	Institut de la Vision
Dr. N. Bhattacharya,	Technische Universiteit Delft
Prof. dr. S. Stallinga,	Technische Universiteit Delft
Prof. dr. B. Rieger,	Technische Universiteit Delft

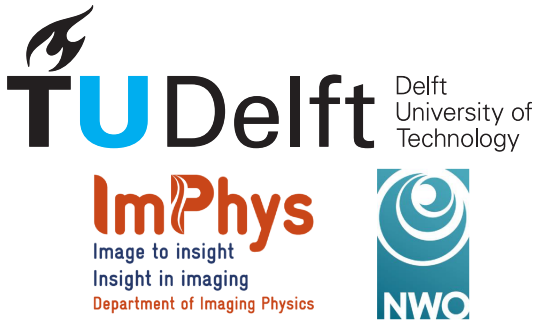

Keywords: Optogenetics, computer generated holography, adaptive optics, light-tissue interactions, microscopy.

Printed by: Ridderprint | www.ridderprint.nl.

Front & Back: Artistic representation of a fish silhouette made of light.

Cover design by Francesca Colella

ISBN 978-94-6384-380-5

An electronic version of this dissertation is available at
http://repository.tudelft.nl/.

Try this lens.
Depths of air.
Excellent! And now!
Light, just light making everything below it a toy world.
Very well, we'll make the glasses accordingly.

Dippold the Optician, Spoon river anthology. Edgar Lee Masters.

Non più ottico ma spacciatore di lenti
Per improvvisare occhi contenti
Perché le pupille abituate a copiare
Inventino i mondi sui quali guardare

Un ottico, Non al denaro non all'amore né al cielo. Fabrizio De André.

Contents

Acronyms

CGH computer generated holography 9

2PE two-photon excitation 8

1PE one-photon excitation 8

2D two dimensional 7

3D three dimensional 7

TPEF two-photon excited fluorescence 52

ROI region of interest 28

GECI genetically encoded calcium indicator 4

LCoS liquid crystal on silicon 33

NIR near infrared 8

SLM spatial light modulator 9

NA numerical aperture 8

FEP fluorinated ethylene propylene 33

dpf days past fertilization 39

PSF point spread function 29

1

Introduction

1.1. All-optical study of physiology in living animals

Since Luigi Galvani in the late XVIII century explored the possibility to stimulate the sciatic nerve of a frog with electricity, scientists have been motivated to investigate the organization and signaling of the brain. Later, during the XX century, modern electrophysiology became the standard technique to study brain activity. Electrophysiology permits an experimenter to read the activity of a single neuron or of hundreds neurons within a complex circuit by recording the electrical signal generated by the ions flux across cells membranes. The electrical signal is directly measured via metal or glass electrodes put in close contact with the circuit of interest. This working principle makes electrophysiology an invasive approach while ensuring a measurement with good signal to noise ratio that is independent from any signal transduction [1].

With the advent of optogenetics in the late 1990s, interrogation of neural circuits became possible with light. Optogenetics relies on genetically encoded proteins that can act as actuators to transduce an optical signal into a physiological perturbation of a living cell *in vitro* or in a living animal. The physiological change can then be measured via genetically-encoded reporters that translate the presence of signaling molecules into an optical signal [2]. The genetic component permits to investigate specific cell types, while the optical component offers exquisite spatial resolution and the possibility to simultaneously activate multiple light-sensitive molecules at different wavelengths [3].

In neuroscience, optogenetic actuators are typically light-gated ion channels that, upon light irradiation, cause the depolarization or hyperpolarization of the plasma membrane of the neuron compared to the resting potential. In the first case, the transmembrane protein becomes permeable to cations and may induce a sub-threshold or supra-threshold action potential. An example in this category

Parts of this chapter are based on the work: *Holographic two-photon activation for synthetic optogenetics.* Nature Protocols **14**, 864–900, (2019)

of actuators is the microbial opsin Channelrhodopsin-2 (ChR2) [4]. On the other hand, the neuron can be hyperpolarized by transmembrane anion pumps, such as the family of Halorhodopsins, activated by another color of light. In this case, the induced physiological consequence is neuronal silencing, namely the inhibition of action potential. [5].

The advancement in the development of actuators and reporters, together with the ability to shine and record the light from the neurons expressing such tools, has allowed researchers to perform *"all-optical physiology"* experiments. Here, both manipulation and monitoring of neural activity are realized through light, making the investigation of the brain physiology in living animals less invasive than via the use of electrodes.

1.1.1. Overview on fluorescent reporters of neuronal function

To monitor the physiological response consequent to the stimulation of a cell, a wide variety of fluorescent sensors have been developed. In general, genetically-encoded reporters of neural activity can be classified in three main categories: genetically encoded calcium indicators (GECIs), genetically-encoded voltage indicators (GEVIs) and genetically-encoded neurotransmitters indicators (GENIs) [6].

GECIs

The first category of reporters relies on sensing the concentration of free calcium (Ca^{2+}). When an action potential is generated, voltage-gated calcium channels open up and cause an increase in calcium concentration within the cytoplasm from 50-100 nM up to 10 μM [7]. Hence, cytosolic Ca^{2+} concentration is a good proxy for neuronal activity because it reports the local Ca^{2+} inflow in shafts and dendritic spines triggered by synaptic activity [8] .

In the late nineties genetically encoded calcium indicator (GECI)s were based on FRET (Foster resonance energy transfer), they exploited the energy transfer between the cyan fluorescent protein (CFP) and the yellow fluorescent protein (YFP) mediated by the Ca^{2+} dependent conformational changes of the complex calmodulin (CaM) - M13 peptide. Cytoplasmic Ca^{2+} binds to CaM that wraps around the M13 peptide and causes the increase of FRET efficiency between CFP and YFP [9].

Later single-fluorophore GECIs were developed to permit Ca^{2+} imaging via conventional fluorescence microscopy. Among GECIs, the single-wavelength family of GCaMPs was widely developed. GCaMPs have three protein domains: calmodulin (CaM), a circularly permuted green fluorescent protein (cpGFP) and a peptide commonly M13 interacting with the calcium-binding protein. Upon Ca^{2+} binding to CaM, this protein interacts with the peptide domain, leading to a conformational change. This change modulates the chromophore inside the cpGFP barrel to promote a highly-fluorescent state [10]. The major limitation of this category of GECIs is their slow kinetics to track action potentials that propagate with timescales of milliseconds. In fact, GCaMPs fluorescence rise-times, at 50% of the total signal detected, is on the order of 100 ms. Improvement on the kinetic properties were achieved with the advent of the GCaMP6 [11] and GCaMP7 [12] families of sensors. Their fast variants have a rise time of 50 ms, however they suffer of decreased sen-

sitivity compared to their slow counterparts since sensitivity and speed are inversely proportional properties [13]. However, among the GCaMPs progeny the GCaMP6 family is one of the most used reporters for functional imaging *in vivo* thanks to brightness and limited photobleaching [14, 15].

The interrogation of complex neural networks among different neuronal ensembles required the extension of the available single-fluorophore GECI. To fill this gap red-shifted GECIs were engineered. They exhibit reduced phototoxicity, lower background signal and advantages linked to intrinsic properties of red-shifted wavelengths such as reduced absorption and scattering through tissue [8].

Overall the main constraint of single-wavelength GECI is their limited kinetic response which is inadequate to resolve fast dynamics of individual neurons with spike rates in the interval 10-100 Hz. In the last years progress was made with the advent of the multicolor XCaMPs [10] family which has still a response 3-4 time slower than endogenous calcium spikes. More recently other promising tools as the jGCaMP8 family was engineered, it offers a faster kinetic response and decay time than the green variants of the XCaMP family [13].

GEVIs

Differently, GEVIs reveal via fluorescence emission changes in the membrane potential of the the cell. Most GEVIs are either fluorescent proteins fused to voltage-sensing domain or are modified versions of microbial rhodopsins that exhibit voltage-sensitive fluorescence. Chemogenetic GEVIs are instead another category of GEVIs combining chemical and genetic indicators together [16]. Altogether, GEVIs represent the most direct measurement of neural electrical activity. However, voltage imaging is more challenging than calcium imaging through GCaMPs since it requires kilohertz (kHz) imaging rate due to the sub-millisecond time scale of the changes in membrane potential during an action potential. Moreover, GEVIs are typically localized on the plasma membrane, requiring bright and stable indicators [17]. Notably, GEVIs, differently than GECIs, enable the read out of sub-threshold activity [18].

GENIs

GENIs directly sense neurotransmitters and report their presence via a fluorescent signal. Neurotransmitters are the chemical messengers released by the pre-synaptic neuron via vesicle exocytosis. Neurotransmitters, reaching a concentrations in the micromolar range within the synaptic cleft [19], bind specific receptors located at the plasma membrane where they trigger in post-synaptic neurons either second messenger signaling cascades or ion flux. GENIs usually use either periplasmic-binding proteins (PBPs) or G-protein-coupled receptors (GPCRs) as the domain to bind the neurotransmitter [20]. Upon ligand binding, both PBP and GPCR domains undergo conformational changes that modulate the emission of the fluorescent protein within the sensors. Among the PBP sensors, iGluSnFR reported glutamate transients in different living animals such as zebrafish, C. elegans and mouse. However, the decay time of this sensor (92 ms) hindered to resolve local glutamate release upon electrical stimulation faster than 10 Hz. For such a reason improved versions

of the sensor were engineered namely SF-iGluSnFRs with the ability to report glutamate release during single action potential stimulated at high frequency (100 Hz) [6]. To date, PBP-based glutamate and GABA sensors and GPCR-based sensors for dopamine, serotonin, acetylcholine and norepinephrine are available [6].

1.1.2. Overview on optogenetic actuators

Since the advent of optogenetics, a plethora of actuators to optically manipulate neural activity has been developed. These actuators can be classified in three broad categories: purely genetic, chemical and synthetic tools.

Pure genetics tools

Genetic tools refer to intrinsically light-gated ion channels that become selectively permeable to specific ions upon irradiation. This property allows to mimic the endogenous electrical activity in the neurons of interest. These genetically-encoded tools make use of endogenous chromophores synthesized by other biological system such as microbes or animal. Among these, the light-gated channel ChR-2, a trans-membrane protein from the algae *Chlamydomonas reinhardtii*, is an example of light-activated ion channel. When the opsin absorbs blue light, the retinal cofactor undergoes photoisomerization, inducing changes in the trans-membrane protein to pass an ionic current [21]. Hence, these opsin-based proteins have been introduced into neurons to mimic an action potential firing.

Chemical tools

Chemical tools rely on photosensitive reagents that react with endogenous receptors and channels. This approach allows to control any neuron expressing the receptor of interest. The use of photosensitive reagents that do not require an exogenous protein component is sometimes called photopharmacology. Examples of such reagents are caged neurotransmitters and designer photoswitches that interact with endogenous proteins. These are typically diffusible compounds introduced to cell by bath application or injected into the cell. Some of the most widely used photopharmacology tools are caged neurotransmitters. These tools have a photosensitive molecule that is removed upon light illumination, allowing the uncaged ligand to bind a receptor. A crucial property for successful caged compounds is the non-blocking behavior towards their target receptor. One of the most widely used caged compounds is the two-photon (2P) sensitive caged glutamate MNI-glutamate. It allows the user to release the neurotransmitter focally, e.g. to mimic synaptic release. This probe was extensively employed to study synaptic plasticity in various brain areas [22, 23].

Synthetic tools

This hybrid approach combines the advantages of photochemical control with the specificity of genetics and they enable to control neural activity in specific cells and at specific receptors. A synthetic photosensitive ligand is attached onto a genetically engineered protein to allow activation or inhibition of that particular protein with light. An example is the combination of functionalized azobenzenes with a

genetically-modified receptor designed to bind the photoswitch. For instance, the receptor ion gated channel can be modified with a single cysteine substitution on its extracellular side, near the binding site for the ligand. The ligand is bound to the chemical photoswitch, an azobenzene designed to be complementary to the engineered receptor. With a cysteine reactive group, namely a maleimide, it irreversibly tethers to the cysteine residue on the receptor. This approach combines the specificity given by genetic modifications with the unique precision to control with light the function of targeted neurons at the molecular level [24].

1.1.3. Milestones of all-optical study of physiology

The optogenetics toolkit, with both actuators and reporters, is a powerful addition to the spectrum of techniques available in neuroscience to investigate neurophysiology and unravel how neural circuit structure is related to circuit function. A plethora of actuators and reporters are available to respectively trigger and read out action potentials in living animals. The approach used in these experiments is to selectively photostimulate cell bodies expressing genetically encoded photosensitive channels (e.g., channelrhodopsins [14]) and record the consequent neural activity with fluorescent sensors [25]. All-optical physiology experiments have also required progress in optical engineering to be able to stimulate and record neural signals within the same instrument. A brief overview of the milestones archived over the last decade follows.

In 2007, Nikolenko and colleagues [26] reported the first example of all-optical interrogation of neural circuits by uncaging MNI-glutamate in mouse brain slices while recording the activation of dendritic spines and cortical neurons via calcium imaging. In those experiments, both the uncaging and the calcium imaging were performed with two-photon excitation. Later in 2014, Szabo *et al.* [27], activated with blue light ChR-2 expressed in cerebellar interneurons of a living mouse and concurrently recorded neural activity via fluorescence imaging of genetically-encoded GCaMP5-G expressed in the same cellular population. The activation of the optogenetics actuator and the delivery of the imaging light was here realized through a fiberscope attached to the mouse skull. This configuration allowed to manipulate and monitor the neural activity while the animal was freely behaving.

At same time two different research groups [28, 29] worked towards a similar experiment where both activation and imaging were performed with two-photon light. Packer *et al.* [29] activated in spiral fashion a red-shifted opsin while recording the activity via a GECI expressed in the same neuronal population of a head fixed mouse living mouse. Rickgauer and colleagues [28] accomplished the same experiment adopting a scanning approach to stimulate the neurons of interest. While both approaches exploited the axial confinement and deepest penetration depth intrinsic to two-photon excitation, the animals were not free to move.

In the following years different research groups contributed to the field of all-optical interrogation of either two dimensional (2D) or three dimensional (3D) neural circuits [30, 31], [32–34]. Dal Maschio and colleagues [33] integrated into a two-photon scanning microscope a module for parallel stimulation in 3D. This instrument allows to identify behavior-related neural circuits in awake zebrafish larvae.

The stimulation was targeted to single somata with a diameter of ~6 μm and axial resolution of ~9 μm over a volume of ~160 x 80 x 32 μm. A similar instrument was proposed by McRaven *et al.* [35] to achieve comparable lateral and axial resolution. In this case the goal was to discover cellular-level motifs in living zebrafish embryos. To date, optogenetics has allowed remote control of neural activity in living and awake animals at different scales from single cell signaling, including complex networks of neurons till the investigation of animals behaviours [3]. The ability of investigating physiology at different scales permitted to use optogenetics to answer both fundamental questions about the brain working principle and both specific questions related to diseases in animal models [36].

1.2. Optical methods for cellular stimulation

Shaping the stimulation light is necessary to precisely target actuators, particularly in densely labeled samples where one wishes to excite only a subset of expressing cells. Initially wide field one-photon excitation (1PE) was used to activate ion channels and pumps both *in vitro* [37] and *in vivo* [38]. However, 1PE is inadequate for optogenetic stimulation with single-cell resolution in thick living tissue given the poor axial resolution in thick, highly scattering tissues and limited penetration depth of visible wavelengths. For such reasons two-photon excitation (2PE) is preferred due to its intrinsic axial confinement and increased penetration depth of longer wavelengths that are less sensitive to scattering and absorption by endogenous molecules. To this end, ultrashort pulses near infrared (NIR), such as those emitted by mode-locked Ti:Sapphire lasers, usually used for two-photon microscopy, are employed.

Light patterning has been realized with different approaches that can be distinguished in two broad categories: sequential and parallel.

Sequential illumination relies on galvanometric mirrors, resonant scanners or acousto-optical deflectors to scan the beam across the stimulation target. Differently from glutamate uncaging, the photoactivation of actuators such as ChR-2 requires increasing the illumination area to a surface encompassing the soma of the neuron of interest because single diffraction limited 2P spots will not produce a depolarization that exceeds the action potential threshold [39]. To increase the efficiency of sequential approaches, the surface of the target cell is covered by the spiral scanning of a low numerical aperture (NA) beam as described in [40]. Here, Rickaguer and colleagues induced AP in cultured hippocampal neurons expressing ChR-2 with 30 ms temporal resolution. However, the time resolution of this approach is dependent on the number of stimulated cells and the number of scanned locations within each cell.

Parallel approaches overcome this limitation by simultaneously redirecting the stimulation light to multiple targets. Here the temporal resolution is independent from the number of stimulated cells [14]. These methods rely either on intensity or phase modulation of the light. In the first case, digital micromirror devices (DMDs) are used to selectively block the off-target light. So these devices are not compatible with 2PE given their low damage threshold and power efficiency [41]. As a consequence this strategy is inefficient in terms of power management. Differently,

computer generated holograms (CGHs) displayed onto spatial light modulator (SLM) allow to modulate the phase of the stimulation light at the back aperture of the objective. The objective performs then a Fourier transform, transforming the phase hologram into a focused pattern of light matching the targets in the sample. CGHs can target both diffraction-limited regions of interest (ROIs) or extended areas covering the neuronal soma or subcellular regions. Overall the temporal resolution of computer generated holography (CGH) optogenetics is limited by the actuator kinetics and the (SLM) refresh rate. This approach combined with 2P illumination, has proven effective for the activation of neurons expressing opsin both in brain slice [42] and in living animals [32, 33, 43]. A more sophisticated method to realize parallel stimulation is generalized phase contrast (GPC). This interferometric method uses an SLM addressed with a binary phase mask corresponding to the desired target intensity. The light reflected off the phase modulator passes then a lens, a phase contrast filter placed in the Fourier plane of the lens and finally a second lens that focuses the target intensity. The phase contrast filter applies a phase retardation between the on-axis component of the the light, representing the reference wave, and the higher-order spatial frequency components, containing the information about the phase of the target object. In this way the components interfere to produce at the focal plane of the second lens the desired target intensity [39].

Another strategy adopted to shape the stimulation light is represented by hybrid methods. Both SLM and scanning devices are used, the stimulation light is multiplexed via CGH and then it is scanned through galvo mirrors. As reported in [29, 34] hybrid approaches can successfully generate AP in living animals. To date, hybrid approaches were used to stimulate simultaneously more ROIs compared to purely parallel methods. Yang and colleagues [34] reported the concurrent stimulation of 80 neurons over 150 μm depth in the mouse visual cortex. Instead the highest number of cells simultaneously activated via purely parallel approaches is 50 [32].

1.2.1. Advantages and limitations of two-photon computer generated holography

In the work presented in this thesis, ultrashort pulses of NIR light were shaped with CGH. As noted above, this technique outperforms other patterning schemes such as intensity modulation through DMDs. Importantly, 1PE via DMDs cannot truly be confined in three dimensions and exhibits poor axial resolution, resulting in unwanted illumination of tissue outside the ROI. Owing to the nonlinear physics of multiphoton absorption, it is possible to achieve confined excitation in the geometrical focus where the light intensity is the highest. Two-photon computer generated holography (2P-CGH) provides a high level of flexibility, allowing the simultaneous excitation of multifocal point clouds, e.g. targeted to sub-cellular regions or to multiple somata. In 2P-CGH, the number of excited ROIs does not affect temporal resolution, which depends only on the stimulation time, the refresh rate of the SLM and the kinetics of the optogenetic tool.

Lasers typically used for 2PE are characterized by four parameters: wavelength,

pulse peak power (P_{peak}), repetition rate (f_{rep}), pulse duration (τ) and average power (P_{av}). These parameters play an important role in the light-tissue interaction and in the non-linear process underlying the stimulation. The excitation wavelength for both fixed-wavelength or tunable (eg. Ti:Sapphire) lasers needs to match the absorption spectra of the optogenetic actuator while minimizing any activation of the reporter to avoid any cross-talk between stimulation and imaging. The wavelengths used for 2P optogenetics activation lay typically in the interval 700-1100 nm which falls in the ”optical window for tissue” (600-1200 nm) where the endogenous absorbers such as melanin, hemoglobin and most importantly water show relatively low absorption. The main consequence is a reduced linear absorption of water which is responsible of heating effects on the sample [44]. The average power over time is determined by the following equation:

$$P_{av} = P_{peak} \cdot f_{rep} \cdot \tau \tag{1.1}$$

The available laser power could limit the number of ROIs that can be excited simultaneously, since CGH splits the average laser power among several focal spots, and the probability of 2PE (Π^{2PE}) drops quadratically with the average power [41]:

$$\Pi^{2PE} \propto \frac{P_{av}^2}{f_{rep} \cdot \tau} \tag{1.2}$$

Increasing the average power will increase the number of targets simultaneously activated while causing thermal heat and consequently thermal damage of the tissue [45, 46]. A reduced laser repetition rate could potentially mitigate the heating effect for two reasons. A lower repetition rate implies a longer time between consecutive pulses and this extra time might be beneficial for tissue to recover from thermal stress. Moreover, when lower repetition rates are associated with higher peak powers and lower average powers a more efficient stimulation of the actuator can be realized reducing the thermal damage caused by high average powers. However, decreasing the repetition rate comes at the expenses of non-linear damage which is proportional to the peak power. Non-linear damage arises from the non-linear interaction between the stimulation light and the tissue at the geometrical focus. This effect can lead to multi-photon ionization, cell ablation, optical breakdown and even plasma formation [47]. Non-linear absorption may also cause photochemical damage [44], such as DNA damage or formation of reactive oxygen species (ROS). Another parameter to consider in the design of a 2PE-CGH stimulation experiment is the intensity or power density namely the average power delivered per unit of area. The intensity of the stimulation is usually lower for extended CGH stimulation compared to sequential illumination because in the first case the irradiation light is distributed over a larger area. However, the simultaneous stimulation of multiple foci usually requires higher average powers compared to sequential approaches. These figures make parallel approaches more exposed to thermal damage than scanning methods where the average power is typically lower and the heat dissipation is more efficient due to the small excitation spot [46]. However, scanning approaches are more prone to induce nonlinear photodamage since the peak power

will be concentrated on a smaller area [41, 48]. In conclusion, the experimenter needs to carefully choose the laser parameters in order to minimize both linear and non-linear damage while preserving the efficiency of 2PE of the actuator of interest.

Another drawback of CGH targeting extended areas is the degradation of the axial confinement of the hologram as the lateral extent of the target pattern increases. This issue can be solved by combining CGH with temporal focusing. Temporal focusing (TF) is a light shaping technique capable of restoring the axial resolution of an holographic projection targeting an extended area. In fact, CGHs projected through a high-NA objective have their lateral extent scaling linearly with the axial extent [14]. TF relies on a diffraction grating conjugated to the sample plane to separate the femtosecond laser pulse into its spectral components. In the time domain, each spectral component has a longer duration until the focus where all the components constructively interfere at the focus and so the resulting beam transiently restores a shorter duration. The probability of excitation at the focal plane is enhanced inversely with the pulse duration τ:

$$\Pi^{2PE} \propto \frac{I_{av}^2}{\tau \cdot f_{rep}} \cdot \sigma^{2P} \tag{1.3}$$

where I_{av} is the average intensity, σ^{2P} is the cross-section of the excited molecule and f_{rep} is the laser repetition rate. By exploiting the inverse proportionality between Π^{2P} and τ, the 2PE response is further confined to a thin region around the focal plane, and the axial resolution is decoupled from the lateral resolution. As previously described [42, 49], TF can confine an arbitrary 2D target pattern up to 500 μm in diameter to cellular resolution along the z axis. Temporally focused 3D 2P-CGH has been achieved in several implementations. One design [50] uses a second SLM after the diffraction grating to control the axial displacement of temporally focused holographic patterns. Alternatively, Pégard *et al.* [51] developed a method called 3D scanless holographic optogenetics with TF (3D-SHOT). The stimulation light is first shaped into custom TF patterns by a spherical lens and a blazed diffraction grating, and then is passed through a 4f system with the SLM in the Fourier plane. The 3D-SHOT [51] enables 2PE stimulation of up to 50 neurons arbitrarily distributed over a large volume (550 × 550 × 110 μm^3). Accanto *et al.* [52] proposed an optical system to perform multiplexed temporally focused-light shaping (MTF-light shaping) where the light shaping was realized through two-dimension computer generated holography (2D-CGH) or GPC methods. This system permitted to project 15 μm diameter temporally focused spots over a volume of 300 x 300 x 500 μm sampled with 50 distinct planes.

CGHs suffer also from speckles, namely variations of the light distribution within the reconstructed hologram. Those inhomogeneities originate from the computation of the hologram which relies on iterative algorithms to modulate only the phase while the output intensity is optimized by having a random phase parameter at the focal point [14]. Speckle fluctuations are on the order of 20% when one-photon stimulation is adopted, while they reach 50% in case of two-photon stimulation [14]. To counteract this issue, generalized phase contrast method can be used to generate speckle-free CGHs. This method combined with TF was successfully ap-

plied to stimulate ChR2 expressed in cultured cells, cultured neurons and in mouse acute cortical slices where as a consequence large photocurrents were measured [53].

1.3. Motivation and outline of this thesis

1.3.1. Motivation

To date, the majority of the joint progress in opsin engineering and optical methods worked to facilitate the activation of neuronal ensembles, which is often called "*circuit optogenetics*" [54]. Here, neural circuits at different brain location are optically manipulated with single-cell spatial precision and millisecond temporal resolution. However, a further transition is required to investigate sub-synapse domains at the synapse level. [55]. For example, it would currently be difficult to perform an experiment focusing stimulation light at single axonal boutons or dendrites in order to mimic local neurotransmission that is not necessarily coupled to an action potential. As reported in [56] most of the optogenetic tools are localized throughout the cell without specificity for sub-cellular compartments. Consequently, the optogenetic stimulation often does not provide specific information about the effect of the stimulation on the sub-cellular physiology and signaling. In this picture sub-cellular optical targeting and readout are needed to provide more specific information.

Sub-cellular optogenetics is an emerging field and several experiments have already tried methods to reduce the active area of photostimulation. For instance, Stahlberg and colleagues [55] developed a mutants of channelrhodopsins, known as step-function channelrhodopsins, that can be activated and deactivated with light at different wavelengths. It was demonstrated that these actuators expressed in hippocampal neurons can be efficiently activated by illuminating a central region with a specific wavelength and simultaneously inactivated by co-illumination with another wavelength. This co-illumination was imposed on the sample in a donut shape overlapping the central region of activation, much like the excitation used in stimulated emission depletion (STED) microscopy. This STED-inspired approach allows to achieve micrometer activation areas, but the application of this strategy to sub-micrometer and even nanometer activation areas is still limited. The limitation arises from low photocurrents generated in the neuronal nanodomains that would be hardly detectable with the existing calcium or voltage reporters with spectral properties compatible with the optogenetic stimulation. Stahlberg and colleagues [55] propose two main solutions to this problem: either increasing the expression level of the step function opsins into the neurons of interest to be able to induce higher currents upon focal stimulation, or the improvement in the single channel conductance. These solutions tackle the bioengineering aspect of the problem. Differently, this thesis intends to improve the available optical tools to focus the stimulation light on sub-cellular ROIs. In this context, this work aims towards the realization of synaptically-localized optogenetic manipulations in living zebrafish brain to investigate synapse formation and growth in developing animals.

The design of the optical instrument to achieve this goal poses three main engineering problems.

One of the main technical requirements to perform such experiments is the confinement of the stimulation light within (sub)diffraction-limited areas located deep into the zebrafish brain and surrounded by inhomogeneous tissue. The dimension of the synaptic cleft is on the order of 20-30 nm [57] while the lateral size of the pre-synaptic compartment is typically below 1 μm and the post-synaptic receptors are organized in sub-synaptic domains with diameters typically below 100 nm [58]. In this scenario, the stimulation light traveling through refractive index inhomogeneous tissue will be impaired by optical aberrations. These distortions will cause a loss of confinement of the stimulation pattern and reduced peak intensities of the ultrashort pulses of NIR light leading ultimately to inefficient excitation.

Sub-cellular regions within the neuron under investigation should be activated within a short temporal window, especially if a STED-approach for activation and inactivation is adopted. Hence, CGH is the natural choice over point-scanning methods since it allows to probe simultaneously the activity of multiple ROIs. Moreover, in real-time manipulation the target structures change over time and the generation of the stimulation pattern should match these dynamics. For instance axonal growth in zebrafish larvae retinal ganglion cells occurs on the minutes time scale [59]. For such a reason the calculation of different stimulation patterns during the experiment needs to happen at the sub-minute time scale. However, traditional computational algorithms such as Gerchberg-Saxton and Weighted Gerchberg-Saxton are able to provide high quality holograms in terms of uniformity of intensity between the foci and efficiency (percentage of the laser light redirected into the foci) with relatively high computational time, ranging from seconds to several minutes. The computational cost depends on the number of pixels in the SLM, the number of iterations chosen for the calculation and number of spots within the pattern.

Finally another aspect to consider when performing all-optical interrogation of cellular and sub-cellular compartments in living animals is the potential harm of the stimulation light on the animal in terms of thermal damage. Even slight heating can cause an alteration of the sample physiology such as instability of synaptic responses [60] or modulation of the firing rate [61]. In the specific case of single synapse manipulation in living and developing zebrafish embryos to probe the synaptic growth over time requires long experiments and repeated irradiation of multiple ROIs with long exposures (milliseconds to seconds) [46]. Hence, thermal damage induced by prolonged NIR exposure needs to be investigated and quantified in order to draw the minimally invasive laser parameters.

1.3.2. Thesis outline

To pursue the scientific motivation of this thesis, three research problems were defined, analyzed and discussed. More specifically the improvement in the speed of the hologram calculation (Chapter 3) is an advantage to stimulate in real-time structures changing dynamically on the minute time scale. The compensation of the aberrations in the stimulation light (Chapter 4) allows for a more effective stimulation in terms of delivered power and facilitates the confinement of the stimulation within smaller area. Finally, stimulating lower repetition rate permits to achieve higher peak energies while reducing the thermal load on the sample (Chapter 5).

1

A detailed summary of the structure of this thesis follows.

Chapter 2: Instrument design: 3D optogenetics module combined with light sheet microscopy
All-optical studies of physiology requires the integration of an optical microscope with an optogenetic stimulation module within the same instrument. Here, I present an imaging system where a light sheet microscope is integrated with a stimulation module based on NIR light shaped with three-dimension computer generated holography (3D-CGH). This chapter provides a review on different light sheet designs and the integration of such microscope with the optogenetics module. I then focus on the specific instrument developed during this thesis work by giving technical notes on the optical design, implementation and operation of the system.

This chapter is based on the work: *Optogenetics and Light Sheet Microscopy.* L.Maddalena*, P. Pozzi*, N.G. Ceffa, B. van der Hoeven, E.C. Carroll. In: Papagiakoumou E. (eds) All-optical methods to study neuronal function, To appear in Neuromethods **Vol. 191**, Humana Press, New York, NY (2022)

Chapter 3: Fast Calculation of Computer Generated Holograms
Here a novel method to compute multi-spot 3D-CGH is described,and tested both computationally and and experimentally in comparison with other existing algorithms. The experimental test was performed on a custom stimulation module for for *in vivo* multiphoton optogenetics. The algorithm here presented is a variation of the Gerchberg-Saxton algorithm where the compressive sensing approach is applied to reduce the computational time. In fact, the algorithms: compressive sensing Gerchberg-Saxton and compressive sensing Weighted Gerchberg-Saxton here introduced allow to compute holograms with comparable spot brightness and uniformity as the Gerchberg-Saxton and Weighted Gerchberg-Saxton, while reducing by at least one order of magnitude the computational cost.

This chapter is based on the work: *Fast Calculation of computed generated holograms for 3D Photostimulation through Compressive-Sensing Gerchberg–Saxton Algorithm.* P. Pozzi*, L. Maddalena*, N.G. Ceffa, O. Soloviev, G. Vdovin, E.C. Carroll, M. Verhaegen. Methods and Protocols, **2**(1), 2-15, (2019).

Chapter 4: Local aberration control to improve efficiency in multiphoton holographic projections
This chapter describes the detrimental effect of optical aberrations on the light propagating through thick tissue where the index of refraction is spatially inhomogeneous. This problem affects the NIR light shaped with CGH used for the optogenetic stimulation. More specifically aberrations non-linearly impair the efficiency of the excitation. Hence, a sensorless adaptive optics approach is here proposed to counteract aberrations in holograms projected through turbid media. The main feature of this method is the capability to compensate local aberration within the FOV, a characteristic that makes it particularly suitable for applications in living tissue where the aberrations vary over a short distance. It is shown here that this

* These authors contributed equally to this work.

method improves the intensity of the stimulation pattern at least two-fold on both synthetic and biological samples.

This chapter is based on the work: *Local aberration control to improve efficiency in multiphoton holographic projections.* L. Maddalena, H. Keizers, P. Pozzi, E.C. Carroll. Optics Express, **30**(16), 29128-29147, (2022)

Chapter 5: Flexible control of pulse intensity and repetition rate for multiphoton photostimulation

Optogenetic stimulation typically uses pulsed near-infrared lasers to exploit their high peak powers needed for nonlinear excitation of actuators. However, a careful evaluation of the laser parameters such as repetition rate and average power is needed in order to estimate the thermal damage. Hence, this chapter shows the implementation of intra-cavity dumping within a mode-locked Ti:Sapphire laser used in the optical module described in the previous chapters of the thesis. This system enables to perform photostimulation experiments in both synthetic and living samples where pulse energy, average power and repetition rate can all be independently harnessed. Here, I characterize the performance of the system and demonstrate that a lower laser repetition rate can reduce the thermal load on living tissues.

This chapter is based on the work: *Flexible control of pulse intensity and repetition rate for multiphoton photostimulation.* L. Maddalena, M. Ouwehand, H. Safdar, E.C. Carroll. Frontiers in Physics, **10**(1005094), (2022)

Chapter 6: Conclusions and future outlook

This chapter provides a summary of the achievements accomplished in each of the previous chapters. Further improvements of those achievements are discussed together with a comparison to alternative approaches proposed by other research groups. Finally, I give an outlook on the directions for this research.

References

[1] M. Scanziani and M. Häusser, "Electrophysiology in the age of light," *Nature*, vol. 461, no. 7266, 2009.

[2] G. Miesenböck, "The Optogenetic Catechism," *Science*, vol. 326, pp. 395–399, 2009.

[3] M. Häusser, "Optogenetics: The age of light," *Nature Methods*, vol. 11, no. 10, 2014.

[4] G. Nagel, M. Brauner, J. F. Liewald, N. Adeishvili, E. Bamberg, and A. Gottschalk, "Light activation of Channelrhodopsin-2 in excitable cells of caenorhabditis elegans triggers rapid behavioral responses," *Current Biology*, vol. 15, no. 24, 2005.

[5] L. Fenno, O. Yizhar, and K. Deisseroth, "The development and application of optogenetics," *Annual Review of Neuroscience*, vol. 34, pp. 389–412, 2011.

[6] K. D. Piatkevich, M. H. Murdock, and F. V. Subach, "Advances in engineering and application of optogenetic indicators for neuroscience," *Applied Sciences*, vol. 9, no. 3, p. 562, 2019.

[7] C. Grienberger and A. Konnerth, "Imaging Calcium in Neurons," *Neuron*, vol. 73, no. 5, pp. 862–885, 2012.

[8] M. Inoue, "Genetically encoded calcium indicators to probe complex brain circuit dynamics in vivo," *Neuroscience Research*, vol. 169, pp. 2–8, 2021.

[9] A. Miyawaki, J. Llopis, R. Heim, J. Michael McCaffery, J. A. Adams, M. Ikura, and R. Y. Tsien, "Fluorescent indicators for Ca2+ based on green fluorescent proteins and calmodulin," *Nature*, vol. 388, no. 6645, pp. 882–887, 1997.

[10] M. Inoue, A. Takeuchi, S. Manita, S. i. Horigane, M. Sakamoto, R. Kawakami, K. Yamaguchi, K. Otomo, H. Yokoyama, R. Kim, T. Yokoyama, S. Takemoto-Kimura, M. Abe, M. Okamura, Y. Kondo, S. Quirin, C. Ramakrishnan, T. Imamura, K. Sakimura, T. Nemoto, M. Kano, H. Fujii, K. Deisseroth, K. Kitamura, and H. Bito, "Rational Engineering of XCaMPs, a Multicolor GECI Suite for In Vivo Imaging of Complex Brain Circuit Dynamics," *Cell*, vol. 177, no. 5, pp. 1346–1360, 2019.

[11] T.-W. Chen, T. J. Wardill, Y. Sun, S. R. Pulver, S. L. Renninger, A. Baohan, E. R. Schreiter, R. A. Kerr, M. B. Orger, V. Jayaraman, L. L. Looger, K. Svoboda, and D. S. Kim, "Ultra-sensitive fluorescent proteins for imaging neuronal activity," *Nature*, vol. 499, no. 7458, pp. 295–300, 2013.

[12] L. Tian, S. A. Hires, T. Mao, D. Huber, M. E. Chiappe, S. H. Chalasani, L. Petreanu, J. Akerboom, S. A. McKinney, E. R. Schreiter, C. I. Bargmann, V. Jayaraman, K. Svoboda, and L. L. Looger, "Imaging neural activity in worms, flies and mice with improved GCaMP calcium indicators," *Nature Methods*, vol. 6, no. 12, pp. 875–881, 2009.

[13] Y. Zhang, M. Rózsa, Y. Liang, D. Bushey, Z. Wei, J. Zheng, D. Reep, G. J. Broussard, A. Tsang, G. Tsegaye, S. Narayan, C. J. Obara, J.-X. Lim, R. Patel, R. Zhang, M. B. Ahrens, G. C. Turner, S. S.-H. Wang, W. L. Korff, E. R. Schreiter, K. Svoboda, J. P. Hasseman, I. Kolb, and L. L. Looger, "Fast and sensitive GCaMP calcium indicators for imaging neural populations," *bioRxiv*, 2021.

[14] V. Emiliani, A.E. Cohen, K. Deisseroth, and M. Häusser., "Symposium All-Optical Interrogation of Neural Circuits," *The Journal of Neuroscience*, vol. 35, pp. 13917–13926, 2015.

[15] S. Bovetti, C. Moretti, and T. Fellin, "Patterned Two-Photon Illumination for High-Speed Functional Imaging of Brain Networks In Vivo," in *Advanced Optical Methods for Brain Imaging. Progress in Optical Science and Photonics*, vol. 5, pp. 123–141, Springer, 2019.

[16] Y. Bando, C. Grimm, V. H. Cornejo, and R. Yuste, "Genetic voltage indicators," *BMC Biology*, vol. 17, no. 71, p. 71, 2019.

[17] D. Brinks, A. J. Klein, and A. E. Cohen, "Two-Photon Lifetime Imaging of Voltage Indicating Proteins as a Probe of Absolute Membrane Voltage," *Biophysical Journal*, vol. 109, no. 5, pp. 914–921, 2015.

[18] M. P. Chien, D. Brinks, G. Testa-Silva, H. Tian, F. P. Brooks, Y. Adam, W. Bloxham, B. Gmeiner, S. Kheifets, and A. E. Cohen, "Photoactivated voltage imaging in tissue with an archaerhodopsin-derived reporter," *Science Advances*, vol. 7, no. 19, 2021.

[19] A. Scimemi and M. Beato, "Determining the neurotransmitter concentration profile at active synapses," *Molecular Neurobiology*, vol. 40, no. 3, pp. 289–306, 2009.

[20] B. L. Sabatini and L. Tian, "Imaging Neurotransmitter and Neuromodulator Dynamics In Vivo with Genetically Encoded Indicators," *Neuron*, vol. 108, no. 1, pp. 17–32, 2020.

[21] G. Nagel, T. Szellas, W. Huhn, S. Kateriya, N. Adeishvili, P. Berthold, D. Ollig, P. Hegemann, and E. Bamberg, "Channelrhodopsin-2, a directly light-gated cation-selective membrane channel," *Proceedings of the National Academy of Sciences of the United States of America*, vol. 100, no. 24, pp. 13940–13945, 2003.

[22] G. C. Ellis-Davies, "Useful Caged Compounds for Cell Physiology," *Accounts of Chemical Research*, vol. 53, no. 8, 2020.

[23] G. C. R. Ellis-Davies, "Two-Photon Uncaging of Glutamate," *Frontiers in Synaptic Neuroscience*, vol. 10, no. 48, 2019.

[24] R. H. Kramer, A. Mourot, and H. Adesnik, "Optogenetic pharmacology for control of native neuronal signaling proteins," *Nature Neuroscience*, vol. 16, no. 7, pp. 816–823, 2013.

[25] T. Knöpfel, "Genetically encoded optical indicators for the analysis of neuronal circuits," *Nature Reviews Neuroscience*, vol. 13, no. 10, pp. 687–700, 2012.

[26] V. Nikolenko, B. O. Watson, R. Araya, A. Woodruff, D. S. Peterka, and R. Yuste, "SLM microscopy: Scanless two-photon imaging and photostimulation with spatial light modulators," *Frontiers in Neural Circuits*, vol. 2, no. 5, 2008.

[27] V. Szabo, C. Ventalon, V. De Sars, J. Bradley, and V. Emiliani, "Spatially selective holographic photoactivation and functional fluorescence imaging in freely behaving mice with a fiberscope," *Neuron*, vol. 84, no. 6, pp. 1157–1169, 2014.

[28] J. P. Rickgauer, K. Deisseroth, and D. W. Tank, "Simultaneous cellular-resolution optical perturbation and imaging of place cell firing fields," *Nature Neuroscience*, vol. 17, no. 12, pp. 1816–1824, 2014.

[29] A. M. Packer, L. E. Russell, H. W. Dalgleish, and M. Häusser, "Simultaneous all-optical manipulation and recording of neural circuit activity with cellular resolution in vivo," *Nature Methods*, vol. 12, no. 2, pp. 140–146, 2015.

[30] E. C. Carroll, S. Berlin, J. Levitz, M. A. Kienzler, Z. Yuan, D. Madsen, D. S. Larsen, E. Y. Isacoff, and W. Denk, "Two-photon brightness of azobenzene photoswitches designed for glutamate receptor optogenetics," *Proceedings of the National Academy of Sciences of the United States of America*, vol. 112, no. 7, pp. E776–E785, 2015.

[31] S. Bovetti, C. Moretti, S. Zucca, M. Dal Maschio, P. Bonifazi, and T. Fellin, "Simultaneous high-speed imaging and optogenetic inhibition in the intact mouse brain," *Scientific Reports*, vol. 7, p. 40041, 2017.

[32] A. R. Mardinly, I. A. Oldenburg, N. C. Pégard, S. Sridharan, E. H. Lyall, K. Chesnov, S. G. Brohawn, L. Waller, and H. Adesnik, "Precise multimodal optical control of neural ensemble activity," *Nature Neuroscience*, vol. 21, no. 6, pp. 881–893, 2018.

[33] M. dal Maschio, J. C. Donovan, T. O. Helmbrecht, and H. Baier, "Linking Neurons to Network Function and Behavior by Two-Photon Holographic Optogenetics and Volumetric Imaging," *Neuron*, vol. 94, no. 4, pp. 774–789, 2017.

[34] W. Yang and R. Yuste, "Holographic imaging and photostimulation of neural activity," *Current Opinion in Neurobiology*, vol. 50, pp. 211–221, 2018.

[35] C. McRaven, D. Tanese, L. Zhang, C.-T. Yang, M. Ahrens, V. Emiliani, and M. Koyama, "High-throughput cellular-resolution synaptic connectivity mapping in vivo with concurrent two-photon optogenetics and volumetric Ca 2+ imaging," *bioRxiv*, 2020.

[36] K. Deisseroth, "Circuit dynamics of adaptive and maladaptive behaviour," *Nature*, vol. 505, no. 7483, pp. 309–317, 2014.

[37] L. Petreanu, D. Huber, A. Sobczyk, and K. Svoboda, "Channelrhodopsin-2-assisted circuit mapping of long-range callosal projections," *Nature Neuroscience*, vol. 10, no. 5, pp. 663–668, 2007.

[38] B. R. Arenkiel, J. Peca, I. G. Davison, C. Feliciano, K. Deisseroth, G. J. Augustine, M. D. Ehlers, and G. Feng, "In Vivo Light-Induced Activation of Neural Circuitry in Transgenic Mice Expressing Channelrhodopsin-2," *Neuron*, vol. 54, no. 2, pp. 205–218, 2007.

[39] D. Oron, E. Papagiakoumou, F. Anselmi, and V. Emiliani, "Two-photon optogenetics," *Progress in Brain Research*, vol. 196, pp. 119–143, 2012.

[40] J. P. Rickgauer and D. W. Tank, "Two-photon excitation of channelrhodopsin-2 at saturation," *Proceedings of the National Academy of Sciences of the United States of America*, vol. 106, no. 35, pp. 15025–5030, 2009.

[41] L. E. Russell, H. W. Dalgleish, R. Nutbrown, O. M. Gauld, D. Herrmann, M. Fişek, A. M. Packer, and M. Häusser, "All-optical interrogation of neural circuits in behaving mice," *Nature Protocols*, vol. 17, pp. 11579—1620, 2022.

[42] A. Bègue, E. Papagiakoumou, B. Leshem, R. Conti, L. Enke, D. Oron, and V. Emiliani, "Two-photon excitation in scattering media by spatiotemporally shaped beams and their application in optogenetic stimulation.," *Biomedical optics express*, vol. 4, no. 12, pp. 2869–79, 2013.

[43] N. C. Pégard, A. R. Mardinly, I. A. Oldenburg, S. Sridharan, L. Waller, and H. Adesnik, "Three-dimensional scanless holographic optogenetics with temporal focusing (3D-SHOT)," *Nature Communications*, vol. 8, no. 1228, 2017.

[44] K.König, "Multiphoton microscopy in life sciences," *Journal of Microscopy*, vol. 200, no. 2, pp. 83–104, 2000.

[45] K. Podgorski and G. Ranganathan, "Brain heating induced by near-infrared lasers during multiphoton microscopy," *Journal of Neurophysiology*, vol. 116, no. 3, pp. 1012–1023, 2016.

[46] A. Picot, S. Dominguez, C. Liu, I. W. Chen, D. Tanese, E. Ronzitti, P. Berto, E. Papagiakoumou, D. Oron, G. Tessier, B. C. Forget, and V. Emiliani, "Temperature Rise under Two-Photon Optogenetic Brain Stimulation," *Cell Reports*, vol. 24, pp. 1243–1253, 7 2018.

[47] M. Rauzi and P. F. Lenne, *Cortical Forces in Cell Shape Changes and Tissue Morphogenesis*, vol. 95. 2011.

[48] E. Ronzitti, V. Emiliani, and E. Papagiakoumou, "Methods for three-dimensional all-optical manipulation of neural circuits," 2018.

[49] E. Papagiakoumou, V. de Sars, D. Oron, and V. Emiliani, "Patterned two-photon illumination by spatiotemporal shaping of ultrashort pulses," *Optics Express*, vol. 16, no. 26, p. 22039, 2008.

[50] O. Hernandez, E. Papagiakoumou, D. Tanese, K. Fidelin, C. Wyart, and V. Emiliani, "Three-dimensional spatiotemporal focusing of holographic patterns," *Nature Communications*, vol. 7, 6 2016.

[51] A. R. Mardinly, I. A. Oldenburg, N. C. Pégard, S. Sridharan, E. H. Lyall, K. Chesnov, S. G. Brohawn, L. Waller, and H. Adesnik, "Precise multimodal optical control of neural ensemble activity," *Nature Neuroscience*, vol. 21, no. 6, pp. 881–893, 2018.

[52] N. Accanto, C. Molinier, D. Tanese, E. Ronzitti, Z. L. Newman, C. Wyart, E. Isacoff, E. Papagiakoumou, and V. Emiliani, "Multiplexed temporally focused light shaping for high-resolution multi-cell targeting," *Optica*, vol. 5, no. 11, 2018.

[53] E. Papagiakoumou, F. Anselmi, A. Bègue, V. De Sars, J. Glückstad, E. Y. Isacoff, and V. Emiliani, "Scanless two-photon excitation of channelrhodopsin-2," *Nature Methods*, vol. 7, no. 10, 2010.

[54] I. W. Chen, E. Papagiakoumou, and V. Emiliani, "Towards circuit optogenetics," *Current Opinion in Neurobiology*, vol. 50, pp. 179–189, 2018.

[55] M. A. Stahlberg, C. Ramakrishnan, K. I. Willig, E. S. Boyden, K. Deisseroth, and C. Dean, "Investigating the feasibility of channelrhodopsin variants for nanoscale optogenetics," *Neurophotonics*, vol. 6, no. 1, p. 1, 2019.

[56] B. R. Rost, F. Schneider-Warme, D. Schmitz, and P. Hegemann, "Optogenetic Tools for Subcellular Applications in Neuroscience," *Neuron*, vol. 96, no. 3, pp. 572–603, 2017.

[57] E. D. De Robertis and H. S. Bennett, "Some features of the submicroscopic morphology of synapses in frog and earthworm.," *The Journal of biophysical and biochemical cytology*, vol. 1, no. 1, pp. 47–58, 1955.

[58] X. Yang and W. Annaert, "The nanoscopic organization of synapse structures: A common basis for cell communication," *Membranes*, vol. 11, p. 248, 4 2021.

[59] M. P. Meyer and S. J. Smith, "Evidence from in vivo imaging that synaptogenesis guides the growth and branching of axonal arbors by two distinct mechanisms," *Journal of Neuroscience*, vol. 26, no. 13, 2006.

[60] P. Andersen and E. I. Moser, "Brain temperature and hippocampal function," *Hippocampus*, vol. 5, no. 6, pp. 491–498, 1995.

[61] J. M. Stujenske, T. Spellman, and J. A. Gordon, "Modeling the Spatiotemporal Dynamics of Light and Heat Propagation for InVivo Optogenetics," *Cell Reports*, vol. 12, no. 3, pp. 525–534, 2015.

2

Instrument design: 3D optogenetic module combined with light sheet microscopy

Light sheet microscopy is a powerful method for imaging small translucent samples in vivo, owing to its unique combination of fast imaging speeds, large field of view and low phototoxicity. This chapter briefly reviews state-of-the-art technology for variations of light sheet microscopy. We review recent examples of optogenetics in combination with light sheet microscopy and discuss some current bottlenecks and horizons of light sheet in all-optical physiology. We describe how three-dimensional optogenetics can be added to an home-built light sheet microscope, including technical notes about choices in microscope configuration to consider depending on the time and length scales of interest.

This chapter is based on the work: *Optogenetics and Light Sheet Microscopy.* In: Papagiakoumou E. (eds) All-optical methods to study neuronal function, To appear in Neuromethods **Vol. 191**, Humana Press, New York, NY

2.1. Imaging translucent organisms

Larval fish, flies, and worms are popular model organisms in developmental biology [1] and, increasingly, in systems neuroscience [2–4]. Optical translucency make these organisms well-suited to visualize physiological functions using high-resolution fluorescence imaging with sub-cellular spatial resolution. Small size and their ability to thrive when immersed in water make it possible even to image embryonic development and behaviors *in toto* over hours or days [5].

Light sheet microscopy, also known as Selective Plane Illumination Microscopy (SPIM), has emerged as the method of choice for imaging smaller organisms, offering a number of advantages over point-scanning microscopy in speed, accessible volume, and phototoxicity. The light sheet revival over the last two decades is tightly associated with important milestones in live tissue imaging, including the iconic example of whole-brain imaging in larval zebrafish (*Danio rerio*). Launched by early examples of calcium imaging of fictive activity [6], several research groups worldwide now routinely record calcium activity from the nearly 10^5 neurons of the young awake, behaving zebrafish. The resulting avalanche of data is beginning to lead to new insights about the communication between different brain areas (see [3, 7] for recent reviews).

A natural extension to such imaging studies is the integration of optical methods for perturbation, such as optogenetics [8, 9], optopharmacology [10], and cell ablation [11, 12]. The expanding toolkit of molecular probes offers many optogenetic actuators to remotely activate or inactivate cellular processes. In the context of controlling neural activity, this progress in engineering molecular probes, together with the development of suitable optical methods [13], makes possible to photostimulate action potentials in cells expressing photosensitive channels and read out the affected neural activity using fluorescent reporters for calcium [14] or voltage [15]. Many of these tools have been developed into transgenic animals strains [16, 17]. Early demonstrations of optogenetic manipulations in combination with light sheet microscopy include optogenetic control over a variety of physiological phenomena, especially in larval zebrafish, from the beating of the heart [18] to cellular control of reflexive behaviors [19].

In this chapter, we describe how optogenetics can be added to a home-built microscope inspired by the open source project OpenSpim [20]. As an example, we describe in detail a microscope configuration suitable for cellular or sub-cellular optogenetics in larval zebrafish. The method involves adding two-photon photostimulation shaped by computer generated holography (2P-CGH). The stimulation module exploits the high numerical aperture (NA) detection objective of the light sheet to simultaneously excite multifocal points targeted either to sub-cellular regions or to multiple somata. The light sheet module provides flexibility to readout neural activity in tiny organisms from small volumes to whole brain. Volumetric imaging is achieved with an electrically tunable lens (ETL), allowing independent control of imaging depth without moving the detection objective and consequently the axial location of the stimulation foci.

We provide technical notes on optical alignment, alternative configurations for different applications, and limitations and challenges of combining optogenetics

with light sheet microscopy. Finally, we offer some perspectives on extending all-optical physiology to higher spatial resolution *in vivo*.

2.1.1. Light sheet technologies

The functioning principle of light sheet microscopy is to illuminate the sample with a thin sheet of light while collecting the fluorescent signal at an angle (usually orthogonal) relative to the illuminated plane. The illuminated plane is aligned with the focal plane of the detection objective enabling an image to be collected by a camera, as in a widefield microscope. Whereas laser scanning confocal microscopy achieves optical sectioning through rejection of photons generated outside of the excitation focus, light sheet microscopy avoids generating out of focus fluorescence. This approach provides optical sectioning while minimizing photobleaching and phototoxicity.

Light sheet configurations

Light sheet microscopes can be implemented in a variety of configurations, distinguished by the the position and number of microscope objectives, the sheet-forming illumination optics, and the detection optics. Readers are referred to several excellent review articles focused on developmental biology and high-resolution applications [21, 22]. With respect to brain imaging, variations of light sheet microscopy have been driven by two main challenges:

1. balancing optical sectioning with a large field of view (FOV)
2. maximizing imaging speed to resolve fast dynamics from fluorescent sensors.

Here, we briefly compare light sheet configurations used for whole-brain imaging in zebrafish, as shown in Fig. 2.1.

Selective Plane Illumination

The basic SPIM design (Fig. 2.1(a)) uses two orthogonal microscope objectives for illumination (I) and detection (D) of fluorescence. The illumination light is typically shaped into a two-dimensional sheet with a cylindrical lens [23, 24]. To image a volume, the sample is either translated with respect to the detection objective, or the light sheet is scanned with a galvanometric mirror while also keeping the illuminated plane conjugated to the camera with either a piezo objective or an electrically tunable lens.

Later it was demonstrated that rapid scanning of a pencil beam (a long, thin illumination profile in one dimension) could generate a ”virtual” sheet, as seen by the camera, with the major advantage of reducing light exposure to the sample [25]. This approach is alternately called digitally scanned light sheet microscopy (DSLM). In this case, volume acquisition requires a second scanning mirror.

For (relatively) small, translucent samples, where light can enter the sample from any side, the SPIM design is convenient. Because two (or more) objective

lenses are used this design decouples the axial(Δz) and lateral ($\Delta x, \Delta y$) resolution which scale as the inverse of the numerical aperture for excitation objective, $\Delta z \sim NA_I^{-1}$ and the detection objective, $\Delta x, \Delta y \sim NA_D^{-1}$.

The constraints on axial resolution limit the usable FOV. The usable length of a Gaussian light sheet is proportional to its thickness. For this reason, longer Gaussian profiles have poor optical sectioning and increased phototoxicity by illuminating a sample slice thicker than the detection depth of field. The most immediate improvement for obtaining longer 1-D uniform excitation profiles comes as a trade-off with temporal resolution: tiling the excitation light sheet [26] allows, in principle, to select only the central uniform region of the excitation profile, stitching together multiple images over an arbitrary FOV. However, in all-optical physiology experiments, the decreased temporal resolution may be unacceptable.

An alternative way to obtain uniform illumination over a larger FOV is to illuminate the sample from two sides using an additional illumination objective opposite of the first (Dual-sided Light Sheet). Depending how the sample is mounted in the microscope, it may also be possible to illuminate from additional angles [27].

Multiview Illumination

In the case of multiple illumination sheets, each sheet needs only cover half of the total FOV, so a lower NA sheet can be used to better preserve optical sectioning. For instance, the IsoView [28] light sheet microscope employs two different DSLM geometries to simultaneously illuminate the sample from two opposite sides, collecting the view with two cameras (Fig. 2.1b). In this method, combining the overlapping images from multiple angles, it is possible to achieve isotropic spatial resolution [28]. This parallel excitation also represents a robust solution against sample opacity. Moreover, employing two sets of galvanometric mirrors in each illumination arm (one for scanning, one for correcting incidence angle on the sample) allows to employ on-line optimization algorithms [29] to partially correct for low-order sample-induced aberrations. These improvements come at a cost both in terms of hardware (number of parts and alignment difficulty) and software complexity. Additionally, because every image is collected twice, the amount of data collected necessitates high-end storage capabilities and lengthy analysis pipelines in order to properly fuse the views into a final volume. An added benefit provided by this geometry is the sample can be left stationary, while the scanning is performed by the galvanometric mirrors (to move the excitation profile in 3D) coupled with piezo motors, that keep the detection objective focused on the illumination plane.

Swept Plane (Single Objective)

A single-objective light sheet configuration, employing epi-fluorescence, can be obtained in several ways [30, 31] by generating a tilted elongated focus (Fig. 2.1(c)). The tilted sheet is swept laterally across the sample to image a volume. Swept plane approaches are gaining ground in neuroimaging because they facilitate high volume speeds, as reviewed recently by Hillman [32]. The single-objective geometry has

the advantage of using the same sample preparation as confocal or two-photon (2P) microscopy, and uniquely, can also be extended to samples of arbitrary size [33]. While the swept plane approach partially sacrifices resolution because every image is formed collecting planes from regions far from the optimal focus, re-imaging the tilted plane (and some post-processing) can recover diffraction-limited resolution. Higher NA objectives with short working distances can also be used when applying light-sheet microscopy to small samples (e.g. single cells) [34, 35].

Hybrid Light Sheet Microscopes

A clever approach to improve imaging speed is to increase out of focus contributions in a principled way. Manipulating the detection point-spread function, for instance by adding spherical aberration [36] or a cubic phase profile [37], extends the effective depth of field of the detection objective so that information can be harvested from a thicker illuminated volume. Other approaches for simultaneous volume acquisition borrow from light field microscopy. For instance, an exciting direction of hybrid imaging called Selecive Volume Illumination (SVIM) [38] merges light-sheet excitation with light field microscopy techniques to allow extremely fast (tens of Hz) volumetric imaging. The trade-off for resolution is acceptable for somatic imaging [39] and SVIM significantly improves contrast over light field microscopy with wide-field illumination.

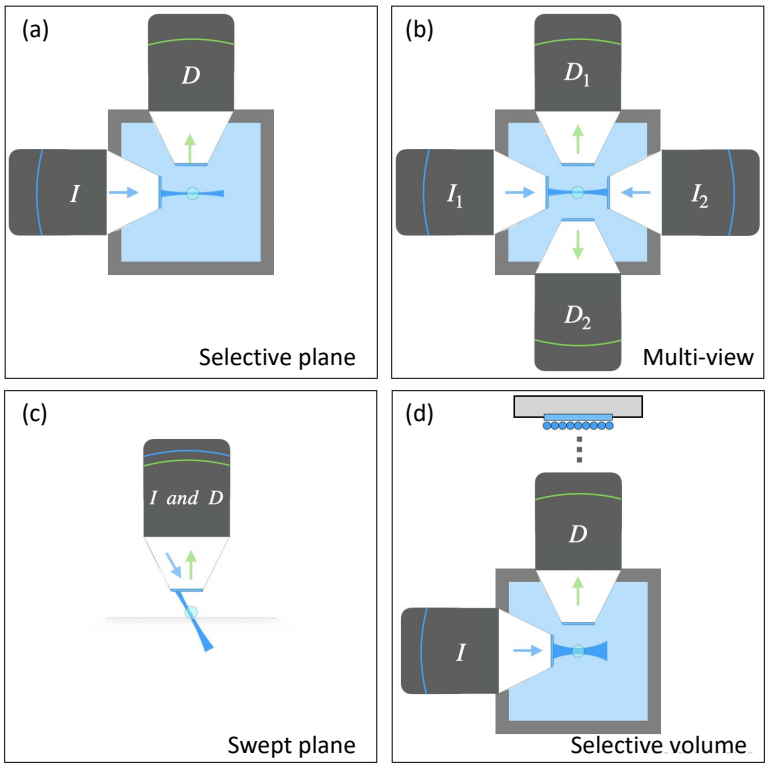

Figure 2.1: **Selection of light sheet microscope configurations used for whole-brain imaging in larval zebrafish.** (a) Fluorescence is collected along a sheet of light formed by side-ways illumination. (b) In variations of multi-view light sheet microscopy additional objectives illuminate or collect fluorescence simultaneously allowing for either greater uniformity of illumination or multiplexing image formation from different angles. (c) In variations of single-objective light sheet , a tilted sheet is swept laterally across the sample while collecting a tilted epifluorescent image. (d) Selective volume illumination microscopy is a hybrid of light sheet illumination and extended-depth of field detection.

Engineering illumination improves resolution and photodamage

Light sheet microscopy is intrinsically efficient with photons. The local intensity required for light sheet imaging is smaller than for confocal techniques [40], including spinning disk confocal microscopy. In fact, with scanning light sheet, the total energy deposited at each point of a three-dimensional (3D) sample is reduced by a factor equal to the total number of sections obtained during the imaging [41]. This minimizes photodamage to the specimen and also has a positive effect on the imaging speed. Moreover, detectors used in light sheet, as CCDs or sCMOS cameras provide a better dynamical range rather than single-pixel detectors used in point-scanning approaches (e.g., avalanche photodiodes or photomultiplier tubes).

A poor dynamic range causes problems of detector saturation which translates to trade-offs in smaller volume or slower acquisition time. Light sheet illumination is less prone to excitation saturation compared to point-scanning techniques, so it is not necessary to compromise imaging speed with long frame exposure times.

To further improve on minimizing illumination intensity and photodamage, engineering the excitation beam to produce quasi non-diffracting beams; in particular Bessel beams [42, 43], has strongly impacted the field. Bessel-like beams preserve a small beam waist over a longer distance compared to beams with a Gaussian amplitude profile (Table 4.1), translating to more uniform illumination over the FOV of the detection objective.

Moreover, when propagating through inhomogeneous samples, Bessel-like beams have reduced scattering and beam spreading due to their self-healing property, namely the beam recovers the initial intensity profile after an obstacle. However, Bessel beams have a major downside: a large portion of energy resides in side-lobes, that can spread out for a tens of microns beyond the central peak. In fact, they may generate fluorescence signal from out-of-focus planes, preventing the theoretical gain in optical sectioning while increasing phototoxicity. For this reason, researchers have introduced methods to reduce the contribution of the side lobes to the image:

1. Prevention: Multiphoton excitation can prevent excitation of fluorescence in the side lobes because of their lower instantaneous intensity [44] (as also discussed in Chapter 10 by Ji) .

2. Displacement: Interference between multiple illumination rays can diminish illumination intensity in the side lobes. For example, lattice light-sheet microscopy [45] employs a spatial light modulator as active optical element to superimpose an array of Bessel beams that destructively interfere and consequently reduce the impact of undesired side lobes. This solution has been proven effective not only in increasing resolution when imaging cellular samples, but also when studying larger animals (e.g. zebrafish embryos), if combined with adaptive optics techniques to compensate for the aberrations introduced by the morphology of larger organisms [46].

3. Rejection: Electronically, fluorescence generated by side lobes can be mitigated by only collecting signal confocal to the scanned beam [47]. This approach only slightly increases system complexity since modern CCD and CMOS cameras already allow to calibrate an internal rolling shutter modality, where only a few lines of pixels are active at a time, following the central lobe of the Bessel excitation.

2.1.2. Design choices

Prioritize scale, resolution, or speed

Optimal choice of the light sheet microscope configuration depends on the research questions of interest, particularly with respect to the spatial and temporal resolution

required. Small organisms tend to have smaller cells than mammalian tissues, so resolution is of particular concern in both imaging and photostimulation. The choice of light sheet approach is often a matter of choosing the best trade-off between speed and resolution, given the dimensions and transparency of the sample.

In designing the system described below, we considered applications involving the larval zebrafish. For this sample, the SPIM design is convenient. The larval zebrafish brain occupies a volume of approximately 500 x 800 x 300 μm, and individual neurons are typically 5-10 μm in diameter. The whole brain is typically measured in a single FOV of a 10x detection objective, with which cellular resolution is easily achieved. However, we also wanted the flexibility to image sub-cellular resolution in smaller brain regions, so we have used higher magnification to achieve sampling of better than 0.2 μm per pixel on the camera. This lateral resolution is achieved with a high-NA water-dipping detection objective (practically limited to NA<1.1 by commercial objectives). To achieve sub-cellular axial resolution over most of the brain, we chose to apply the superior optical sectioning of a Bessel beam.

For example, considering illumination with a laser source with λ = 488 nm, and an excitation objective with NA $= 0.29$, a Bessel profile can be generated to cover uniformly 160 μm with a central peak width of $\simeq$ 0.6 μm. To reach the same FOV, a Gaussian beam would have more than double thickness (around 10 μm, as calculated following precisely the Rayleigh length formula): of course, this value is chosen following a trade-off between length and the acceptable divergence that can be tolerated at the edges of the FOV.

Type of photostimulation

The experimenter has many options to add photostimulation optics to a light sheet microscope, including the variety of methods discussed in Chapters (see chapters 1, 3, 5, 7). Both scanning and parallel approaches to photostimulation can be applied to small, translucent samples. In the first case resonant scanners or galvanometric mirrors steer a focused beam across multiple region of interest (ROI)s whereas in the latter case all the ROIs are illuminated simultaneously by using computer generated holograms (CGHs) projected through spatial light modulators (SLMs). The same excitation strategies applied in living animals requires increased optical sectioning and penetration depth, both provided by 2P illumination. For example, Dal Maschio et al. [48] integrate a 2P CGH module with a 2P scanning microscope, generating an instrument capable of identifying behavior-related neural circuits in living zebrafish larvae. The stimulation is targeted to single soma with a diameter of ∼6 μm and axial resolution of ∼9 μm over a volume of ∼ 160×80×32 μm. Comparable lateral and axial resolution for circuit optogenetics are achieved by McRaven and colleagues [49], in their 2P-CGH setup coupled to a 2P scanning microscope with remote focusing, to discover cellular level motifs in awake zebrafish embryos. On the other hand De Medeiros, et al. [12] combine a scanning unit with a multiview light sheet microscope. This is a flexible instrument to perform ablation of single cells in zebrafish embryos and also localized optogenetic manipulations with concurrent *in toto* imaging in *Drosophila*. Here, the effect of the optogenetic manipulation can be monitored at the embryo scale with cellular resolution. Another example of SPIM

integrated with 2P scanning stimulation is presented in [27], where whole-brain imaging and brain-wide manipulations in larval zebrafish reveal causal interaction. All these works demonstrated that in the small brain of the larval fish ($\sim 0.1\ \mu m^3$), it is possible to both record and stimulate with millisecond temporal resolution and single cell precision over the full volume of the engaged neural circuit.

One photon or two?

As mentioned in other chapters, multiphoton excitation is the simultaneous absorption of *n* lower-energy photons to electronically excite a higher-energy single-photon transition. For visible-absorbing optogenetic chromophores, near infrared (NIR) wavelengths (700-1100 nm) are typical for 2P absorption. NIR has the added advantage of high penetration depth in biological tissues [50]. Transparent tissue might seem to obviate the need for multiphoton microscopy. On the contrary, there are several arguments for the use of 2P excitation light sheet microscopy.

On the imaging side, scanned beam approaches also made 2P excitation feasible because the spherical focus can generate the highest peak intensity for a given power, extending light sheet microscopy to imaging in highly scattering samples[51], [52]. Even for optically translucent samples like larval zebrafish, scattering is noticeably reduced. For brain imaging in larval zebrafish, 2P microscopy is often preferred because it is more orthogonal to the visual system [2]. Imaging with visible light impacts general brain activity, visual sensitivity, and even innate motor behaviors due to non-visual opsins [53], though by carefully avoiding direct illumination of the eyes, it is possible to deliver visual stimuli and even virtual reality [27].

For photostimulation with cellular, or sub-cellular, precision in 3D tissues, it is crucial to exploit multiphoton absorption for optical sectioning. Since 2P absorption is a non-linear process, its probability depends quadratically on the intensity of the excitation light. The main consequence is an improved optical sectioning because the stimulation is generated only in the vicinity of the geometrical focus where the light intensity is the highest [54]. The resolution of the multiphoton excited fluorescence is described as the full width half maximum (FWHM) of the three-dimensional 3D-point spread function (PSF) of the fluorescence intensity h^i of the excitation. The following equations describe the dependency of the 3D-PSF h^i on the 3D-PSF of the illumination intensity of two-photons excitation.

$$h^{2P}(u,v) \propto |I(u,v)|^2 \tag{2.1}$$

where u and v are respectively the axial and lateral coordinates of the optical system.

It should be noted that all-optical experiments require careful control to avoid heating effects induced by NIR stimulation [55]. Compared to experiments in rodents or organotypic tissues, small translucent organisms like zebrafish larvae are fragile and easily burned. Their small size, typically smaller than the beam waist exiting the microscope objective, means that a significant fraction of the animal's skin is exposed to defocused light, even while a tight, diffraction-limited focus may be achieved beneath the skin. When exposed to NIR light, even small amounts of

dark skin pigment can lead to unintentional burning. Furthermore, ectotherms like zebrafish and drosophila, lack the ability to maintain a constant internal body temperature, and typically regulate temperature behaviourally (e.g., by heat seeking or heat avoidance behaviour [3]). Even a 1-2 K rise in temperature may have a notable effect on the physiology under study. In 2P imaging, intensity is typically kept around 0.1 - $0.5 mW/\mu m^2$ [48]. In both 2-photon imaging and photostimulation, a potential control experiment to evaluate the 1-photon NIR effect is to test photostimulation with a lower peak power density, e.g., in mode-locked Ti:Sapphire lasers, switching into continuous wave mode provides a means to obtain the same average power with orders of magnitude lower energy density.

2.2. Materials

All-optical physiological experiments require an imaging system that combines a fluorescence microscope with a light path for photostimulation. The microscope serves dual purpose: first to acquire a baseline fluorescence image or movie to identify the spatial location of ROIs and second to acquire a continuous readout of the effect of photostimulation. Here we describe an example of a Bessel-beam light sheet microscope and a 2P-CGH module.

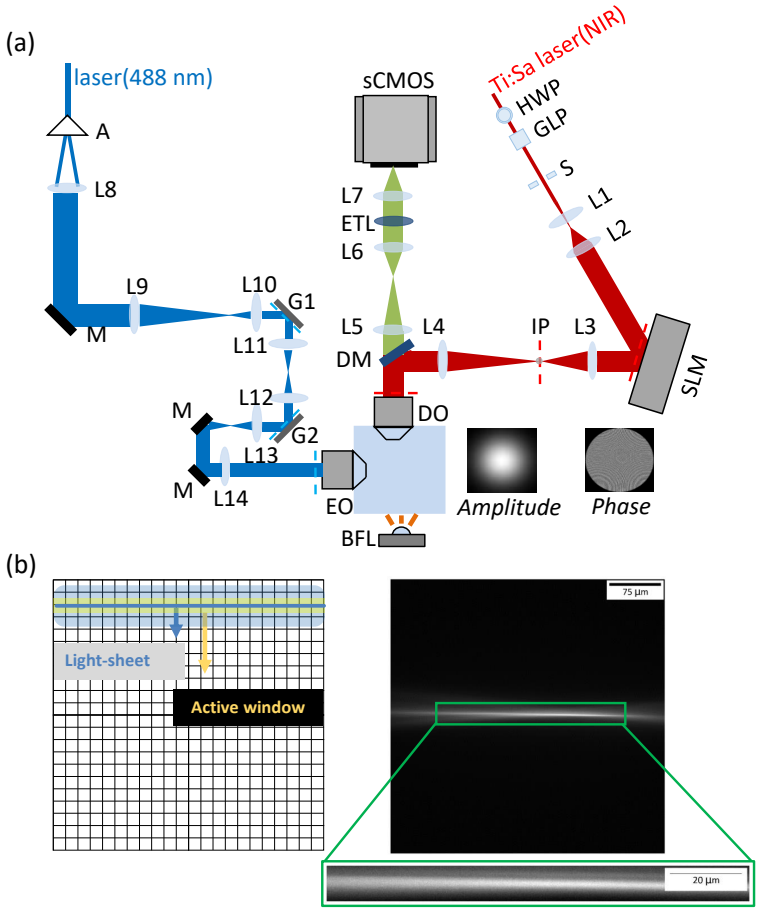

Figure 2.2: **Example configuration of light-sheet microscope with optogenetics** (a)The system consists of a light-sheet imaging module (left, blue lines) and an optogenetics module (right, red lines) that share a common light path through the high-NA detection objective (DO). In the imaging module, a continuous-wave visible wavelength laser is shaped in a Bessel beam by an axicon (A) and scanned onto the sample through galvo mirrors G1 and G2 and excitation objective (EO).Fluorescence collected through the detection objective (DO), is transmitted through a low-pass dichroic mirror (DM) and imaged onto a sCMOS camera by an electrically-tunable lens (ETL).The fluorescent signal is recorded with the concfocal slit detection approach schematically shown in panel b. In the 2P-CGH module, a Ti:Sa pulsed laser beam is magnified through a telescope (L1, L2), impinges on the SLM, placed in a plane where the wavefront is flat. Lenses (L3, L4) relay the wavefront from the SLM to the pupil of the DO. In the focal plane of lens L3 the inverse pinhole (IP) blocks the zero-order diffraction spot.(b) Left: Scheme of confocal slit detection. An active window (yellow line) on the sCMOS camera is rolled synchronously with the scanning of the Bessel beam illumination (cyan line). In this way we minimize the detection of fluorescence excited by the side lobes of the Bessel beam (light cyan halo). Right: Bessel beam projected into uniform fluorescent solution. The zoom in on the middle region of FOV shows the central lobe of the Bessel beam as it appears with confocal slit detection

2.2.1. Light sheet module

The microscope schematic shown in Fig. 3.1 is a digitally scanned light sheet implemented by scanning a Bessel beam in a 2D plane. The combination of an axicon with a plano-convex lens generates a beam shaped as a hollow cylinder. Since this beam is collimated, any subsequent conjugate plane can be chosen as the entry pupil of the microscope. The collimated ring is conjugated with two galvanometric mirrors (G1, G2, Thorlabs, ax1210-A) and the back aperture of the excitation objective (EO; Nikon, 10X/NA 0.3 CFI Plan Fluorite).

Fluorescence is collected through the detection objective (DO; Olympus, 20X/NA 1.0 XLUMPLFLN), transmitted through a low-pass dichroic mirror and finally the image is formed by a 300 mm tube lens (L5). The image is relayed to the sCMOS camera (Andor, Zyla 4.2) by a 1:1 telescope (L6 and L7, focal 150 mm). An electrically-tunable lens (ETL; Optotune, EL-16-40-TC-VIS-20D) lens, positioned in the common focus of the telescope, can scan the signal at different depths.Brigthfield images are collected by transmission of a white LED (BFL; Thorlabs, LEDW25E), mounted at the opposite side of the DO.

To effectively eliminate the out-of-focus emission excited by the side lobes of the Bessel beam, the design implements confocal slit detection of the fluorescent signal, as shown in inset Fig. 3.1(b). The slit is virtually created using an active window of the sCMOS camera that is rolled synchronously with scanning of the Bessel beam illumination. In this way we minimize the detection of fluorescence excited by the side lobes. The cost is a slower imaging speed.

The ETL in the detection path allows independent control of photostimulation in three dimensions and volumetric imaging, without moving either the objective lens or the sample. The accessible volume is determined by the choice of the tube lens L5. In fact, given the objective the focal of the tube lens is directly proportional to the image magnification. For such a reason longer focal lengths give access to a smaller volume, while they achieve better sampling of the fluorescence signal at the camera pixel. The ETL in the configuration shown in Fig. 3.1(a) allows to image a volume extending over 500μm. The photostimulation can be performed on a volume extending over 200 μm in depth, with the SLM being the limiting factor in the theoretical axial FOV.

2.2.2. 2P-CGH module

We implement computer generated holography for spatial patterning of the photostimulation light. As shown in Fig. 3.1(a) the ultra-short pulses of NIR light, emitted by the Ti:Sa laser (Coherent, Mira-900F), pass a combination of half-wave plate (HWP) and Glan-laser calcite polarizer (GLP, Thorlabs, GL5-B) to control the average power. A mechanical shutter (S; Uniblitz, LS2S2Z1) allows to block or transmit the light. Then the beam, magnified through a telescope (L1 and L2, focal 25.4 mm and 150 mm), impinges on the SLM (Meadowlark optics, P1920-600-1300-HDMI) placed in a plane where the wavefront is flat (where the Gaussian laser beam is collimated). Subsequent lenses relay the wavefront from the SLM to the pupil of the DO: here, the Fourier lens L3 (focal 250 mm) and lens L4 (focal 500 mm) magnify the beam to fill the back aperture of the objective. In the focal plane of

lens L3, an inverse pinhole (IP; custom tungsten deposition, diameter 1.3 mm, on glass window deposition thickness 0.5 mm) blocks the zero-order diffraction spot.

The light paths of the light sheet microscope and the 2P-CGH module join at a dichroic mirror (DM; Semrock, FF01-720/SP-25)), with a cutoff wavelength at 720 nm. This mirror reflects the NIR stimulation light to the sample and transmits the fluorescent readout to the sCMOS. Two-photon excited (TPE) epi-fluorescence can be recorded and this is useful to characterize the photostimulation beam as described in Appendix 2.A.1

The choice of focal lengths of lenses L3 and L4 is important in the design of the experiment. If the SLM image at the objective back aperture is smaller than the aperture itself the NA of the objective is not fully exploited. This might be an intentional choice. Otherwise if the SLM image is larger some stimulation light gets lost. The best option is to choose a telescope magnification which matches the dimension of the SLM image at the back aperture to the aperture itself. In this case the lateral resolution is only limited by the objective NA.

The pixelated structure of the SLM chip introduces in the reconstructed hologram a zero-order diffraction spot which appears as a bright spot in the center next to the hologram. To separate the hologram from the zero-order illumination we can either proceed algorithmically, or we can block the zero-order illumination physically. Since the result given by the second method can strongly degrade the quality of the image it is preferable to implement a combination of the two approaches to preserve the image quality. The hologram can be displaced from the zero-order algorithmically by introducing a constant defocus. Once CGH and zero-order lay at different depths the zero-order beam is blocked by means of an inverse pinhole without impairing the quality of the CGH.

In high-resolution applications, the spatial accuracy of photostimulation is paramount. As reported in [56] the precision to address a CGH to a specific target depends on the number of pixels in the SLM and grey scale values available. Several companies produce SLM with over 1000 pixel in the shorter axis, which provide the spatial accuracy required for sub-cellular manipulations and also a high number of degrees of freedom if the SLM is used as an adaptive element to correct for high-order aberrations. The accessible lateral and axial FOV for a CGH is inversely proportional to the SLM pixel size. However, fairly large pixel size (in the order of 10 μm) is preferred because, assuming a constant inter-pixel gap, the fill factor increases with the pixel size. A larger pixel size reduces also the cross-talk between pixels. Cross-talk acts as a low pass filter on the CGH and it is due to fringing field effect which cause gradual voltage changes across the border of neighbouring pixels and by elastic forces in the liquid crystal material [57]. In the setup in Fig. 3.1(a) we use a 1920 x 1152 pixels liquid crystal on silicon (LCoS)-SLM with a pixel pitch of 9.2 μm. This device guarantees 95.7% fill factor and a CGH switching rate of 31 Hz.

2.2.3. Sample Preparation

In SPIM, samples are usually mounted in tubes made of fluorinated ethylene propylene (FEP), a plastic with refractive index similar to water. The tube is filled with a solution of water and low melting temperature agarose ($\sim$ 1.5-2 %) for short

term imaging (1-3 hours). For larval zebrafish these conditions ensure stability of the sample while maintaining good physiological conditions given the time frame of the experiment. However, as reported in [58] for longer experiments (over 1 day) it is recommended to use lower agarose percentage (~ 0.1 %) or methylcellulose solutions (~ 3 %) to ensure stability but also proper growth of the sample especially between 24–72 hours post-fertilization.

2.3. Methods

2.3.1. Microscope alignment and calibration

The alignment of both light sheet microscope and 2P-CGH module is performed projecting respectively the Bessel beam and the zero-order diffraction beam into the microscope chamber filled with a solution of water and fluoresceine. The alignment needs to be checked daily and a step by step guide is reported in Appendix 2.A.1. To obtain good fidelity between the stimulation target and the holographic illumination, it is critical that the light sheet module and 2P-CGH module share a common coordinate system. This is accomplished by first calibrating the scan volume of the light sheet such that we can image the sample scanned by the Bessel beam within the volumetric FOV of the ETL (see Appendix 2.A.1). Then, a calibration between the volume accessible to the 3D-CGH and the FOV of the ETL is performed (see Appendix 2.A.1). Both volumetric scans are achieved by incrementing voltage on the ETL. Once the 2P-CGH and light sheet volumes are calibrated with the ETL, the two coordinate systems are then aligned through an affine transformation (see Appendix 2.A.1). This calibration is carried out before each experiment and the resulting affine transformation matrix is applied to the ROIs location selected on the image to get the input coordinates for the holographic stimulation.

2.3.2. Microscope resolution characterization

The resolution of the light sheet microscope is determined by measuring the point spread function (PSF) of the whole optical system known as the convolution between the PSF of the illumination and the PSF of the detection [59]. The PSF is the diffraction pattern of a point source viewed by an optical system [60], hence the PSF is measured on a three-dimensional image of a diffraction limited fluorescent point-source. The diffraction pattern, also known as Airy pattern, shows a central spot with surrounding diffraction rings. Bright rings are the maxima of the diffraction pattern and correspond to constructive interference of the light coming from the point sources. Conversely, dark areas are the minima of the diffraction pattern and originate from destructive interference. As stated by the Rayleigh criteria a microscope can distinguish as separate features any pair of points with a mutual distance equal to the separation between the central spot and the first diffraction minima of the Airy pattern [61]. In this picture the diameter of the central spot of the PSF, known as Airy disk, is a measure of the resolution capability of the optical system. The Airy disk diameter is measured in 3D looking at the xy, yz and xz slices of the PSF. Both lateral and axial resolution depends on the NA of the microscope and the light wavelength, however the axial resolution is roughly three times higher

than the lateral resolution [60], this is due to the intrinsic elongated shape of the PSF along the axial direction. In addition due to scattering at increased depths the axial PSF deteriorates due to spherical aberrations ad interference of out-of-focus light. Abbe's theory provides the following equations to define the theoretical lateral 2.2 and axial2.3 resolution .

$$R_{xy} = \frac{\lambda}{2NA} \tag{2.2}$$

$$R_z = \frac{2\lambda}{NA^2} \tag{2.3}$$

PSF extraction from microspheres imaging

The experimental PSF for both blue and green excitation channels is measured by imaging a solution of Tetraspeck microspheres (blue, green, orange and dark red fluorescence spectrum, 500 μm diameter) embended in 6 % agarose in Milli-Q and mounted into a FEP tube. Since the size of the beads scales as the fluorescent signal, here the beads diameter was chosen based on a reasonable brightness of the sample allowing automatic beads detection without signal saturation. A z-stack spanning over a volume of 70 μm with a z step spacing of 1μm, equal to the detection objective depth of field, is acquired with both blue and green excitation. A PSF extractor algorithm implemented in Python [62] and described in Appendix 2.A.3 allows to detect automatically the beads on the acquired raw data and to calculate the PSF for each bead. Finally the software yields the average PSF obtained from all the detected PSFs in the stacks. Figure 2.3 and Fig. 2.4 below show the resulting average PSF for respectively blue and green excitation channels. In the blue channel 38 beads were detected and averaged, whereas in green channel 35 beads were used for the calculation. Lateral (xy view) and axial (xz and yz views) PSF are measured along the dashed lines indicated in the images. The three plots show the result of a Gaussian fit performed along the dashed lines. The full-width-at-half-maximum (FWHM) from each Gaussian fit quantifies the size of the PSFs along the three dimensions. From the PSF sizes obtained we can conclude that the light sheet microscope has lateral resolution of 1 ±0.2 μm and 3.5 ±0.5 μm in z.

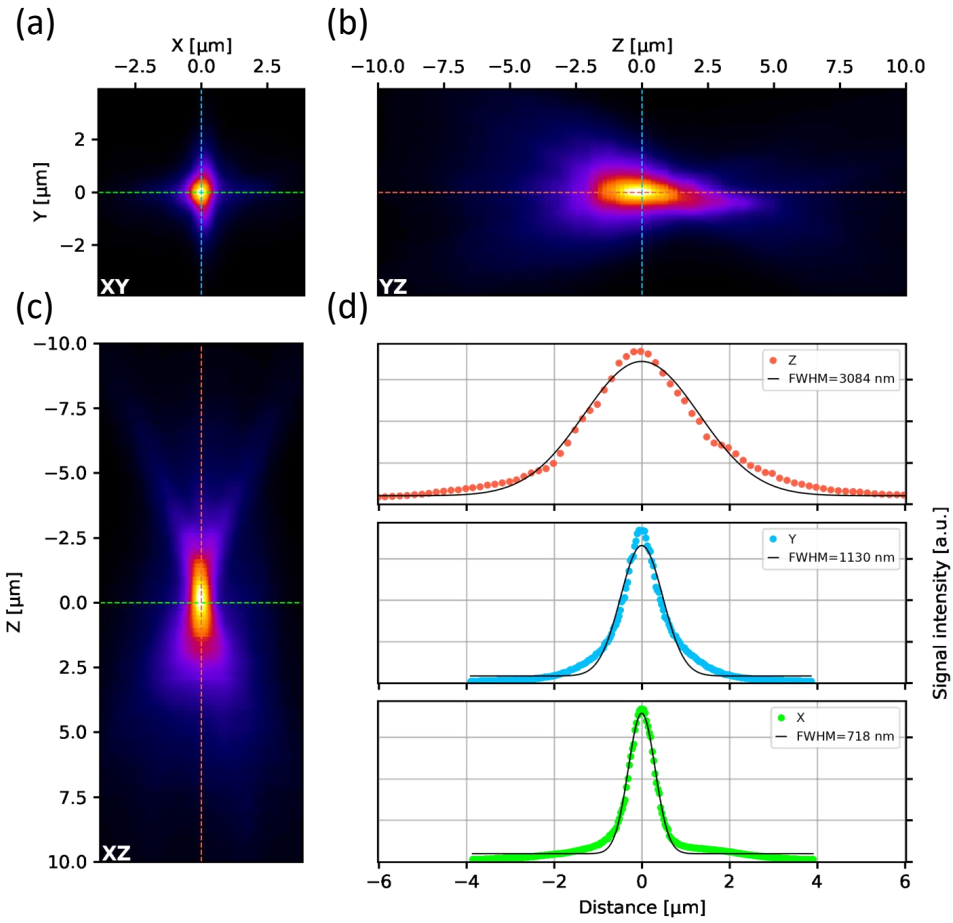

Figure 2.3: **Detection PSF measured from microspheres in blue excitation channel.** (a) xy cross-sections of the extracted average PSF. (b) yz cross-sections of the extracted average PSF. (c) xz cross-sections of the extracted average PSF. (d) Line profiles are measured along the dashed lines plotted onto the sections quantify the PSF size along the three dimensions.

PSF extraction from CGH projections

The same approach described in the previous subsection is used to quantify the PSF of the TPE fluorescence induced by holographic stimulation. A 7-point hologram with points sparsely distributed over a volume of 58 µm was projected into a FEP tube containing fluoresceine diluted in water. A z-stack encompassing a volume of 82 µm with a z-step of 1µm, equal to the detection objective depth of field, is acquired with the blue laser. The same algorithm for PSF extraction [62] used to characterize the light sheet microscope also served to detect CGH spots and compute an average PSF. The extracted average PSF is shown in Fig. 2.5 below,

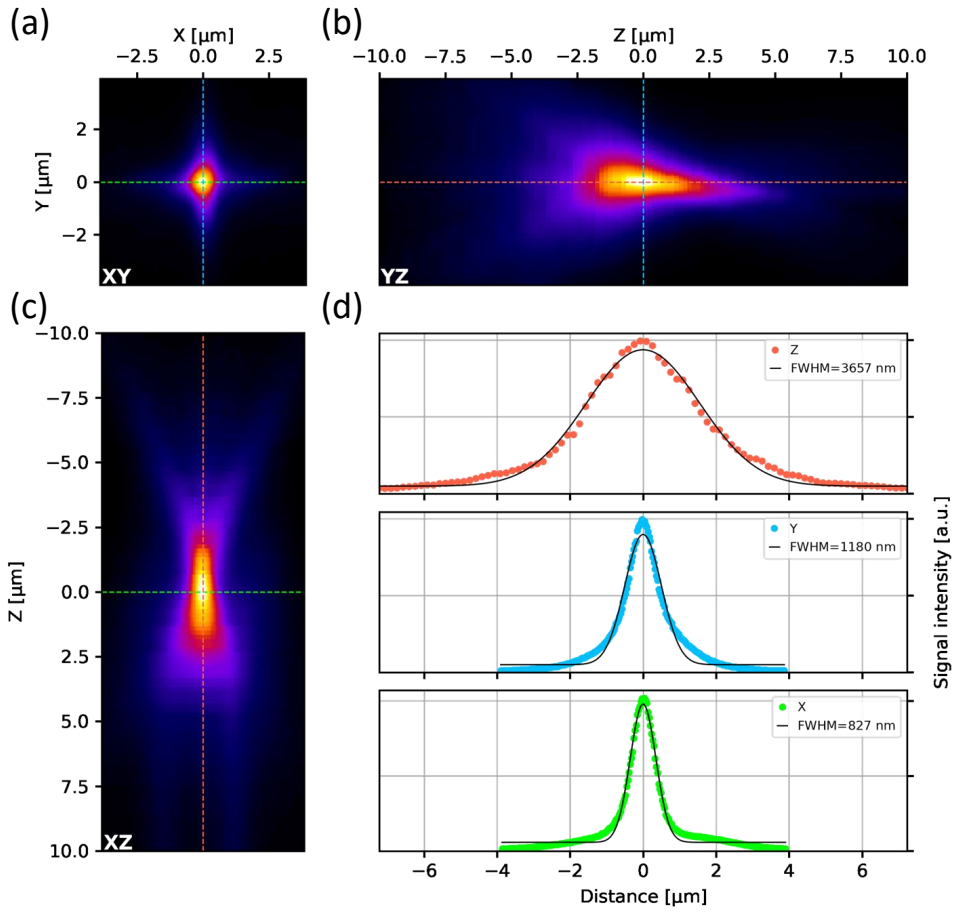

Figure 2.4: **Detection PSF measured from microspheres in green excitation channel.** (a) xy cross-sections of the extracted average PSF. (b) yz cross-sections of the extracted average PSF. (c) xz cross-sections of the extracted average PSF. (d) Line profiles are measured along the dashed lines plotted onto the sections quantify the PSF size along the three dimensions.

which corresponds to the convolution between the PSF of the holographic system and the PSF of the detection system.

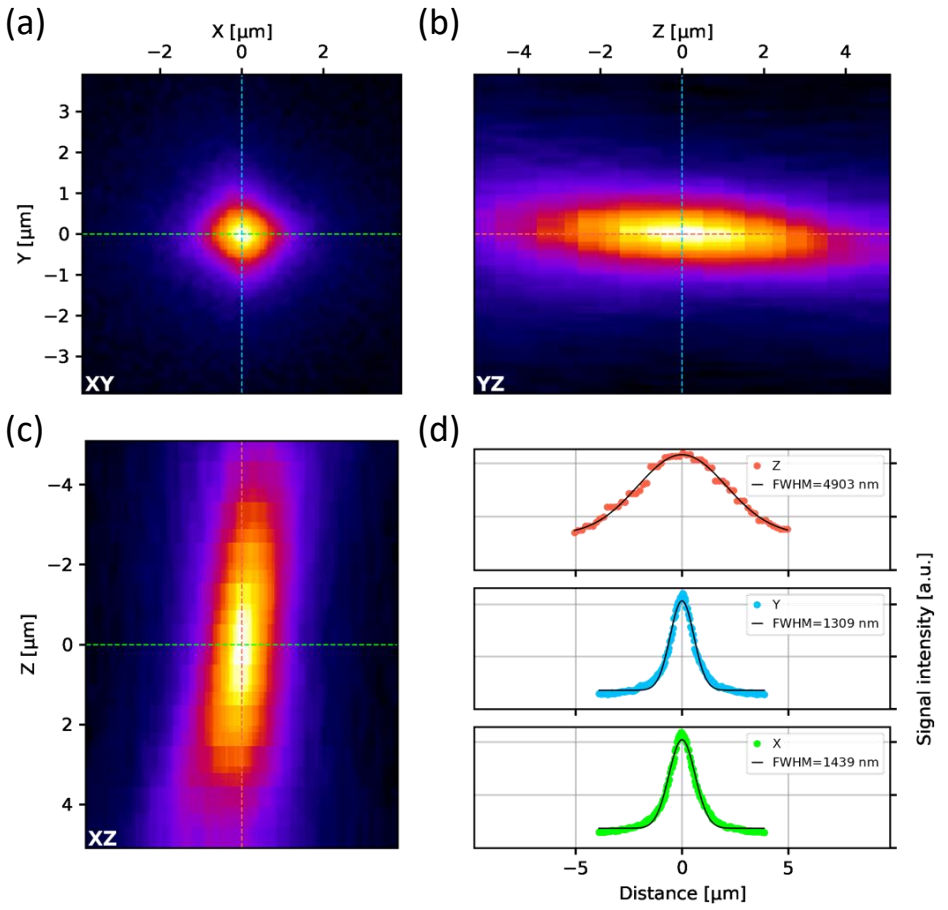

Figure 2.5: **Extracted PSF from CGH projected into liquid fluorescein.**(a) xy cross-sections of the extracted average PSF. (b) yz cross-sections of the extracted average PSF. (c) xz cross-sections of the extracted average PSF. (d) Line profiles are measured along the dashed lines plotted onto the sections quantify the PSF size along the three dimensions.

2.3.3. Workflow of light sheet optogenetics experiment

The general workflow for all-optical physiology experiment using the system described above would be similar to other methods described in this volume. After alignment of the system, it is typical to first acquire a baseline fluorescence image or a 3Dmovie to characterize anatomical structure, and possibly baseline activity. Then, the regions of interest (ROIs) to be stimulated are selected. The criteria to choose the ROIs from the baseline image are set by the experimenter and fed into an algorithm for targeting light, e.g., CGH calculation. Subsequently we program a pulse sequence encoding for the CGH where the stimulation light is temporally

gated by an external shutter. Afterwards the fluorescence signal is recorded over time.

Imaging larval zebrafish

After microscope alignment, mount a zebrafish in FEP tubing. Use brightfield illumination to orient and position the sample appropriately. Obtain a baseline fluorescence image. A high-resolution volume is recommended to help with brain registration later in image analysis. Based on anatomical or functional criteria, select ROIs for photostimulation. Generate the hologram(s) and set gating sequence or method to trigger the photostimulation sequence of interest.

Analysis of large-scale Ca^{2+} data set

Figure 2.6 shows the analysis of a representative data set measuring spontaneous neural activity in a 5 days past fertilization (dpf) zebrafish larvae expressing nuclear localized GCaMP6s in neurons, as acquired by volumetric calcium imaging on the described Bessel beam light sheet microscope. Fluorescence was captured in 20 volume sections of the forebrain, spaced 8 μm apart, with an acquisition rate of 0.67 Hz. Motion correction and the extraction of activity traces from individual neurons was implemented with the open-source calcium image analysis package CaImAn [63]. Motion artifacts were corrected through piece-wise rigid registration. Active neurons were then detected in the motion-corrected data through constrained non-negative matrix factorization (CNMF). To initialize CNMF, the images were filtered with a Gaussian kernel and the Pearson correlation with neighboring pixels and peak-to-noise ratio were calculated for each pixel (Fig. 2.6(a)). Local maxima in the point-wise product of the peak-to-noise ratio image and correlation image were used as initialization positions. With CNMF, the contours of found neurons (Fig. 2.6(b)) and activity traces (Fig. 2.6(c)) were then extracted. In total, 2077 active neurons were detected in the imaged brain volume (Fig. 2.6(d),(e))

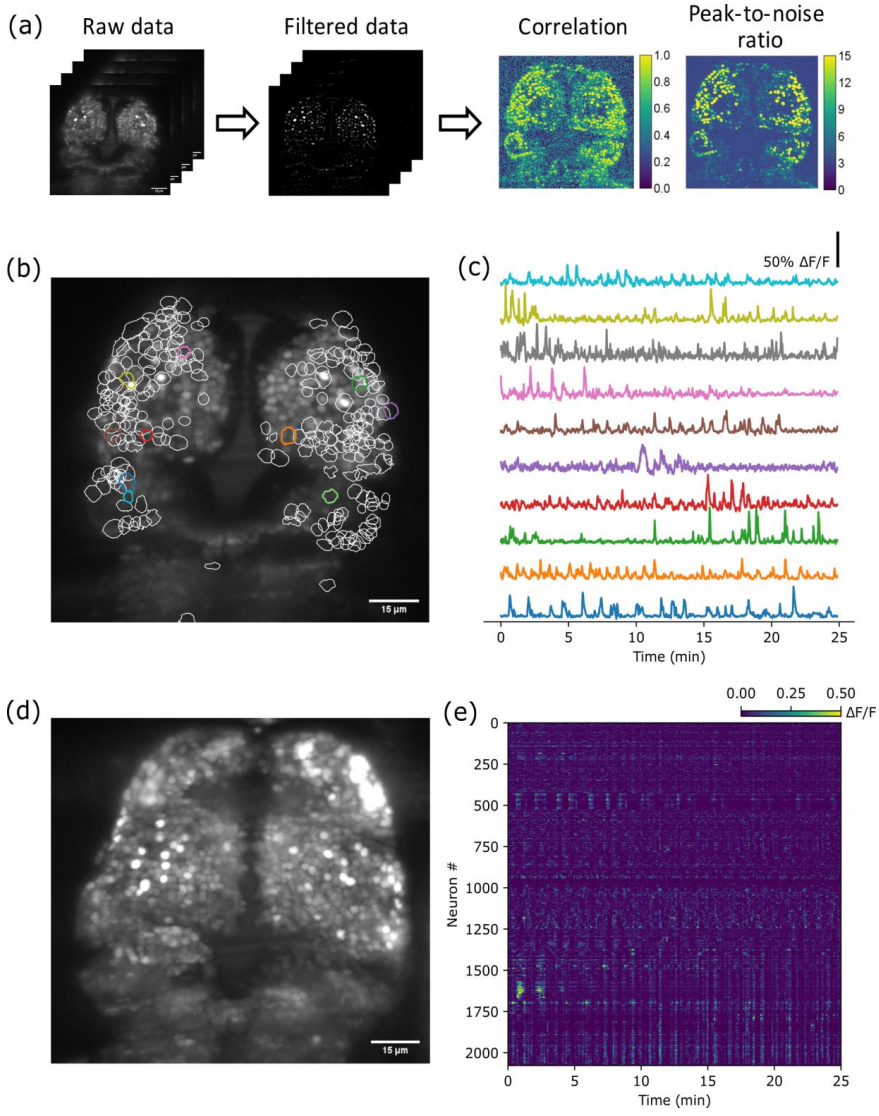

Figure 2.6: **Analysis of light-sheet calcium imaging data from the larval zebrafish forebrain with constrained non-negative matrix factorization (CNMF).** (a) Images were obtained from the forebrain of a larval zebrafish (5 dpf) expressing nuclear localized GCaMP6s. A total of 20 volume sections were imaged with Bessel beam light-sheet microscopy at an acquisition rate of 0.67 Hz. To detect neurons, CNMF was initialized by filtering the motion corrected time-series data with a Gaussian kernel and calculating the peak-to-noise ratio and Pearson correlation with 4 nearest neighboring pixels. Local maxima in the point-wise product of the peak-to-noise ratio image and correlation image were then used as initialization positions. (b) Contours of neurons extracted with CNMF in a single section. (c) The fluorescence ($\Delta F/F$) signals of 10 randomly selected neurons. (d) Maximum intensity projection of the measured volume (e) Activity map of 2077 fluorescence traces from neurons found in all sections clustered by correlation coefficient.

2.3.4. Choice of CGH algorithm

The 2P-CGH module shown in Fig. 3.1(a) is based on Fourier holography and requires an appropriate algorithm to calculate the desired phase hologram. The aim of CGH algorithms is to retrieve the phase mask, namely the phase of the hologram field U_h, to address the SLM by knowing the field U_o of the target at the image plane, where these fields are one the Fourier transform of the other. To generate a hologram of ROIs distributed in 3D, we compute a 3D hologram corresponding to a field U_o defined at different depths z as schematically described in Fig. 2.7(a). Optically the Fourier transform of the field U_h is realised through the objective lens when the SLM is conjugated to the objective back aperture through a telescope (L3 and L4 in Fig. 3.1(a)).

The choice of the algorithm to calculate CGHs depends on several considerations. Ideally, the algorithm provides high diffraction efficiency, uniformity over the volume of interest, and accuracy between the target and the reconstructed hologram. The algorithm should also be fast given the real-time nature of optogenetic experiments. The shape and dimensions of the target photostimulation pattern also influence the choice of CGH algorithm. When the target object has a complex and extended lateral shape (> 1 μm) image-based algorithms are employed. They enable the generation of extremely complex illumination patterns in very short times however they are limited to illumination light focused on a limited number of two-dimensional planes [64]. Conversely, point-cloud algorithms allow one to target diffraction-limited spots arbitrarily distributed in the three-dimensional FOV of the optical system.

Many variations of these algorithms have been developed. Here we classify them in two categories (see Appendix 2.A.2): classic algorithms, and more recent algorithms developed specifically for optogenetics applications. Random superposition (RS) and Gerchberg-Saxton (GS) [65, 66] are the most known algorithms. The first offers high speed but poor quality of the CGH in terms of uniformity and efficiency, whereas the second provides improved quality with an increased computational time. Recently new algorithms have been developed that are optimized for speed, such as a compressive sensing version of the Gerchberg-Saxton algorithm [67]. Here the compressive sensing method allows to reduce the computational time by a factor of 10 without impairing the quality of the CGH achieved with the standard implementation of Gerchberg-Saxton. Another advanced algorithm recently available is computer-generated holography by non-convex optimization [64]. Arbitrary 3D holograms are generated through non-convex optimization of custom cost functions. Another advanced algorithm recently developed, called DeepCGH [68], is based on unsupervised convolutional neural networks. Holograms computed via DeepCGH showed improved computational times and high efficiency suitable for neurostimulation experiments.

As an example, in the high-NA configuration hereby described we implement Weighted Gerchberg-Saxton (WGS) algorithm to generate stimulation ROIs with a lateral dimension between $\sim$ 6 - 10 μm, on the order of the size of small neurons in the larval zebrafish brain. The principle of this approach is schematically described in Fig. 2.7 (b), while Fig.2.7 (d) shows a 3D view of an extended CGH projected into

a thick Rhodamine slide. On the other hand, when targeting sub-cellular regions, the Compressive Sensing Weighted Gerchberg-Saxton algorithm is faster, but the lateral extension of the CGH depends on the numerical aperture of the detection objective. In the case that $NA = 1.0$ the lateral extension of the spots is on the order of ~ 1 µm. Similarly to the previous case, Fig.2.7 (c) illustrates the principle of point-cloud CGH and panel 2.7 (e) shows a 3D view of the point-cloud CGH. The Compressive sensing weighted Gerchberg-Saxton (CS-WGS) algorithm provides comparable results in terms of spot brightness and uniformity as the point-clouds generated by the GS and WGS approaches, while reducing drastically the computational time [67].

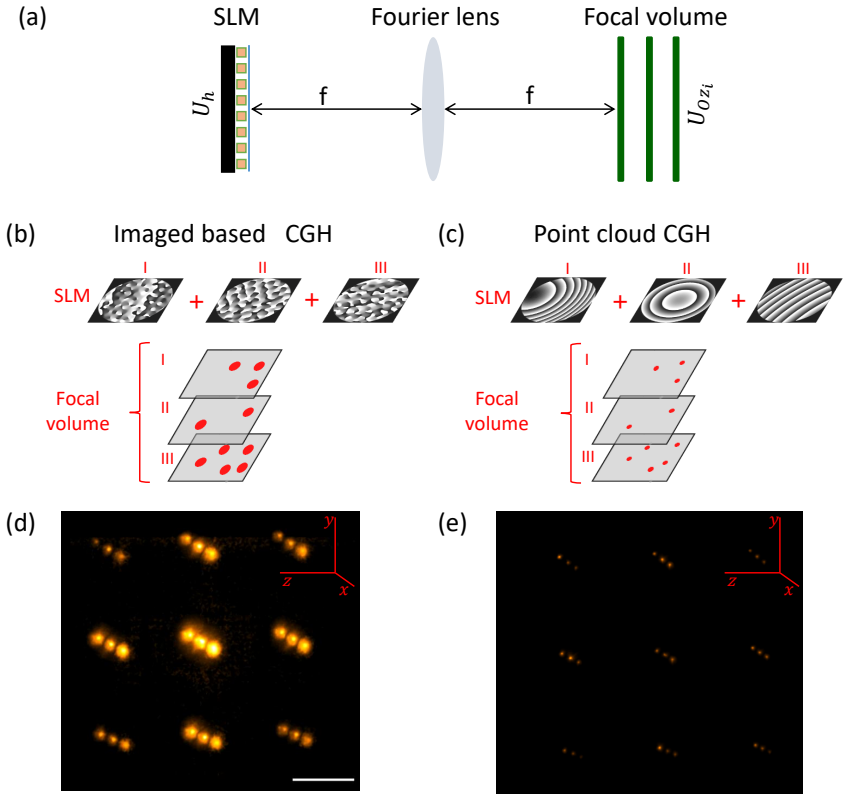

Figure 2.7: **CGH approach** (a) Optical transformation needed to project a 3D CGH. U_h represents the spatial Fourier transform of the desired pattern U_{ozi} defined at different depths. f is the focal length of the lens (middle element).(b) Scheme of algorithms for extended CGH. Phase masks producing different features at focal planes I, II, III are combined by superposition principle at the SLM. Each of the three phase masks is calculated based on the corresponding image at the focal plane.(c) Scheme of algorithms for point-cloud CGH. Phase masks producing different features at focal planes I, II, III are combined by superposition principle at the SLM. Each of the three phase masks is calculated based on the coordinates xyz of the spots at the focal plane.(d) 3D view of image based CGH of a grid 160 × 160 × 100 µm (e) 3D view of point-cloud CGH of the same grid.

2.3.5. Effect of aberrations on CGH

All algorithms previously described compute CGHs based on the assumption that the sample has uniform index of refraction. This assumption is rarely true in neuroscience since brain tissue is generally optically turbid and non uniform. Optical inhomogeneities of samples cause a distortion of the stimulation pattern known as optical aberrations. In Fig. 2.8 we show the effect of optical aberrations on a point cloud CGH. Specifically to the computed CGH phase, we summed a phase encoding for horizontal coma aberration with progressively increasing coefficient. The aberrated CGH has a decreased intensity and it is displaced from its original position. Sample induced aberrations can be compensated through adaptive optics techniques using the SLM as an adaptive element

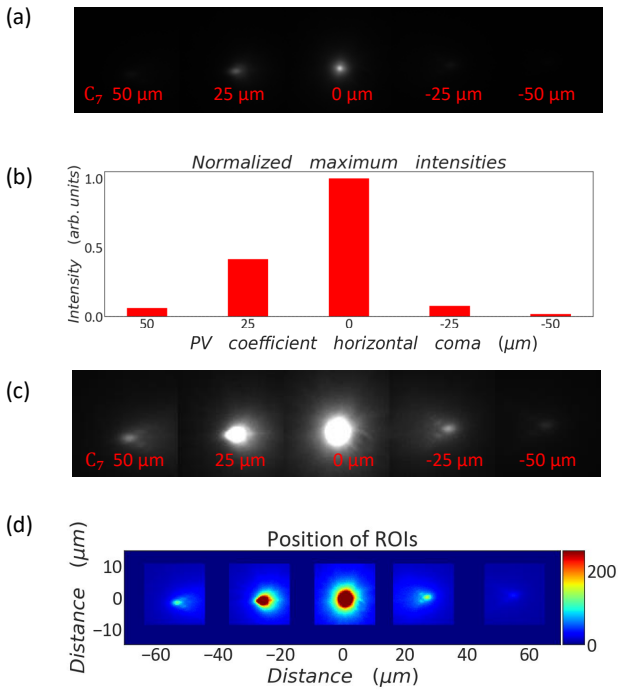

Figure 2.8: **Effect of coma on CGH** a) TPE fluorescence induced onto a Rhodamine slide by a one-point hologram with progressively increasing horizontal coma coefficient. Subscripts on the images indicate the corresponding peak-to-valley (PV) coefficient in units of the wavelength of horizontal coma.The additional coma phase introduces a dramatic drop in the fluorescence intensity compared to the case without aberrations (0 µm PV coefficient). (b) Bar plot showing the maximum intensity of each aliased fluorescent spot in a. Intensities are normalized to the maximum intensity of the aberration-free spot (0 µm PV coefficient). The maximum intensity is reduced below 50 % compared to the intensity of the aberration-free spot. (c) Same fluorescence images showed in a) where the aberrated spots intensity are enhanced by a constant factor. (d) Maximum intensity projection of the fluorescence images in b) showing the position of each point across the camera chip. The aberration besides the loss of intensity introduces a loss of the CGH fidelity.

2.4. Summary

Optogenetic manipulation coupled to light sheet imaging is a powerful tool to perturb and monitor living translucent samples such as zebrafish larvae. Light sheet imaging can be realized in different flavors with emphasis on balancing optical sectioning with the dimensions of the FOV and maximizing the imaging speed to resolve fast dynamics as reported in section 2.1.1. Here the light sheet is realized by scanning a Bessel beam in a 2D plane. This illumination offers a more uniform illumination over the FOV compared to Gaussian beams and a reduced scattering thanks to the self-healing properties of Bessel beams. However a major drawback is the presence of the side-lobes of Bessel profiles. In our microscope design the side lobes are electronically rejected by implementing a confocal slit detection of the fluorescent signal. Unfortunately this solution sacrifices the imaging speed. To improve this aspect an interesting future upgrade of our imaging system is the implementation of a NIR light source. In fact, 2P excitation can successfully mitigate the fluorescence induced by the side lobes as reported in [44]. Moreover, NIR wavelengths are often preferred for brain imaging of zebrafish larvae due to their orthogonality to the visual system of the animal [2].The photostimulation module exploits the high NA of the light sheet detection objective to focus on the sample 2P-CGHs. Those offer flexibility to illuminate either sub-cellular ROIs with dimensions in the order of the light diffraction limit or whole cell-bodies extending over several microns ($\approx$ 6-10 μm). In the first case optical aberrations due to tissue inhomogeneities are a limiting factor to reach diffraction limited resolution. Hence, a next step in further developing the 2P-CGH technique is to include adaptive optics methods to compensate for tissue-induced aberrations using the SLM as corrective element. Another improvement could be to include temporal focusing in the 2P holography module [69] to increase the axial confinement of the stimulation light.

References

[1] W. C. Lemon, S. R. Pulver, B. Höckendorf, K. McDole, K. Branson, J. Freeman, and P. J. Keller, "Whole-central nervous system functional imaging in larval Drosophila," *Nature Communications*, vol. 6, no. 7924, 2015.

[2] G. C. Vanwalleghem, M. B. Ahrens, and E. K. Scott, "Integrative whole-brain neuroscience in larval zebrafish," *Current Opinion in Neurobiology*, vol. 50, pp. 136–145, 2018.

[3] M. D. Loring, E. E. Thomson, and E. A. Naumann, "Whole-brain interactions underlying zebrafish behavior," *Current Opinion in Neurobiology*, vol. 65, pp. 88–99, 2020.

[4] C. Eschbach and M. Zlatic, "Useful road maps: studying Drosophila larva's central nervous system with the help of connectomics," *Current Opinion in Neurobiology*, vol. 65, 2020.

[5] P. J. Keller and M. B. Ahrens, "Visualizing whole-brain activity and development

at the single-cell level using light-sheet microscopy," *Neuron*, vol. 85, no. 3, pp. 462–483, 2015.

[6] M. B. Ahrens, M. B. Orger, D. N. Robson, J. M. Li, and P. J. Keller, "Whole-brain functional imaging at cellular resolution using light-sheet microscopy," *Nature Methods*, vol. 10, no. 5, pp. 413–420, 2013.

[7] M. Lovett-Barron, "Learning-dependent neuronal activity across the larval zebrafish brain," *Current Opinion in Neurobiology*, vol. 67, pp. 42–49, 2021.

[8] L. Fenno, O. Yizhar, and K. Deisseroth, "The Development and Application of Optogenetics," *Annual Review of Neuroscience*, vol. 34, no. 1, pp. 389–412, 2011.

[9] H. E. Johnson and J. E. Toettcher, "Illuminating developmental biology with cellular optogenetics," *Current Opinion in Biotechnology*, vol. 52, pp. 42–48, 2018.

[10] R. H. Kramer, A. Mourot, and H. Adesnik, "Optogenetic pharmacology for control of native neuronal signaling proteins," *Nature Neuroscience*, vol. 16, no. 7, pp. 816–823, 2013.

[11] R. A. Hill, E. C. Damisah, F. Chen, A. C. Kwan, and J. Grutzendler, "Targeted two-photon chemical apoptotic ablation of defined cell types in vivo," *Nature Communications*, vol. 8, 6 2017.

[12] G. de Medeiros, D. Kromm, B. Balazs, N. Norlin, S. Günther, E. Izquierdo, P. Ronchi, S. Komoto, U. Krzic, Y. Schwab, F. Peri, S. de Renzis, M. Leptin, M. Rauzi, and L. Hufnagel, "Cell and tissue manipulation with ultrashort infrared laser pulses in light-sheet microscopy," *Scientific Reports*, vol. 10, no. 1, pp. 1–12, 2020.

[13] V. Emiliani, A.E. Cohen, K. Deisseroth, and M. Häusser., "Symposium All-Optical Interrogation of Neural Circuits," *Journal of Neuroscience*, vol. 35, no. 41, pp. 13917–13926, 2015.

[14] T. Knöpfel, "Genetically encoded optical indicators for the analysis of neuronal circuits," *Nature Reviews Neuroscience*, vol. 13, no. 10, pp. 687–700, 2012.

[15] F. St-Pierre, J. D. Marshall, Y. Yang, Y. Gong, M. J. Schnitzer, and M. Z. Lin, "High-fidelity optical reporting of neuronal electrical activity with an ultrafast fluorescent voltage sensor," *Nature Neuroscience*, vol. 17, no. 6, pp. 884–889, 2014.

[16] K. Asakawa and K. Kawakami, "Targeted gene expression by the Gal4-UAS system in zebrafish," *Development Growth and Differentiation*, vol. 50, no. 6, pp. 391–399, 2008.

[17] P. Antinucci, A. Dumitrescu, C. Deleuze, H. J. Morley, K. Leung, T. Hagley, F. Kubo, H. Baier, I. H. Bianco, and C. Wyart, "A calibrated optogenetic toolbox of stable zebrafish opsin lines," *eLife*, vol. 9, no. e54937, 2020.

[18] B. R. Rost, F. Schneider-Warme, D. Schmitz, and P. Hegemann, "Optogenetic Tools for Subcellular Applications in Neuroscience," *Neuron*, vol. 96, pp. 572–603, 11 2017.

[19] C. Pantoja, A. Hoagland, E. C. Carroll, V. Karalis, A. Conner, and E. Y. Isacoff, "Neuromodulatory Regulation of Behavioral Individuality in Zebrafish," *Neuron*, vol. 91, no. 3, pp. 587–601, 2016.

[20] "https://openspim.org/."

[21] Y. Wan, K. McDole, and P. J. Keller, "Light-sheet microscopy and its potential for understanding developmental processes," *Annual Review of Cell and Developmental Biology*, vol. 35, pp. 655–681, 2019.

[22] R. M. Power and J. Huisken, "A guide to light-sheet fluorescence microscopy for multiscale imaging," *Nature Methods*, vol. 14, no. 4, pp. 360–373, 2017.

[23] J. Huisken, J. Swoger, F. Del Bene, J. Wittbrodt, and E. H. Stelzer, "Optical sectioning deep inside live embryos by selective plane illumination microscopy," *Science*, vol. 305, no. 5686, pp. 56–86, 2004.

[24] P. J. Verveer, J. Swoger, F. Pampaloni, K. Greger, M. Marcello, and E. H. Stelzer, "High-resolution three-dimensional imaging of large specimens with light sheet-based microscopy," *Nature Methods*, vol. 4, no. 4, pp. 311–313, 2007.

[25] P. J. Keller, A. D. Schmidt, J. Wittbrodt, and E. H. Stelzer, "Reconstruction of zebrafish early embryonic development by scanned light sheet microscopy," *Science*, vol. 322, no. 5904, pp. 1065–1069, 2008.

[26] L. Gao, "Extend the field of view of selective plan illumination microscopy by tiling the excitation light sheet," *Optics Express*, vol. 23, no. 5, pp. 6102–6111, 2015.

[27] N. Vladimirov, C. Wang, B. Höckendorf, A. Pujala, M. Tanimoto, Y. Mu, C. T. Yang, J. D. Wittenbach, J. Freeman, S. Preibisch, M. Koyama, P. J. Keller, and M. B. Ahrens, "Brain-wide circuit interrogation at the cellular level guided by online analysis of neuronal function," *Nature Methods*, vol. 15, no. 12, pp. 1117–1125, 2018.

[28] R. K. Chhetri, F. Amat, Y. Wan, B. Höckendorf, W. C. Lemon, and P. J. Keller, "Whole-animal functional and developmental imaging with isotropic spatial resolution," *Nature Methods*, vol. 12, no. 12, pp. 1171–1178, 2015.

[29] L. A. Royer, W. C. Lemon, R. K. Chhetri, and P. J. Keller, "A practical guide to adaptive light-sheet microscopy," *Nature Protocols*, vol. 13, no. 11, pp. 2462–2500, 2018.

[30] C. Dunsby, "Optically sectioned imaging by oblique plane microscopy," *Optics Express*, vol. 16, no. 25, pp. 20306–20316, 2008.

[31] M. B. Bouchard, V. Voleti, C. S. Mendes, C. Lacefield, W. B. Grueber, R. S. Mann, R. M. Bruno, and E. M. Hillman, "Swept confocally-aligned planar excitation (SCAPE) microscopy for high-speed volumetric imaging of behaving organisms," *Nature Photonics*, vol. 9, no. 2, pp. 113–119, 2015.

[32] E. M. Hillman, V. Voleti, W. Li, and H. Yu, "Light-Sheet Microscopy in Neuroscience," *Annual Review of Neuroscience*, vol. 42, pp. 295–313, 2019.

[33] R. Strack, "Single-objective light sheet microscopy," *Nature Methods*, vol. 18, no. 28, 2021.

[34] R. Galland, G. Grenci, A. Aravind, V. Viasnoff, V. Studer, and J. B. Sibarita, "3D high-and super-resolution imaging using single-objective SPIM," *Nature Methods*, vol. 12, no. 7, pp. 641–644, 2015.

[35] M. B. M. Meddens, S. Liu, P. S. Finnegan, T. L. Edwards, C. D. James, and K. A. Lidke, "Single objective light-sheet microscopy for high-speed whole-cell 3D super-resolution," *Biomedical Optics Express*, vol. 7, no. 6, pp. 2219–2236, 2016.

[36] R. Tomer, M. Lovett-Barron, I. Kauvar, A. Andalman, V. M. Burns, S. Sankaran, L. Grosenick, M. Broxton, S. Yang, and K. Deisseroth, "SPED Light Sheet Microscopy: Fast Mapping of Biological System Structure and Function," *Cell*, vol. 163, no. 7, 2015.

[37] S. Quirin, N. Vladimirov, C.-T. Yang, D. S. Peterka, R. Yuste, and M. B. Ahrens, "Calcium imaging of neural circuits with extended depth-of-field light-sheet microscopy," *Optics Letters*, vol. 41, no. 5, pp. 855–858, 2016.

[38] T. V. Truong, D. B. Holland, S. Madaan, A. Andreev, K. Keomanee-Dizon, J. V. Troll, D. E. Koo, M. J. McFall-Ngai, and S. E. Fraser, "High-contrast, synchronous volumetric imaging with selective volume illumination microscopy," *Communications Biology*, vol. 3, no. 74, pp. 1–8, 2020.

[39] E. Sapoznik, B. J. Chang, R. J. Ju, E. S. Welf, D. Broadbent, A. F. Carisey, S. J. Stehbens, K. M. Lee, A. Marín, A. B. Hanker, J. C. Schmidt, C. L. Arteaga, B. Yang, R. Kruithoff, D. P. Shepherd, A. Millett-Sikking, A. G. York, K. M. Dean, and R. Fiolka, "A single-objective light-sheet microscope with 200 nm-scale resolution," *bioRxiv*, 2020.

[40] Jerome Mertz, "Optical sectioning microscopy with planar or structured illumination," *Nature Methods*, vol. 8, no. 10, pp. 811–819, 2011.

[41] M. Jemielita, M. J. Taormina, A. Delaurier, C. B. Kimmel, and R. Parthasarathy, "Comparing phototoxicity during the development of a zebrafish craniofacial bone using confocal and light sheet fluorescence microscopy techniques," *Journal of Biophotonics*, vol. 6, no. 11-12, pp. 920–928, 2013.

[42] T. A. Planchon, L. Gao, D. E. Milkie, M. W. Davidson, J. A. Galbraith, C. G. Galbraith, and E. Betzig, "Rapid three-dimensional isotropic imaging of living cells using Bessel beam plane illumination," *Nature Methods*, vol. 8, no. 5, pp. 417–423, 2011.

[43] L. Gao, L. Shao, C. D. Higgins, J. S. Poulton, M. Peifer, M. W. Davidson, X. Wu, B. Goldstein, and E. Betzig, "Noninvasive imaging beyond the diffraction limit of 3D dynamics in thickly fluorescent specimens," *Cell*, vol. 151, no. 6, pp. 1370–1385, 2012.

[44] F. O. Fahrbach, V. Gurchenkov, K. Alessandri, P. Nassoy, and A. Rohrbach, "Light-sheet microscopy in thick media using scanned Bessel beams and two-photon fluorescence excitation," *Optics Express*, vol. 21, no. 11, pp. 13824–13839, 2013.

[45] B. C. Chen, W. R. Legant, K. Wang, L. Shao, D. E. Milkie, M. W. Davidson, C. Janetopoulos, X. S. Wu, J. A. Hammer, Z. Liu, B. P. English, Y. Mimori-Kiyosue, D. P. Romero, A. T. Ritter, J. Lippincott-Schwartz, L. Fritz-Laylin, R. D. Mullins, D. M. Mitchell, J. N. Bembenek, A. C. Reymann, R. Böhme, S. W. Grill, J. T. Wang, G. Seydoux, U. S. Tulu, D. P. Kiehart, and E. Betzig, "Lattice light-sheet microscopy: Imaging molecules to embryos at high spatiotemporal resolution," *Science*, vol. 346, no. 6208, 2014.

[46] T. L. Liu, S. Upadhyayula, D. E. Milkie, V. Singh, K. Wang, I. A. Swinburne, K. R. Mosaliganti, Z. M. Collins, T. W. Hiscock, J. Shea, A. Q. Kohrman, T. N. Medwig, D. Dambournet, R. Forster, B. Cunniff, Y. Ruan, H. Yashiro, S. Scholpp, E. M. Meyerowitz, D. Hockemeyer, D. G. Drubin, B. L. Martin, D. Q. Matus, M. Koyama, S. G. Megason, T. Kirchhausen, and E. Betzig, "Observing the cell in its native state: Imaging subcellular dynamics in multicellular organisms," *Science*, vol. 360, no. 6386, 2018.

[47] E. Baumgart and U. Kubitscheck, "Scanned light sheet microscopy with confocal slit detection," *Optics Express*, vol. 20, no. 19, pp. 21805–21814, 2012.

[48] M. dal Maschio, J. C. Donovan, T. O. Helmbrecht, and H. Baier, "Linking Neurons to Network Function and Behavior by Two-Photon Holographic Optogenetics and Volumetric Imaging," *Neuron*, vol. 94, no. 4, pp. 774–789, 2017.

[49] C. McRaven, D. Tanese, L. Zhang, C.-T. Yang, M. Ahrens, V. Emiliani, and M. Koyama, "High-throughput cellular-resolution synaptic connectivity mapping in vivo with concurrent two-photon optogenetics and volumetric Ca 2+ imaging," *bioRxiv*, 2020.

[50] K. Ko and E. Nig, "Multiphoton microscopy in life sciences," *Journal of Microscopy*, vol. 200, no. 2, pp. 83–104, 2000.

[51] W. Supatto, T. V. Truong, D. Débarre, and E. Beaurepaire, "Advances in multiphoton microscopy for imaging embryos," *Current Opinion in Genetics and Development*, vol. 21, no. 5, pp. 538–548, 2011.

[52] T. V. Truong, W. Supatto, D. S. Koos, J. M. Choi, and S. E. Fraser, "Deep and fast live imaging with two-photon scanned light-sheet microscopy," *Nature Methods*, vol. 8, no. 9, pp. 757–762, 2011.

[53] S. Wolf, W. Supatto, G. Debrégeas, P. Mahou, S. G. Kruglik, J. M. Sintes, E. Beaurepaire, and R. Candelier, "Whole-brain functional imaging with two-photon light-sheet microscopy," *Nature Methods*, vol. 12, no. 5, pp. 379–380, 2015.

[54] Diaspro Alberto and Robello Mauro, "Two-photon excitation of fluorescence for three-dimensional opticalimaging of biological structures," *Journal of Photochemistry and Photobiology B: Biology*, vol. 5, pp. 1–8, 2 200.

[55] A. Picot, S. Dominguez, C. Liu, I. W. Chen, D. Tanese, E. Ronzitti, P. Berto, E. Papagiakoumou, D. Oron, G. Tessier, B. C. Forget, and V. Emiliani, "Temperature Rise under Two-Photon Optogenetic Brain Stimulation," *Cell Reports*, vol. 24, no. 5, pp. 1243–1253, 2018.

[56] E. Papagiakoumou, E. Ronzitti, I. W. Chen, M. Gajowa, A. Picot, and V. Emiliani, "Two-photon optogenetics by computer-generated holography," in *Neuromethods*, vol. 133, pp. 175–197, Humana Press Inc., 2018.

[57] D. E. Martin Persson and M. Goksör, "Reducing the effect of pixel crosstalk in phase only spatial light modulators," *Optics express*, vol. 20, no. 20, pp. 22334–22343, 2012.

[58] A. Kaufmann, M. Mickoleit, M. Weber, and J. Huisken, "Multilayer mounting enables long-term imaging of zebrafish development in a light sheet microscope," *Development*, vol. 139, no. 17, pp. 3242–3247, 2012.

[59] L. Nhu, X. Wang, Y. Liu, C. Kuang, and X. Liu, "Light sheet microscopy with high spatial resolution based on polarized structured illumination beam modulated by the phase mask," *Microscopy Research and Technique*, vol. 81, no. 9, pp. 959–965, 2018.

[60] R. S. Fischer, Y. Wu, P. Kanchanawong, H. Shroff, and C. M. Waterman, "Microscopy in 3D: A biologist's toolbox," *Trends in Cell Biology*, vol. 21, no. 12, pp. 682–691, 2011.

[61] R. W. Cole, T. Jinadasa, and C. M. Brown, "Measuring and interpreting point spread functions to determine confocal microscope resolution and ensure quality control," *Nature Protocols*, vol. 6, no. 12, pp. 1929–1941, 2011.

[62] "https://github.com/hoogenboom-group/PSF-Extractor/."

[63] A. Giovannucci, J. Friedrich, P. Gunn, J. Kalfon, B. L. Brown, S. A. Koay, J. Taxidis, F. Najafi, J. L. Gauthier, P. Zhou, B. S. Khakh, D. W. Tank, D. B. Chklovskii, and E. A. Pnevmatikakis, "CaImAn an open source tool for scalable calcium imaging data analysis," *eLife*, vol. 8, 2019.

[64] J. Zhang, N. Pégard, J. Zhong, H. Adesnik, and L. Waller., "3D computer-generated holography by non-convex optimization," *Optica*, vol. 4, no. 10, pp. 1306–1313, 2017.

[65] R. W. Gerchberg and W. O. Saxton, "A Practical Algorithm for the Determination of Phase from Image and Diffraction Plane Pictures," *Optik*, vol. 35, no. 2, pp. 337–246, 1972.

[66] R. Di Leonardo, F. Ianni, and G. Ruocco, "Computer generation of optimal holograms for optical trap arrays," *Optics Express*, vol. 15, no. 4, pp. 169–175, 2007.

[67] P. Pozzi, L. Maddalena, N. Ceffa, O. Soloviev, G. Vdovin, E. Carroll, and M. Verhaegen, "Fast Calculation of Computer Generated Holograms for 3D Photostimulation through Compressive-Sensing Gerchberg–Saxton Algorithm," *Methods and Protocols*, vol. 2, no. 1, pp. 2–15, 2018.

[68] M. Hossein Eybposh, N. W. Caira, M. Atisa, P. Chakravarthula, and N. C. Pégard, "DeepCGH: 3D computer-generated holography using deep learning," *Optics Express*, vol. 28, no. 18, p. 26636, 2020.

[69] D. Oron, E. Papagiakoumou, F. Anselmi, and V. Emiliani, "Two-photon optogenetics," *Progress in Brain Research*, vol. 196, pp. 119–143, 2012.

2.A. Appendix

2.A.1. Microscope alignment

Align the light-sheet module

The microscope is aligned by visualizing the Bessel beam profile. By using the galvanometric mirror G1, responsible for the planar scan, we can image the full profile of the Bessel beam at specific locations.

1. Prepare a low concentration solution of fluorescent dye such as fluorescein (Invitrogen, F1300) diluted in demineralized water.

2. Fill the sample chamber with the fluorescent solution and turn on the excitation laser at low power (1 mW).

3. Optimize the beam thickness and uniformity in the center of the FOV by setting the galvanometric mirror G1 at 0 V.

4. Optimize the beam focus at the edges of the FOV by setting the galvanometric mirror G1 at its extrema, e.g., $\pm$ 1 V. For steps 3 and 4, the galvanometric mirror G2 and the ETL voltages are kept to 0 V. These settings ensure that the axial scanning range is centered. As schematically shown in Figure A1a, a properly aligned Bessel beam appears as a tiny, bright, and straight line profile across the FOV. The inset shows a zoom-in on a good example of Bessel beam where a sharp profile with side lobes can be observed. Contrarily, Figure A1b shows an example of a misaligned Bessel beam. It is prominently tilted at the edges of the FOV and its profile is enlarged.

5. Perform an automated calibration to acquire a planar scan. The planar calibration correlates the vertical displacement of the Bessel beam across the planar FOV and the voltage given to the galvanometric mirror G1. During this calibration, sequentially change the voltages driving G1 and for each voltage measure the position of the Bessel beam onto the camera. The resulting data are voltages as a function of position. The slope of the linear fit on these data yields the relation between voltage and displacement.

6. Perform the volumetric calibration. This step allows to synchronize the displacement of the Bessel beam in the volumetric FOV with the ETL focal plane. This is achieved by sequentially changing the voltages fed to both the galvanometric mirror G2 and the ETL. For each ETL voltage, scan the full range with G2 and collect an image at each step. For each image, measure the maximum intensity of the central lobe of the Bessel beam. Select the value of G2 corresponding to this maximum to get the excitation profile in focus.

Align the 2P-CGH module

The 2P-CGH module is aligned by projecting the zero-order diffraction beam into the same fluorescent solution used for the light sheet alignment.

1. Align the NIR beam to impinge on the SLM with a small ($\sim 5°$) angle and to uniformly illuminate the whole SLM chip.

2. Check that the reflection of the zero-order beam from the SLM is well-separated from the incoming beam and that these beams have the same height.

3. Center the zero-order diffracted beam onto the irises placed in front of the downstream optics.

4. Check the position of the beam at the sample using the sCMOS camera. The beam must appear as a bright spot in the middle of the camera FOV. If this spot appears far away from the center of the camera, adjustments in the upstream optics are needed.

5. Install the inverse pinhole in the optical path and visualize a CGH projected into the sample.

6. Calibrate the 2P-CGH module with the ETL voltages. For this, load a series of single-point CGHs with different z position onto the SLM. For each CGH, adjust the voltage on the ETL and acquire an image of the two-photon excited fluorescence (TPEF) produced by the CGH. Record the second moment of the spot intensity as function of the voltage on each image series. The voltage corresponding to the minimum second moment is considered the right voltage to have the point in focus. This procedure links the z position of a CGH to the optimal voltage needed for an image in focus.

Registration between light-sheet module and 2P-CGH module

1. Compensate for possible rotation and flip between the 2P-CGH and the light sheet coordinate system. In the setup shown in Figure 3.1 , the 2P-CGH coordinate system is rotated by $-90°$ and flipped vertically with respect to the imaging system because of the orientation of the SLM and the odd number of mirrors between the SLM and the DO back aperture.

2. Calculate a point cloud CGH of random spots spanning the volume relevant to the experiment by using $x'y'z'$ coordinates defined in the 2P-CGH system. In the specific case of the setup described here the volume is covering 140×140×200 μm (Figure 3.1b).

3. Project the CGH into a concentrated solution of fluorescent dyes.

4. Collect images of the TPEF induced by the CGH and measure the xyz spots position in the light-sheet system (Figure 3.1b)

5. Calculate the affine transformation matrix through least square minimization between the xyz and the $x'y'z'$ coordinates.

6. Align the xyz coordinates to the $x'y'z'$ by applying the affine transformation matrix.Linear affine transforms will account for all linear transformations between coordinates, including lateral and axial shifts, magnification mismatches (independently for all axes), rigid rotations and coordinates shearing. Nonlinear distortions, such as barrel or pincushion distortion, would require a more complex non-linear transform. Given that the FOV is limited to hundreds of microns, nonlinear effects rarely appear in a well-designed system, and a linear transform provides sufficient accuracy even for photostimulation of sub-micron structures. The linear affine transform matrix between homogeneous coordinates is represented by a $4x4$ matrix [1] however it is determined by only 12 values as the last row in the matrix is always defined as $\{0, 0, 0, 1\}$. Hence, the matrix can be determined though least square minimization between vectors X_i of the image coordinates and X'_i vectors of 12 SLM coordinates. The accuracy of the matrix estimation is improved using more than 12 coordinates

2.A.2. Algorithms for CGH

The mathematical approach to calculate a CGH differs based on whether we deal with image-based or point-cloud CGHs. To target complex and extended shapes spanning over few focal planes the electric field of the desired pattern per each focal plane is modelled as:

$$U_o(\xi, \eta, z) = u_o(\xi, \eta) e^{i\phi_z} \tag{2.4}$$

where u_o is the square root of the desired intensity at depth z and ϕ_z is a random phase. The hologram field is defined as the Fast Fourier transform (FFT) of the field U_o at each focal plane. Then the phase delay between the fields at different depths is optimized to get an interference pattern at the SLM plane as close as possible to the target illumination pattern. On the other hand for diffraction limited spots arbitrarily distributed in the three dimensional FOV the hologram field is defined as the wavefront generated by the coordinates x, y, z of the single spots in the focal planes. Hence, the field at the SLM is calculated as the superposition of the fields generating each single spot:

$$U_h = \sum_{n=1}^{N} u_{o,n} \cdot e^{-i\left(\frac{2\pi}{\lambda f}\cdot(x_n \cdot x' + y_n \cdot y') + \frac{z_n \pi}{\lambda^2 f^2}\cdot(x'^2 + y'^2) + \phi_n\right)} \tag{2.5}$$

where $u_{o,n}$ is the amplitude of the field of each spot at the focal plane, f is the focal length of the optical system and λ is the wavelength of the light source, x_n, y_n, z_n are the coordinates of the n desired spots in 3D space, ϕ_n are random phase values, x′ and y′ are the coordinates of each SLM pixel and ϕ_n is a constant term. This field can be related to the field at the focal plane via a Discrete Fourier transform (DFT) of the single spots. Also in this case the aim is to optimize the phase delay between the fields generating each single spot.

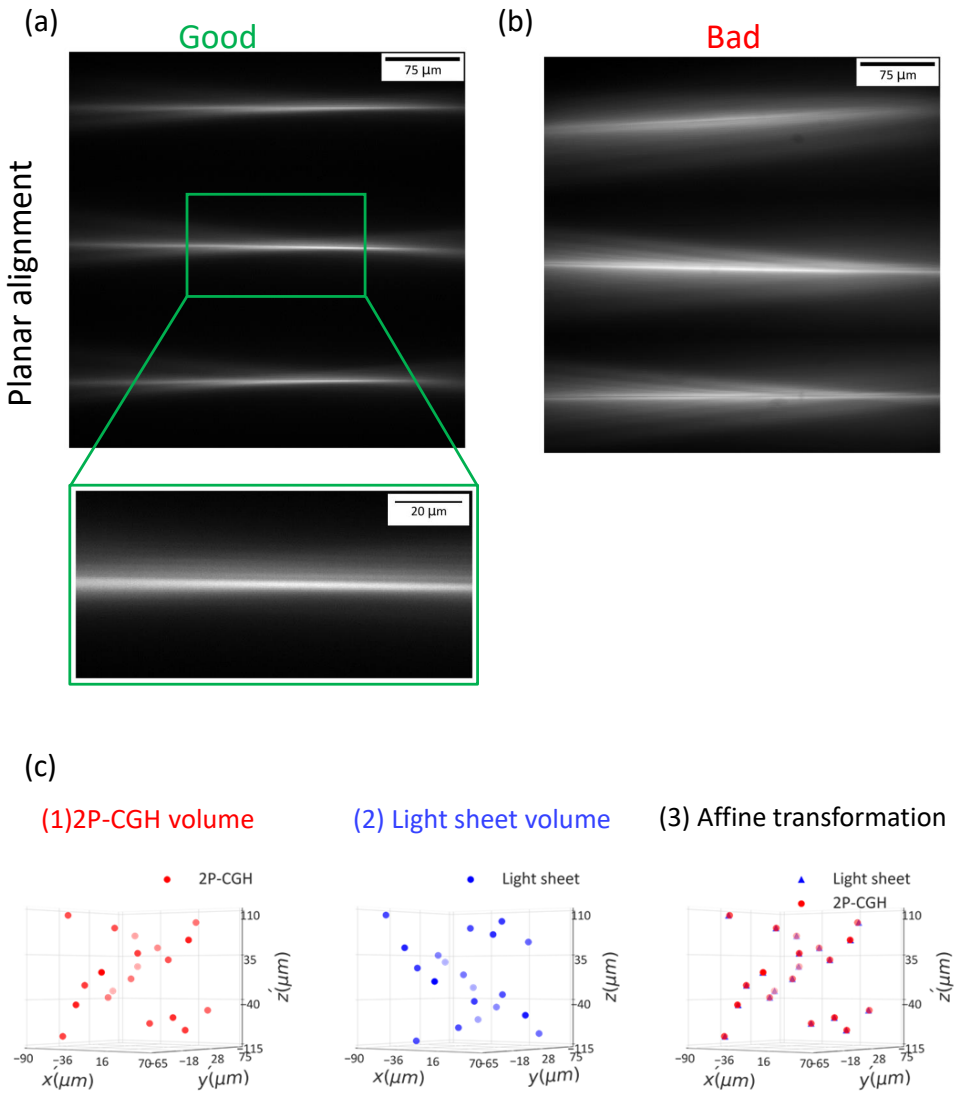

Figure A1: **Main steps of system alignment** (a)Example of good planar alignment. This image shows an overlay of the Bessel profile at different positions across the planar FOV. Inset shows a shallow Bessel beam with its side lobes. (b) Same image as in a) shows an example of misaligned beam across the planar FOV. (c) Affine transformation between Light-sheet and 2P-CGH module (1) 3D plot of the coordinates fed into the algorithm to generate a point cloud CGH of random points spanning over a 3D volume. These coordinates are defined in the coordinate system $x'y'z'$of the 2P-CGH module. (2) 3D plot of the coordinates measured on the TPEF image of the CGH. These coordinates are defined in the coordinate system xyz of the light-sheet module. (3) Result of the affine transformation between 2P-CGH coordinates and light sheet coordinates.

Classic CGH algorithms:

- **Random superposition (RS)**
  The electric field of the desired pattern per each focal plane is modelled as in equation 2.4. The hologram is calculated as the inverse Fourier transform of the field U_o and it is back propagated to the SLM plane according to the Fresnel propagator in Fourier Optics [2]. Then the interference field of all the holograms is computed. The phase of this interference field is the hologram retained as the phase mask to load onto the SLM. The average of the hologram fields at different depths is based on the assumption of independence between the depths. Thus, this method does not take into account the interference of the fields at different planes. This results in a degradation of the reconstructed holograms, which is evident when we project holograms with more than 2-3 depths [3]. This method is very fast compared to iterative algorithms.

- **Gerchberg-Saxton (GS**
  The electric field U_o of the desired pattern is modelled as in the previous algorithm. Then the hologram is calculated as the inverse Fourier transform of the object field U_o. In the resulting hologram field the phase is retained while the amplitude is substituted with a Gaussian amplitude. This new field undergoes another Fourier transform to produce the object field at the focal plane. The pattern produced at the focal plane is similar to the desired one but it has a decreased efficiency, hence the phase is kept while the amplitude is replaced with the one of the desired pattern. At this stage the inverse Fourier transform of the field is calculated to retrieve the phase mask at the SLM plane. This procedure is repeated iteratively until the algorithm converges to phase mask which produces the best intensity pattern.This algorithm can be implemented for 3D holograms including in the calculation the propagation of the fields to different depth levels according to the diffraction theory [2].

- **Weighted Gerchberg-Saxton (WGS)**
  This is a modified version of GS where all the features in the CGH have a better uniformity. For this purpose an extra degree of freedom is introduced in the CGH calculation which is the intensity weight of every feature in the pattern. At each iteration the intensity of each feature is optimized comparing the intensity at the last iteration and the intensity of the target. The computational cost remains the same of GS.

Recent algorithms

- **Compressive sensing Gerchberg-Saxton (CS-GS)**
  This algorithm is a faster version of the GS for sparse diffraction limited spots in 3D. The field at the SLM is defined as reported in equation 4.1 and it is iteratively calculated for a subset of cM (where c is the compression factor

and M is the number of SLM pixels) randomly distributed pixels of the SLM with GS algorithm. The last iteration is a standard GS calculation over all the M pixels in the SLM. The computational cost scales as $N_i \times N_p \times cM + N_p \times M$, this cost for $cN_i << 1$ can be approximated to $M \times N_p$, where N_i is the number of iterations, N_p is the number of points, M is the number of SLM pixels. It has been demonstrated [4] that a speedup over one order of magnitude can be achieved without compromising the quality of the obtained hologram compared to regular multi-spot-GS.

- **Compressive sensing weighted Gerchberg-Saxton (CS-WGS)**
  This algorithm is a faster version of the WGS for sparse diffraction limited spots in 3D. WGS is incompatible with the compressive sensing approach leading quickly to divergence but it is possible to run Compressive sensing Gerchberg-Saxton (CS-GS) for k-1 iterations and then perform a final iteration with WGS. This method, known as CS-WGS has an approximately double computational cost compared to CS-GS when $c \times N_i << 1$. As reported in [5]both CS-WGS and CS-GS can be implemented with GPU calculations on a low cost graphic card. This upgrade permits to calculate a CGH ten times faster compared to the standard version using the FFT algorithm.

- **Non-Convex Optimization for Volumetric CGH (CGH-NOVO)**
  This iterative algorithm to produce phase masks based on the non convex minimization of a custom-defined cost function [3]. Given the intensity distribution of the target pattern V at different depths z, the corresponding hologram is calculated via the RS algorithm. A cost function is defined as,

$$L(I((\phi_s), V)) \tag{2.6}$$

  where $I(\phi_s)$ is the distribution generated by the random phase mask ϕ_s at each plane and V is the intensity of the desired pattern at the focal plane. The minimization of the cost function in eq. 2.6 gives the optimal phase ϕ^*. When $I(\phi)$ and the cost function have a well-defined derivative the problem is solved with a gradient descendant approach.

  CGH-NOVO offers the advantage of choosing a cost function tailored for the specific application. For instance, one might be interested in stimulating a subset of neurons while minimizing the intensity received by off-target neurons below some illumination threshold, cost functions optimized for binary patterns are suitable. Another example of the flexibility of the CGH-NOVO is the possibility to implement a cost function optimized for 2P illumination. This algorithm can be implemented using a GPU to speed up the calculations.

- **DeepCGH**
  The DeepCGH algorithm [6] uses convolutional neural networks (CNNs) with

unsupervised learning to compute 3D holograms with the image-based approach. The distribution of amplitudes $A(x, y, z)$ of the 3D target pattern at the focal planes is the input of the CNN. The CNN provides in output an estimate of the complex field $P(x, y, z = 0)$ at depth $z = 0$. This field back-propagated to the SLM plane via 2D inverse Fourier transform gives the phase map Φ of the CGH. During unsupervised training of the CNN, the goal is to minimize a loss function $L(A, \widetilde{A})$ where A is the intensity distribution of the target and $\widetilde{A}$ is the intensity associated with the predicted SLM phase. As shown in [6] this algorithm offers a 10 time faster computational cost and up to 41 % increased accuracy compared to iterative methods such as CGH-NOVO and GS. Moreover, experimentally, DeepCGH holograms can elicit two-photon absorption with 50 % higher efficiency compared to GS or CGH-NOVO algorithms, given the same experimental conditions [6]. However, this algorithm requires a high-performance graphic card for GPU calculations.

2.A.3. Algorithm for PSF extraction

The algorithm takes in input the z stack of the beads sample and some user defined parameters about the characteristics of the setup and the sample such as : pixel size, z step used in the data acquisition, expected size of the PSF, size of the images to segment single beads and the minimum mass fraction which is used as a threshold value to detect automatically the beads. The beads detection is performed on the maximum projection of the z stack and all the features with a mass exceeding the minimum mass parameter are discarded. Here, the mass is calculated as the sum of the signal from each feature considered as a potential bead across the full z stack. After this first detection the resulting beads are isolated and cropped in single images, if two or more beads are not separated in the three dimension they will be discarded. Then, each bead is fitted with a 2D Gaussian in the xy view while a 1D Gaussian fit is performed through the focal plane of the PSF to quantify the PSF along the z axis. At this point the obtained PSFs are compared all together to calculate the Pearson correlation coefficient $\mu_{PCC} \pm 3 \cdot \sigma_{PCC}$, this calculation allows to find and discard the outlier PSFs. Finally an upsampling of the Gaussian fits is performed to have more data points to calculate the PSFs. The results from all the beads are averaged to obtain the averaged original and upsampled PSF.

References

[1] P. Shirley, M. Ashikhmin, and S. Marschner, *Fundamentals of Computer Graphics*. 2009.

[2] J.W. Goodman, *Introduction to Fourier optics*. 2005.

[3] J. Zhang, N. Pégard, J. Zhong, H. Adesnik, and L. Waller., "3D computer-generated holography by non-convex optimization," *Optica*, vol. 4, no. 10, pp. 1306–1313, 2017.

[4] P. Pozzi, L. Maddalena, N. Ceffa, O. Soloviev, G. Vdovin, E. Carroll, and M. Verhaegen, "Fast Calculation of Computer Generated Holograms for 3D Photostim-

ulation through Compressive-Sensing Gerchberg–Saxton Algorithm," *Methods and Protocols*, vol. 2, no. 1, pp. 2–15, 2018.

[5] P. Pozzi and J. Mapelli, "Real Time Generation of Three Dimensional Patterns for Multiphoton Stimulation," *Frontiers in Cellular Neuroscience*, vol. 15, no. 34, 2021.

[6] M. Hossein Eybposh, N. W. Caira, M. Atisa, P. Chakravarthula, and N. C. Pégard, "DeepCGH: 3D computer-generated holography using deep learning," *Optics Express*, vol. 28, no. 18, p. 26636, 2020.

3

Fast Calculation of Computer Generated Holograms

The calculation of computer generated holograms for optogenetic stimulation of brain circuits is most commonly performed with either the high-speed, low-performance random superposition algorithm, or the low-speed, high performance Gerchberg-Saxton algorithm. This chapter presents a variation of the Gerchberg-Saxton algorithm that, by only performing iterations on a subset of the data, according to compressive sensing principles, is rendered significantly faster while maintaining high quality outputs. The algorithm is presented in high-efficiency and high-uniformity variants. The method was tested computationally against existing algorithms, and the results were confirmed experimentally on a custom setup for in vivo multiphoton optogenetics. The results clearly show that the proposed method can achieve computational speed performances close to the random superposition algorithm, while retaining the high performance of the Gerchberg-Saxton algorithm, with a minimal loss of hologram quality.

This chapter is based on the work: *Fast Calculation of computed generated holograms for 3D Photostimulation through Compressive-Sensing Gerchberg–Saxton Algorithm.* Methods and Protocols **2**(1), 2-15, (2019)

3.1. Introduction

The calculation of computer generated holograms (CGHs) is a non-trivial problem and several algorithms are available. In particular, two main classes of algorithms are available: fast Fourier transform based algorithms and multi-spot algorithms.While fast Fourier transform algorithms can generate extremely complex illumination patterns in very short times, a strict requirement is that illumination light should be focused either on a two-dimensional plane [1], or at most on a limited number of of two-dimensional planes at different depths [2].On the other hand, multi-spot algorithms tend to be slower, but can generate holograms of diffraction limited spots arbitrarily distributed in the three-dimensional (3D) field of view of the optical system. These spots can be used to stimulate sub-cellullar regions in the neuron of interest [3]. Alternatively, to use a multi-spot hologram to illuminate regions of interest (ROIs) of the size of neurons, the entire illumination pattern can be scanned in a spiral or raster pattern [4], or combined with temporal focusing excitation [5]. Several algorithms exist to calculate a multi-spot hologram, generally representing a trade-off between computation speed and quality of the hologram. A good summary of the most common algorithms for the generation of multi-spot holograms can be found in [6].

The most common way to compute a multi-spot CGH is the Gerchberg-Saxton (GS) algorithm [7], an iterative procedure of alternating projections allowing for the computation of high quality CGHs in time frames compatible with experimental needs. While the computational cost scales linearly with the amount of generated spots, in a general experimental scenario, calculation of a CGH can take between a few seconds and a couple of minutes.
In optogenetics experiments requiring frequent calculation of new stimulation patterns "on-the-fly", the random superposition (RS) algorithm is sometimes preferred to GS algorithm [8], sacrificing hologram quality to achieve higher computation speeds.

In this paper, a modified version of the GS algorithm, based on compressive sensing of the pupil function, is presented. The compressive sensing Gerchberg–Saxton algorithm (CS-GS) can generate holograms of equal quality to the standard GS algorithm, but reduces the computational cost by more than one order of magnitude, reaching time scales similar to the RS algorithm.

3.2. Method Description

3.2.1. Random Superposition and Gerchberg–Saxton Algorithm

The CGH $\phi(x', y')$ generating a single spot at coordinates (x, y, z) at the sample can be easily computed through Fourier optics, as a combination of tip, tilt and defocus aberrations

$$\phi(x', y') = \frac{\pi z}{\lambda f^2}(x'^2 + y'^2) + \frac{2\pi}{\lambda f}(xx' + yy'), \tag{3.1}$$

where f is the equivalent focal length of the optical system and λ is the wavelength.

In the GS algorithm, the CGH generating a set of N spots at coordinates (x_n, y_n, z_n) is assumed to be the phase of the superposition of all the fields generating the individual spots

$$\phi_{\text{cgh}}(x', y') = \arg \sum_{n=1}^{N} \frac{1}{N} \mathrm{e}^{-\mathrm{i}(\phi_n(x', y') + \theta_n)}, \tag{3.2}$$

where θ_n are some constant phase terms. The only degrees of freedom that can be addressed from the algorithm to optimize the quality of the CGH are the N values of θ_n.

It is to be noticed that, by simply solving Equation (3.2) for random values of θ_n, a low quality CGH can be calculated, without any optimization on the constant phase terms θ_n. This is known as the RS algorithm, which has computational cost scaling as $M \times N$ where M is the number of spatial light modulator (SLM) pixels.

To compute optimal values of θ_n, the GS algorithm proceeds by alternating projections. The initial values of the phases θ_n^0 are chosen at random, and the initial CGH ϕ_{cgh}^0 is computed according to Equation (3.2).

At each kth iteration, the values of θ_n^k are estimated as

$$\theta_n^k = \arg \int_{SLM} \mathrm{e}^{-\mathrm{i}(\phi_{\text{cgh}}^{k-1} - \phi_n)} dx' dy', \tag{3.3}$$

and ϕ_{cgh}^k is computed again according to Equation (3.2).

Performing a GS algorithm for K iterations, while generating N spots, on an SLM with M pixels has a computational cost scaling as $K \times N \times M$. Empirically, a few tens of iterations are required for convergence of the algorithm.

3.2.2. Compressive Sensing Approach

To understand the principle of the CS-GS algorithm described in this paper, it must be noticed that Equation (3.2) can be rewritten as

$$\vec{y} = A\vec{x}^T, \tag{3.4}$$

where $\vec{y}$ is a N-dimensional vector representing the field values for each spot, A is a $N \times M$-dimensional matrix in which each nth line contains the value of $\frac{1}{N}\mathrm{e}^{-\mathrm{i}\phi_n}$ at each mth pixel of the SLM, and $\vec{x}$ is a vector of coefficients in the form $x_m = \mathrm{e}^{-\mathrm{i}\phi_{\text{cgh},m}}$ where $\phi_{\text{cgh},m}$ is the value of the phase of the CGH at the mth pixel of the SLM.

Since generally $M \gg N$, this is an under-determined linear system. While an exact solution to the system is provided by Equation (3.2), according to the principles of compressive sensing [9], and in particular equivalently to k-space compressed imaging applications [10], a satisfying solution can be obtained by only sampling a subset of cM randomly distributed pixels of the SLM, where $\frac{N}{M} < c < 1$.

According to this assumption, the first $K-1$ iterations of the GS algorithm can be performed only considering a subset of randomly distributed pixels of the SLM, and

only on the Kth iteration the whole CGH should be computed according to Equation (3.2). With this algorithm, the computational cost scales as $K \times N \times cM + N \times M$, which, for $c \times K \ll 1$, can be approximated as just $N \times M$, which is equivalent to the RS algorithm cost. Reasonable values of K are in the order of 10^2.

3.2.3. Weighted Gerchberg–Saxton

The GS algorithm tends to optimize the efficiency of the CGH, but does not guarantee uniform intensity amongst the foci created. In applications in which it is crucial for the CGH to generate spots of equal intensity, a modified version of the GS algorithm, named weighted Gerchberg–Saxton (WGS) algorithm [6] can be implemented to improve uniformity, with a minor loss in efficiency. The WGS algorithm has the same computational cost of GS. In the WGS algorithm, N additional degrees of freedom are introduced, as intensity weights ω_n in the combination of the spots wavefronts. The initial value of the weights is equal for all spots, and set to $\omega_n^0 = \frac{1}{N}$. Equation (3.2) is then rewritten as:

$$\phi_{\text{cgh}}^k(x', y') = \arg \sum_{n=1}^{N} \omega_n^k \mathrm{e}^{-\mathrm{i}(\phi_n + \theta_n)}. \tag{3.5}$$

Computing the intensity of each spot as:

$$I_n^k = \left| \int_{SLM} \mathrm{e}^{-\mathrm{i}(\phi_{\text{cgh}}^{k-1} - \phi_n)} dx' dy' \right| \tag{3.6}$$

at each step, the weights are recalculated as:

$$\omega_n^k = \omega_n^{k-1} \frac{\langle I_n^k \rangle}{I_n^k}. \tag{3.7}$$

This approach cannot be implemented in a compressive sensing framework, as it quickly diverges for even slightly inaccurate calculations of I_n. However, significant improvements can be obtained by running the CS-GS algorithm for K-1 iterations, and only performing a single iteration of the WGS at the end when computing the final CGH. This, however, doubles the computation time compared to CS-GS when $c \times K \ll 1$. For the rest of the paper, this approach is referred to as compressive sensing weighted Gerchberg–Saxton algorithm (CS-WGS).

3.3. Materials and Methods

3.3.1. Software Implementation

All algorithms described in Section 3.2 were implemented in Python 2.7 (Python Software Foundation, `https://www.python.org/`). All code is available as Supplementary Materials to this article, and in a public repository [11]. While better performances could be achieved implementing the algorithm in a lower level programming language, or through implementation over dedicated hardware (e.g.,

multi-core threads and GPU implementations), the Python scripting code was chosen to maximize the readability of the code, and provide an easy way to reproduce the results presented. Computational results reported in Section 3.4.1 were achieved with a mid-range desktop computer (Intel Core i5-4690 3.5 Ghz, 8 GB of memory, 64-bit Windows 7 operating system).

3.3.2. Experimental Setup

For the experimental investigation of the algorithms performances, we employed the system shown in Fig. 3.1. Two-photon excitation (TPE) beam (λ = 800 nm, diameter = 0.8 mm) from a Ti:Sapphire laser passes a beam expander composed by two lenses to uniformly illuminate the active area of a reflective SLM. The SLM is conjugated with the objective back aperture via lenses L1 and L2. An inverse pinhole blocks the zero-order beam while the CGH is projected onto the sample (Rhodamine 6 G uniformly coated slide, thickness 1.7 mm, Thorlabs; Newton, New Jersey, United States). Two-photon excitation fluorescence is collected by the same objective and, thanks to a short-pass dichroic mirror and a tube lens, is recorded by a complementary metal oxide semiconductor (CMOS) camera. To acquire images of 3D holograms, a deformable mirror (DM-40, Thorlabs; Newton, New Jersey, United States) was added to the detection path, conjugated with the objective back aperture.

3.4. Results

3.4.1. Computational Results

The CS-GS algorithm was tested against the regular GS algorithm, as an upper limit of performance, and the random superposition algorithm, as an expected lower limit of performance. The performance metric used to evaluate the quality of the CGHs were, as in [6], the efficiency and uniformity of the obtained patterns. The efficiency e of the CGH is computed as the fraction of the total intensity directed at the generated spots. The uniformity u is calculated as

$$u = 1 - \frac{I_{max} - I_{min}}{I_{max} + I_{min}}, \tag{3.8}$$

where I_{max} and I_{min} are the intensities of the brightest and dimmest spot generated by the CGH.

As a computational test, CGHs were calculated for a random 3D distribution of 100 spots, simulating a reasonable requirement for a optogenetics experiment, and for a grid of 10×10 spots in the image plane, representing a worst-case scenario for the uniformity of the pattern, where WGS should perform much better than GS. All variants of the GS algorithm were run for 50 iterations.

Due to the randomized initialization of the values of θ_n, the final values of u and e of the CGH can vary slightly for different initializations. All the reported measurements were therefore performed by computing each CGH 10 times, with different random initializations, and calculating the mean and standard deviation of u and e.

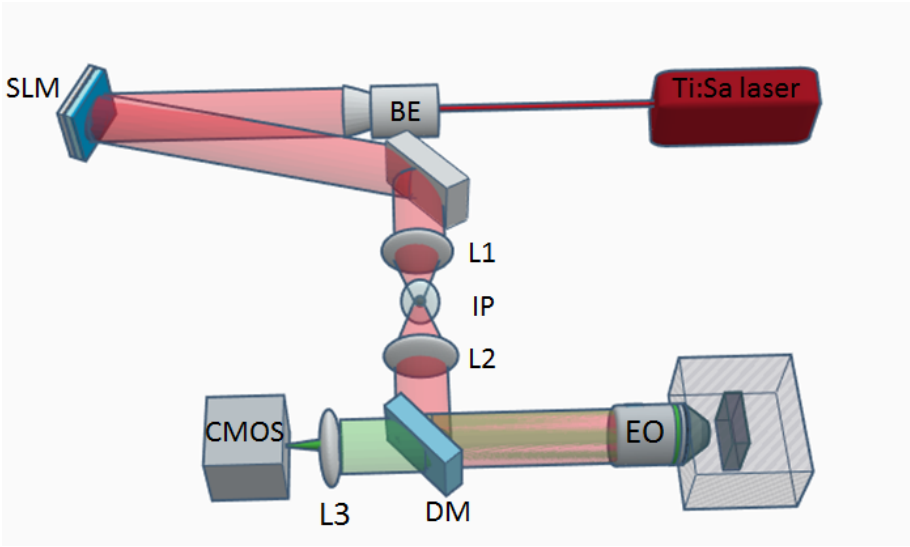

Figure 3.1: **Scheme (not to scale) of two-photon excitation computer-generated hologram (CGH) setup**. Ti:Sapphire laser (MIRA 900-F, Coherent; Santa Clara, California, United States), beam expander (BE) composed by two lenses ($f = 25$ mm and $f = 150$ mm, respectively), reflective spatial light modulator (SLM, 1920 $\times$ 1152; pixel pitch, 9.2 μm Meadowlark Optics; Frederick, Colorado, United States), lens L1 ($f = 250$ mm) and L2 ($f = 500$ mm), inverse pinhole (IP), objective (EO, Olympus 20X, 1.0 NA, water immersion, Olympus; Tokyo, Japan), dichroic mirror (DM) with cutoff wavelength at 700 nm (FF01-7200/SDi01, Semrock; Rochester, New York, United States), tube lens L3 ($f = 200$ mm), CMOS camera (IDS UI-3270CP, IDS; Obersulm, Germany).

The results, reported in Fig. 3.2 and 3.3, show how the CS-GS algorithm has performances virtually identical to GS with compression factors up to $c = 1/32$, while providing an improvement in computational time of more than one order of magnitude. Moreover, CS-GS still greatly outperforms RS up to extreme compression factors.

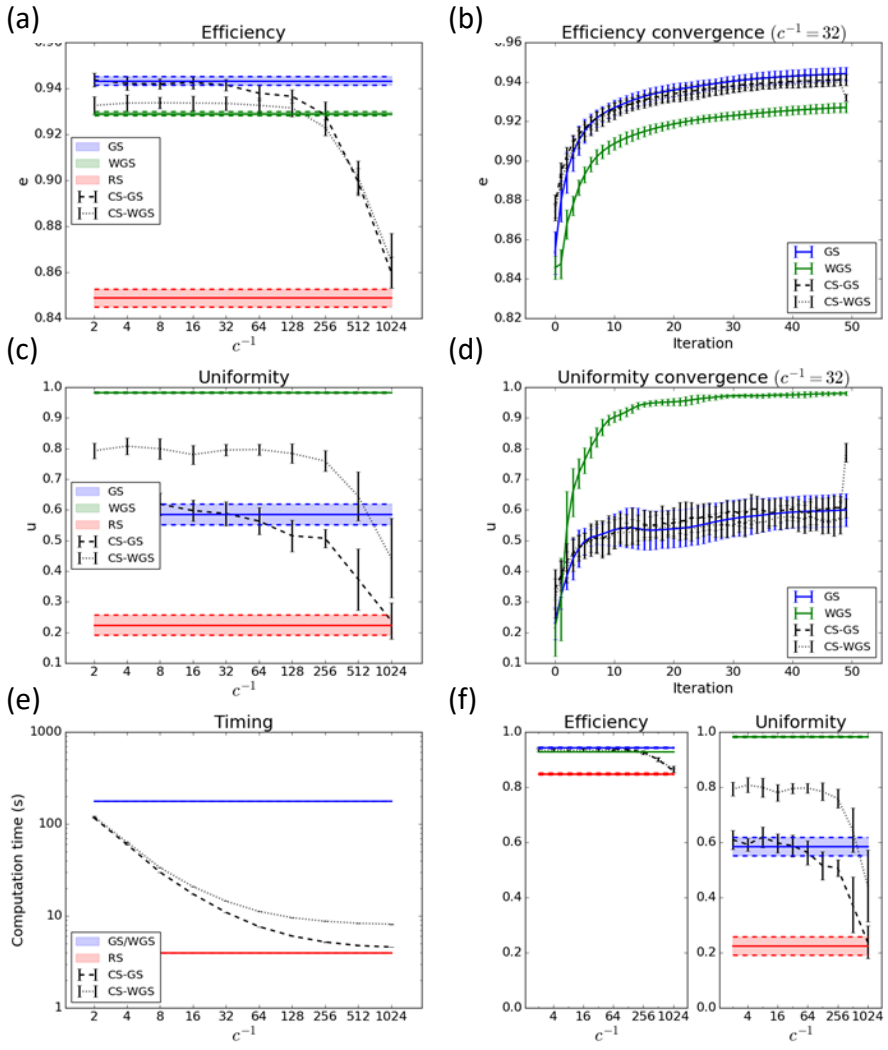

Figure 3.2: **Algorithms performance in the case of the generation of a regular 2D array of 100 spot.** Graphs (a) and (b) report the efficiency metric as a function of the subsampling parameter $1/c$ and the convergence graph at $c = 1/32$ for the CS-GS and the CS-WGS algorithm. Graphs (c) and (d) report uniformity metric and convergence for the same dataset. For comparison, horizontal bars represent the interval of confidence of performance of GS, WGS, and RS algorithm. Graph (e) reports the improvement in computation time as a function of $1/c$. Graph F reports the efficiency and uniformity represented in absolute scale to better represent overall performance.

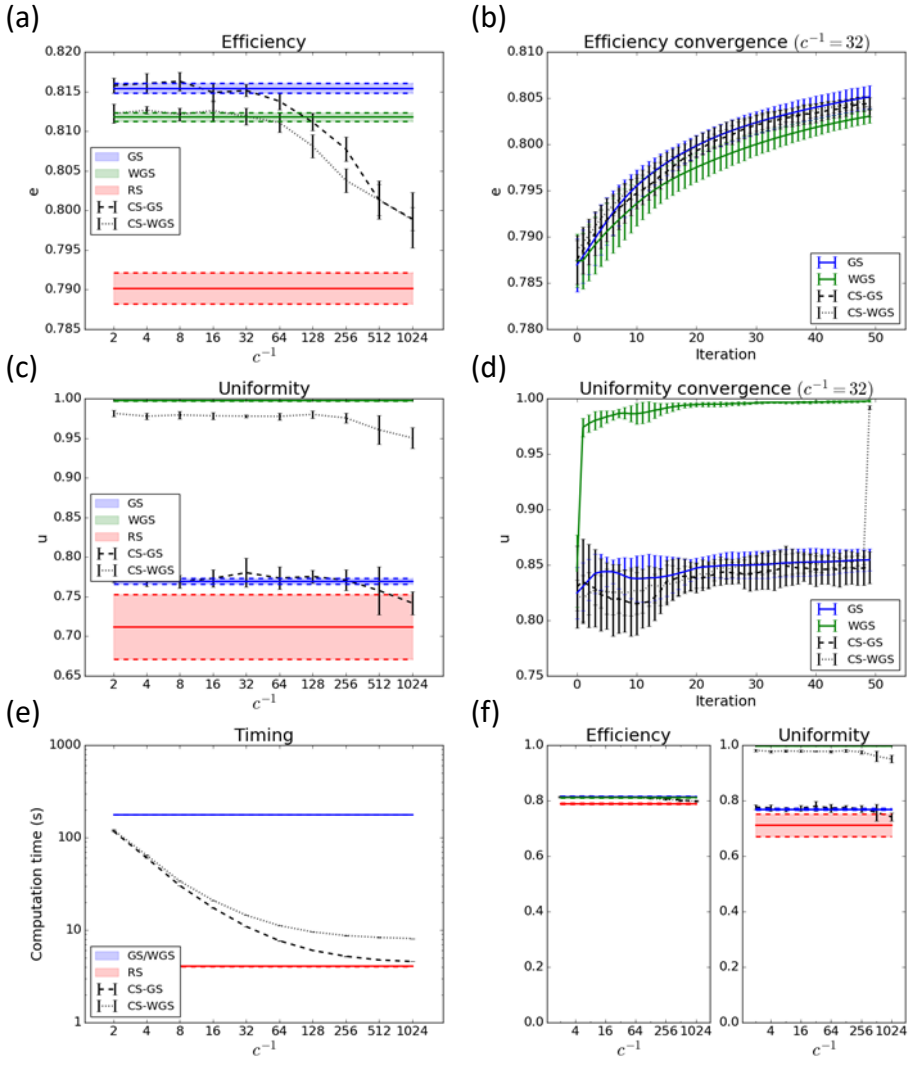

Figure 3.3: **Algorithms performance in the case of the generation of a random 3D distribution of 100 spots.** Graphs (a) and (b) report the efficiency metric as a function of the subsampling parameter $1/c$ and the convergence graph at $c = 1/32$ for the CS-GS and the CS-WGS algorithm. Graphs (c) and (d) report uniformity metric and convergence for the same dataset. For comparison, horizontal bars represent the interval of confidence of performance of GS, WGS, and RS algorithm. Graph (e) reports the improvement in computation time as a function of $1/c$. Graph F reports the efficiency and uniformity represented in absolute scale to better represent overall performance.

As far as the weighted version is concerned, CS-WGS, only performing a single weighted iteration, does not perform as well as the regular version of WGS, especially in the case of the generation of regular geometrical patterns of spots. However, it still greatly outperforms GS in uniformity, and its deficit in uniformity compared to WGS can be considered practically negligible in the case of randomly distributed patterns of spots.

To rule out the possibility that the computation time difference between the standard and compressed sensing versions of the algorithms could be partially compensated by different convergence rates, efficiency and uniformity were estimated as a function of the iteration number. Since, for the considered experimental parameters, a compression factor of $c = 1/32$ appears to represent the best compromise between speed and performances for both CS-GS and CS-WGS, such a compression parameter was used for the convergence speed comparison. As shown in Fig. 3.2 and 3.3, no significant difference in convergence speed can be observed. It is apparent from the convergence graphs that CS-GS and CS-WGS only differ from each other in the last iteration, as described in Section 3.2.3. This causes the sudden discontinuity in the CS-WGS convergence graph.

3.4.2. Experimental Results

To experimentally compare our methods to RS and iterative projections algorithms, we used each of them to compute the same 2D multi-spot CGH. This pattern contains 25 points arranged in letters shape for the initials of the laboratory institution (Technische Universiteit Delft, TUD) and extending over the complete available field of view. While all iteratively generated CGH were obtained with 100 iterations, we also operated WGS with 200 iterations and considered it as reference term in the performances evaluation. All the compressive sensing methods were computed with a sub-sampling value of 0.05.

As qualitatively shown in Fig. 3.4 (a)–(d) CS-WGS and WGS outperform RS. The intensity profile from a line of points in each image (Fig. 3.4 (e)) highlights the lack of excitation for some ROIs in the RS image (the peak corresponding to the third point is almost absent), while all other methods provide comparable results in terms of points intensity.

To quantitatively classify the performances of all algorithms including GS and CS-GS, we estimated the relative brightness and the intensity uniformity across the FOV of the different patterns. For each method, a stack of five images was acquired, and then, on the averaged image, seven random points were selected and fitted with 2D Gaussian profiles. The peak values from the fit are averaged and normalized for each method to produce the relative brightness. The brightness analysis (Fig. 3.4(f)) confirmed RS as the least efficient method, while all others show results comparable with the reference WGS.

From the standard deviation of the peaks values (Fig. 3.4(g)), we quantified the uniformity of the illumination. As anticipated in the computational results, WGS and CS-WGS algorithms are reaching uniformities that are very close to the golden standard (around 90%) at a fraction of the computational cost. Furthermore, we obtained a slightly higher uniformity for CS-WGS compared to WGS (run with the same number of iterations) corroborating that the deficit in uniformity found in the computational results is practically negligible for randomly distributed patterns.

Additionally, a separate dataset with spots distributed in three dimensions is reported in Fig. 3.5, to prove the performances of the method in three dimensions. As can be observed, the WGS and CS-WGS images are practically indistinguishable, while RS, despite its minimal time saving compared to CS-WGS, has visibly worse performance, with significantly non uniform spots in the distribution.

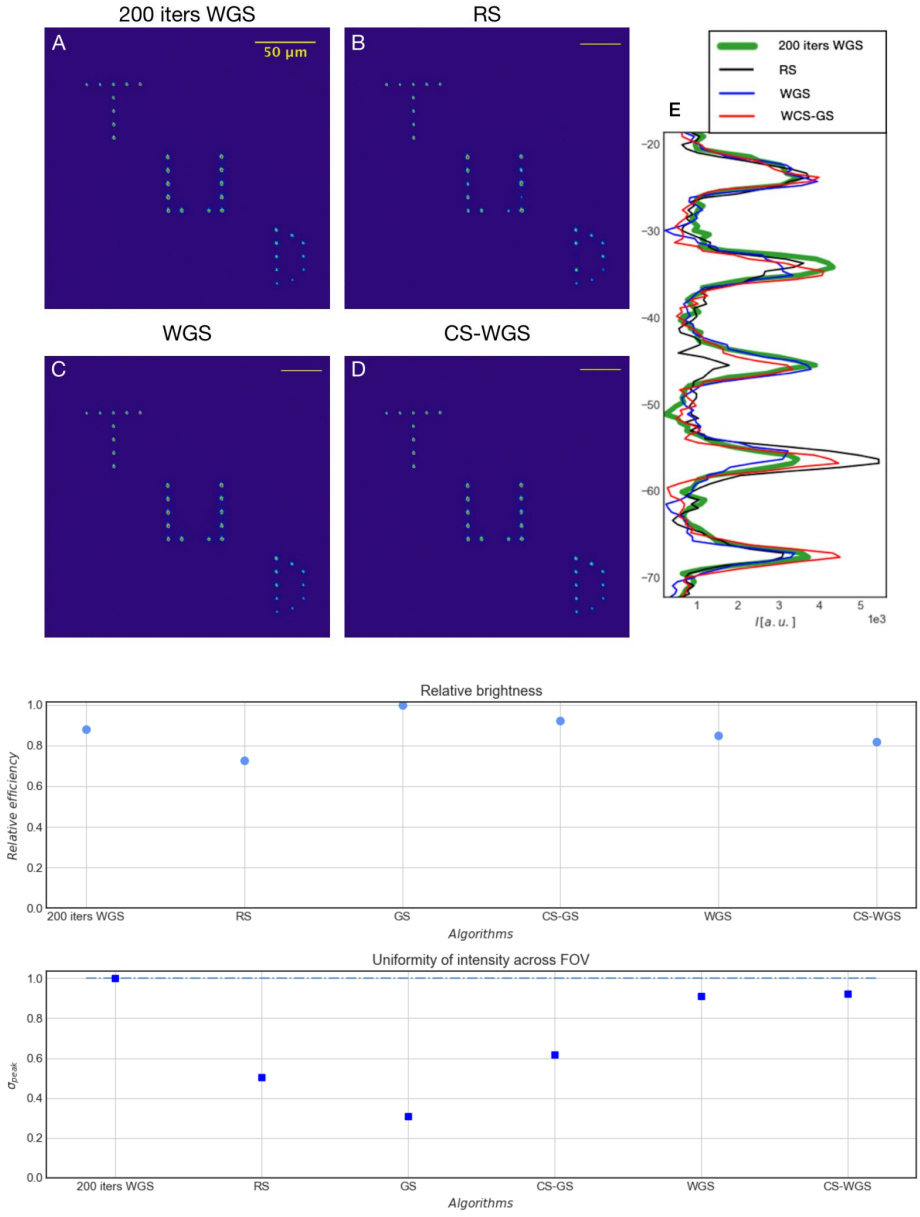

Figure 3.4: **Experimental results.** (a)–(d) Two photon excitation fluorescence images of multi-spot CGHs generated, respectively, with WGS 200 iterations, RS, WGS and CS-WGS algorithms. (e) Intensity profile from a single line in panel (d). (f) Relative brightness for all methods explored. (g) Uniformity across the field of view in the peak intensities for all methods explored.

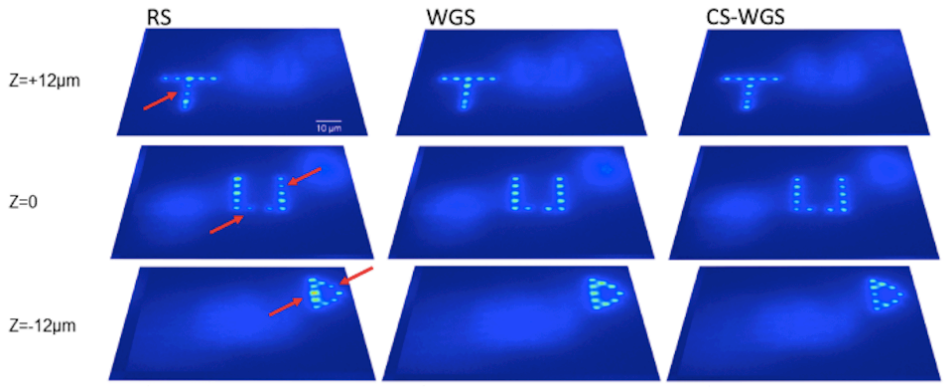

Figure 3.5: **Experimental results for a 3D hologram**. CS-WGS and WGS were computed over 100 iterations, while CS-WGS had a compression factor of 0.05. Computation times were, respectively, 5 s, 40 s and 456 s for RS, WGS and CS-WGS. All images are reported on the same intensity scale. It can be noticed that, while the WGS and CS-WGS images are practically identical, RS has some spots with significantly different intensities (highlighted by the red arrows)

3.5. Discussion

In this paper, we demonstrate, both computationally and experimentally, how the implementation of compressive sensing principles to the Gerchberg–Saxton algorithm for the generation of multi-spot holograms, in both its classic and weighted forms, can provide a dramatic decrease in computation time, without significantly affecting its performance. This method could therefore represent a standard in spatial light modulation based optogenetic stimulation, where fast and reliable generation of 3D multi-spot patterns is key for a successful experiment. To facilitate implementation and testing for the neuroscience community, Python implementations of the RS, GS, WGS, CS-GS and CS-WGS algorithms are available as Supplementary Materials to this paper and in a public repository [11].

References

[1] C. Lutz, T. S. Otis, V. DeSars, S. Charpak, D. A. DiGregorio, and V. Emiliani, "Holographic photolysis of caged neurotransmitters," *Nature Methods*, vol. 5, no. 9, pp. 821–827, 2008.

[2] J. Zhang, N. Pégard, J. Zhong, H. Adesnik, and L. Waller., "3D computer-generated holography by non-convex optimization," *Optica*, vol. 4, no. 10, pp. 1306–1313, 2017.

[3] F. Anselmi, C. Ventalon, A. Bègue, D. Ogden, and V. Emiliani, "Three-dimensional imaging and photostimulation by remote-focusing and holographic light patterning," *PNAS*, vol. 108, pp. 19504–19509, 2011.

[4] A. M. Packer, L. E. Russell, H. W. Dalgleish, and M. Häusser, "Simultaneous all-optical manipulation and recording of neural circuit activity with cellular resolution in vivo," *Nature Methods*, vol. 12, no. 2, pp. 140–146, 2015.

[5] N. C. Pégard, A. R. Mardinly, I. A. Oldenburg, S. Sridharan, L. Waller, and H. Adesnik, "Three-dimensional scanless holographic optogenetics with temporal focusing (3D-SHOT)," *Nature Communications*, vol. 8, no. 1, 2017.

[6] R. Di Leonardo, F. Ianni, and G. Ruocco, "Computer generation of optimal holograms for optical trap arrays," *Optics Express*, vol. 15, no. 4, pp. 169–175, 2007.

[7] R. W. Gerchberg and W. O. Saxton, "A Practical Algorithm for the Determination of Phase from Image and Diffraction Plane Pictures," *Optik*, vol. 35, no. 2, pp. 337–246, 1972.

[8] L. Golan, I. Reutsky, N. Farah, and S. Shoham, "Design and characteristics of holographic neural photo-stimulation systems," *Journal of Neural Engineering*, vol. 6, no. 066004, 2009.

[9] E. J. Candès, J. Romberg, and T. Tao, "Robust uncertainty principles: Exact signal reconstruction from highly incomplete frequency information," *IEEE Transactions on Information Theory*, vol. 52, no. 2, pp. 489–509, 2006.

[10] D. Lustig, M.; Donoho, J. Santos, and J. Pauly, "Compressed sensing MRI," *IEEE Signal Process. Mag.*, vol. 25, pp. 72–82, 2008.

[11] "https://github.com/csi-dcsc/compressive-sensing-Gerchberg-Saxton."

4

Local aberration control to improve efficiency in multiphoton holographic projections

Optical aberrations affect the quality of light propagating through a turbid medium, where refractive index is spatially inhomogeneous. In multiphoton optical applications, such as two-photon excitation fluorescence imaging and optogenetics, aberrations non-linearly impair the efficiency of excitation. We demonstrate a sensorless adaptive optics technique to compensate aberrations in holograms projected into turbid media. We use a spatial light modulator to project custom three dimensional holographic patterns and to correct for local (anisoplanatic) distortions. The method is tested on both synthetic and biological samples to counteract aberrations arising respectively from misalignment of the optical system and from samples inhomogeneities. In both cases the anisoplanatic correction improves the intensity of the stimulation pattern at least two-fold.

This chapter is based on the work: *Local aberration control to improve efficiency in multiphoton holographic projections.* Optics Express **30**(16), 29128-29147, (2022)

4.1. Introduction

Computer generated holography (CGH) is a well-established technique to shape coherent light into custom three-dimensional (3D) patterns. When encoded onto a programmable spatial light modulator (SLM), CGH enables flexible projection technology. A wide range of applications exploits this strategy, such as dynamically controlled optical traps for micromanipulation [1], laser microsurgery [2], two-photon polymerization to produce micrometer-sized 3D structures [3], and optogenetic stimulation of neurons in tissue [4]. Each of these applications relies on the quality of the projected light field, in terms of intensity, precision and fidelity to the computed version of the CGH. However, distortion of the modulated wavefront at any point in the optical path can compromise the reconstructed hologram.

Aberrations arise in any non-ideal imaging system from misalignment and from propagation through materials where the index of refraction varies spatially across the wavefront. In some cases, aberrations affect the whole field of view (FOV) homogeneously. Those aberrations are denominated isoplanatic and they can be modeled and compensated for in the design of the instrument with a fixed optic. For instance, in photo-resist laser writing, aberrations originating from the interface between the resist and the substrate are proportional to the mismatch of refractive index at this interface, the depth of the focal point, and the numerical aperture (NA) of the objective lens [5]. More generally, aberrations varying across the FOV are called anisoplanatic. Sample-induced aberrations are a known problem for loss of signal and contrast in deep tissue optical imaging, where both excitation and emission light are distorted when they propagate through inhomogeneous and thick biological samples [6]. In multiphoton excitation, aberrations reduce peak excitation intensity nonlinearly, leading both to inefficient excitation as well as losses on the signal collection.

Adaptive optics (AO), a technique borrowed from astronomers who obtained high quality images of stars and satellites deteriorated by atmospheric turbulence [7], can compensate for such distortions. An AO system may consist of three main components: a sensor to measure the aberrations, an adaptive optical element to correct the wavefront distortions, and a controller to feed the information obtained by the sensor to the adaptive element. An alternative to using a wavefront sensor in closed loop is a sensorless approach in which information about the wavefront can be determined indirectly (e.g., from the properties of two-photon excited fluorescence). Both sensor-based and sensor-less AO approaches have been successfully integrated into different microscope designs [8]. In widefield microscopy, a Shack-Hartmann wavefront sensor may be used to measure the distortion on the fluorescent signal using guide stars, or fluorescent landmarks with known shape [9]. Differently, wavefront sensors have been employed in light sheet microscopy to correct the aberrations on the excitation light [10]. The approach most commonly used in laser scanning microscopies, like laser scanning confocal microscopy, is to obtain a single isoplanatic aberration correction for both the excitation light and fluorescence signal over a relatively small FOV [11]. At the same time, sensorless AO has been widely applied to correct excitation and or emission light in different microscopy techniques [12–14]. Recently, various research groups proposed aniso-

planatic corrections to improve imaging in more heterogeneous samples, such as intact organs [15–18].

In non-imaging applications, holographic projections are likewise subject to aberrations. Stray photons may have unintended consequences in the case of laser writing or optogenetics. In particular, in the case of optogenetics, chromophores are intentionally designed to perturb the biology of the system rather than simply fluoresce. In fact, photostimulation conditions in optogenetics are often more intense than conditions used in imaging, using longer dwell times (millisecond vs. microsecond), so the effect of off-target photostimulation can be more problematic. Inefficient excitation is also detrimental for photostimulation in living tissues where one wants to use the minimum light needed to be effective.

Here we apply a sensorless AO approach to correct aberrations on holographic projections using two-photon excited fluorescence (TPEF) as a readout. An optical module for photostimulation with CGH is implemented, which we will call 2P-CGH in this paper. A computer generated hologram (CGH) of the desired 3D excitation pattern is calculated and its phase is imposed on a coherent wavefront at the rear pupil plane of an objective through a liquid crystal on silicon spatial light modulator (LCoS-SLM). The SLM serves also as AO element to introduce bias aberration into the stimulation light. The optimal AO corrections are determined through a simple hill-climbing approach where a series of images is acquired under different bias aberrations. To validate the method we demonstrate correction of anisoplanatic aberrations in 2D and 3D using a series of samples with increasing complexity, including tissue. We show that our method can improve the intensity of the stimulation pattern in both synthetic samples and fixed tissue by at least a factor of two.

4.1.1. Computer generated hologram calculation

The optical layout to project computer generated holograms is based on Fourier holography, as shown in Fig.4.1(a). The target field $U_o(z_i)$ is defined by user-selected points in a virtual representation of the real space FOV, describing the 3D pattern of points at depths z_i. The hologram field U_h is related to the field at the focal planes through a discrete Fourier transform. The phase of the hologram field is then addressed to the SLM and the hologram is reconstructed optically by a spatial Fourier transformation by the objective lens. Holograms are calculated with the Compressive Sensing Weighted Gerchberg-Saxton (CS-WGS) algorithm [19]. This algorithm can generate holograms of point clouds arbitrarily distributed in the 3D FOV of the optical system. As reported in [19], CS-WGS provides comparable results in terms of spot brightness and uniformity as Gerchberg-Saxton and Weighted Gerchberg-Saxton approaches, while reducing drastically the computational time.

For a CGH with N spots, the field at the SLM is calculated as the superposition of the fields generating each individual spot:

$$U_h = \sum_{n=1}^{N} u_{o,n} \cdot e^{-i(\phi_{POS,n}+\phi_n)} \tag{4.1}$$

where $u_{o,n}$ is the amplitude of the field associated with the n^{th} spot at the focal plane, ϕ_n is a constant term and $\phi_{POS,n}$ is a phase describing the position. The position $\phi_{POS,n}$ is determined by combination of tip, tilt and defocus localizing each of the N points in 3D space:

$$\phi_{POS,n}(x,y) = \frac{2\pi}{\lambda f} \cdot (x_n \cdot x' + y_n \cdot y') + \frac{z_n \pi}{\lambda^2 f^2} \cdot (x'^2 + y'^2) \tag{4.2}$$

where x_n, y_n, z_n are the coordinates of each point, x', y' are the SLM coordinates, f is the focal length of the optical system and λ is the wavelength of the light source. Any iterative calculation of the hologram field aims at maximizing the quality of the hologram by optimizing the value of the phase term ϕ_n.

The approach here described allows to include in the hologram field (Eq. 4.1) a phase term, $\phi_{AO,n}$, representing the full-pupil phase applied to the sub-hologram for each point n to compensate local optical aberration [15]. Hence, the CGH phase encoding for a 3D distribution of points with their corresponding aberrations correction is computed as :

$$\phi_{CGH} = arg(\sum_{n=1}^{N} e^{-i(\phi_{POS,n} + \phi_{AO,n} + \phi_n)}) \tag{4.3}$$

Here the aberrations are encoded in the CGH using a modal representation. Specifically the aberration phase is expanded as a linear combination of Zernike polynomials as follows:

$$\phi_{AO} = \sum_{i=j}^{N} w_j \cdot Z_j \quad with \quad j = \frac{k(k+2)+m}{2} \tag{4.4}$$

where Z_j is the Zernike polynomial function, j is the index of the expansion and w_j is the coefficient or weight. Zernike modes are a set of basis functions defined on a circle, in this case corresponding to the objective back aperture. We follow the *ANSI* order where the index j carries information about the radial (k) and angular (m) indices of the Zernike polynomials. Zernike modes with the same radial index k belong to the same aberration order [20]. These polynomials are widely used [21] and easily applicable. The low order modes are directly linked to identifiable aberrations such as defocus and spherical aberration allowing for clear interpretation of the results. The coefficients w_j of the Zernike polynomials are calculated in units of the wavelength and are hereby reported in μm.

The 3D CGH can include an isoplanatic phase term $\phi_{AO,n}$ which is the same across all the points in the field of view. This case is depicted in Fig.4.1(b) where a uniform vertical coma aberration (Z_8) with coefficient w = 1 μm is superimposed to the CGH on the SLM. The left image shows the phase of the coma aberration addressed to the SLM. The right shows a simulation of a 16-point grid pattern extending over a FOV of 80 μm at focal plane z = 7 μm in the sample, here all the points are affected by the same aberration.

Alternatively, as shown in Fig.4.1(c) anisoplanatic aberrations are encoded in the CGH. Here distinct aberration phases are targeted to different location of the FOV. The left image shows different aberration phases, from oblique astigmatism (Z_3) to horizontal secondary coma (Z_{18}) with the same coefficient w = 1 μm, for each point of the same grid shown in Fig. 4.1(b). The right image displays the image of the grid simulated at the focal plane where each point is degraded by different aberrations. The following equation describes the calculation to obtain the simulated images:

$$I_{sim} = |\mathcal{F}\{e^{i\phi_{cgh}} e^{i\frac{z\pi}{\lambda^2 f^2}\cdot(x'^2+y'^2)}\}|^{2\gamma} \tag{4.5}$$

where $e^{i\frac{z\pi}{\lambda^2 f^2}\cdot(x'^2+y'^2)}$ is a propagator factor to have the focal plane at a specific z plane, $\mathcal{F}$ is the Fourier transform applied to propagate the field from the pupil plane to the focal plane, γ is used to apply a gamma correction to enhance the features of the spots. The simulated images in Fig. 4.1(b,c) were generated with γ = 0.5.

4.1.2. Imaging system

The optical setup shown in Fig. 4.1(d) uses short pulsed near-infrared (NIR) light emitted by a mode-locked Ti:Sapphire laser (Coherent, Mira 900-F) tuned to a central wavelength of 800 nm with 76 MHz repetition rate. Power at the sample is controlled by adjusting the angle between a Glan-Laser Calcite Polarizer (GLP, Thorlabs, GL5B) and a half-wave plate (HWP). The beam is magnified by a telescope (lenses L1, f=25.4 mm and L2, f=150 mm) to fill the chip of the LCoS-SLM (Meadowlark Optics, P1920-600-1300-HDMI, pixel size: 9.2 μm) placed in a plane where the wavefront is nominally flat. The SLM is illuminated obliquely with an angle of 4.6° to be able to separate the modulated beam from the incident one. A mechanical shutter (S, Uniblitz, LS2S2Z1) installed at the focal point of lens L1 temporally gates the NIR illumination with a response of 2 ms. A second telescope (lenses L3, f=250 mm and L4, f=500 mm) magnifies the beam to fill the back aperture of the water immersion objective lens (O, Olympus XLUMPLFLN, 20X/NA 1.0). In the focal plane of lens L3, an inverse pinhole (IP, custom tungsten deposition, diameter 1.3 mm, on glass window of thickness 0.5 mm) blocks the zero-order diffraction spot. The focal lengths of lenses L3 and L4 are chosen to match the dimension of the SLM image at the back aperture of the microscope objective and the SLM chip. In this case the lateral resolution is only limited by the objective NA. TPEF is collected through the objective, transmitted through a low-pass dichroic mirror (Semrock, FF01-720/SP-25) and finally the image is formed by a tube lens (L5, f=300 mm). The image is relayed to the sCMOS camera (Andor, Zyla 4.2) by a 1:1 telescope (L6 and L7, f=150 mm) and an electrically-tunable lens (ETL, Optotune EL-16-40-TC-VIS-20D) lens which scans the signal at different depths. Brightfield (BF) images are acquired by transmission of a white light LED (Thorlabs, LEDW25E) placed at the opposite side of the objective.

As reported previously [22] the precision to address a CGH to a specific target depends on the number of pixels in the SLM and gray scale values available. We use a LCoS-SLM with 1920 x 1152 pixels so that the number of pixels in the shorter

axis permits a spatial accuracy better than 1 μm and also a high number of degrees of freedom when the SLM is used as adaptive element to correct for high-order aberrations. Regions of interest (ROIs) for generating the CGH can be located anywhere within the FOV which is a combination of lateral and axial FOV. The lateral FOV, defined the maximum tilt that can be applied on the first order of diffraction, is 391 μm. The theoretical axial FOV is 166 μm, where the SLM is the limiting factor for generating the CGH. Nonetheless, a trade off between the available lateral and axial FOV exists since increasing the axial displacement of a feature decreases the accessible amount of lateral displacement. Limitations in the applicable corrective patterns arise from aliasing as discussed in Appendix 4.A.1.

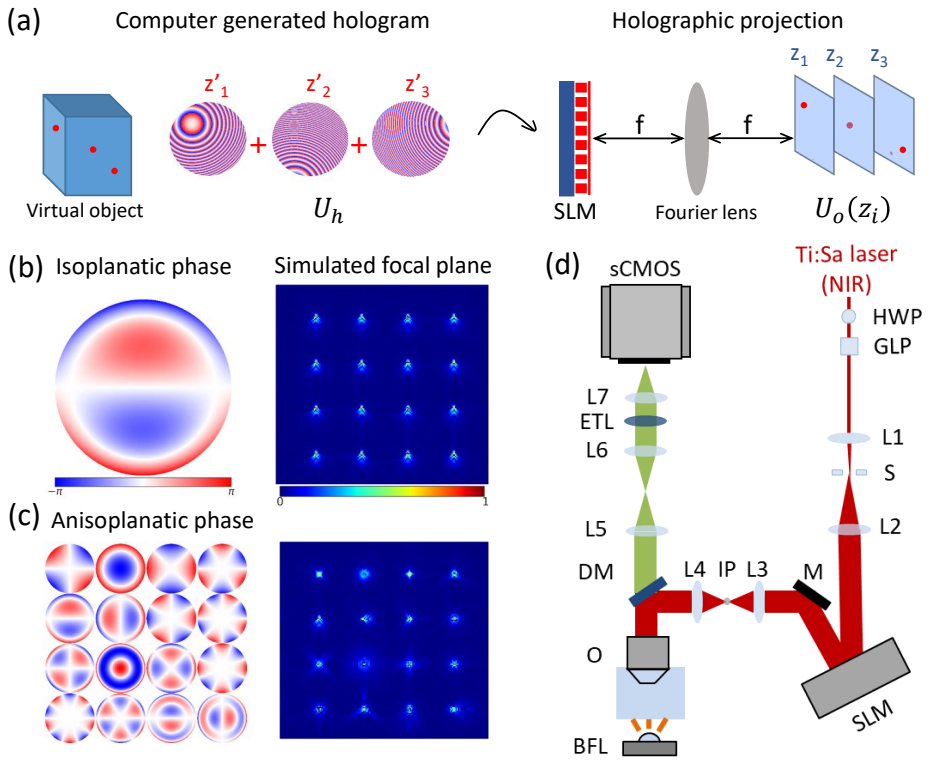

Figure 4.1: **Computer Generated Holography combined with Adaptive Optics.** (a) Concept of CGH and optical transformation needed to project a 3D digital hologram. U_h: spatial 2D Fourier transform of the target pattern U_o defined at different depths z_i, applied by lens of focal length, f. Each circle at the SLM represents the specific phase to generate the point at the chosen depth. (b) Left: Phase corresponding to vertical coma introduced as isoplanatic aberration to all the points in a grid pattern of 16 points. Right: Simulated image of the grid pattern affected by vertical coma with coefficient w = 1 μm (c) Left: Phase of the local aberrations introduced in the grid pattern. Each circle in the grid represents a different aberration expanded in the Zernike base from oblique astigmatism to secondary coma. Right: Simulated image of the grid pattern with local aberration with coefficient w = 1 μm applied to each point. (d) Implementation of CGH projection module (red lines) including widefield imaging path for measurement of TPEF (green lines; DM: dichroic; ETL: electrically tunable lens), not to scale.

4.1.3. Sensorless AO correction of the holographic stimulation

AO using direct measurement of the wavefront, e.g., with a Shack-Hartmann sensor, is generally limited to a single isoplanatic patch. For correction over multiple isoplanatic patches in the CGH, we instead chose a modal-based sensorless approach. Each aberration mode is imparted as a trial correction by the AO element and an image of the sample is acquired. The result is a collection of images for each of the optical aberration with a different bias coefficient. The best coefficient is chosen measuring a metric that quantifies image quality.

Sensorless methods require some *a priori* information about the system, such as a mathematical model describing how the corrective phase influences the chosen metric. For TPEF, the intensity of the fluorescence is known to depend quadradically on the peak intensity of the excitation light. Since we use widefield microscopy to capture fluorescence excited by the reconstructed CGH, we calculate the TPEF intensity of each spot in the pattern as the sum of gray scale pixel values within a bounding region,

$$I_F = \sum_i I_i^2. \tag{4.6}$$

In the ideal case of diffraction-limited spots in the CGH, the resulting TPEF spots should also be minimized in dimension. Bearing these two criteria in mind, we propose two different metrics M_1 and M_2, that combine the TPEF intensity with a feature that quantifies the spot shape. The metric M_1 combines the intensity I_F and the diameter D, determined as the maximum dimension of a single-spot CGH as shown in the following equation:

$$M_1 = \frac{I_F}{D} \tag{4.7}$$

where the diameter D is taken to be the larger of the vertical or horizontal axes of the single-point image at the focal plane. On the other hand metric M_2 combines the intensity the intensity I_F and the area A of a single-spot CGH as shown in the following equation:

$$M_2 = \frac{I_F}{A}. \tag{4.8}$$

Both area and diameter are measured after a threshold of $\frac{1}{e} \cdot I_{max}$ is applied. By dividing the intensity I_F with either the diameter or the area of the spot, we ensure that these combined metrics reach the maximum when the spot is more confined. Although the metric M_1 is sensitive to the variation of the spot shape on the lateral direction, the metric M_2 takes into account also any variation of the spot on oblique directions. For such reason metric M_2 is more robust to correct for aberrations that severely impair the shape of the points.

The metric is integrated in an optimization algorithm scheme. The optimization scheme affects both speed and efficiency of the correction. Those are equally important factors to correct aberrations in turbid samples. Here we use an hill-climb algorithm that sequentially loops over the Zernike polynomial base and explores a pre-defined range of bias coefficients for each Zernike polynomial. The corrections

found are sequentially applied to each Zernike term before moving to the next one. The optimal coefficient is found by fitting the metric data points with a combination of a Lorentzian function with a line (Eq. 4.10). Piston, tip, tilt and defocus are excluded in the optimization process because these are defined in the positioning of the points (Eq. 2) and may lead to loss of fidelity in the CGH as they cause displacement of the ROIs [23].

Isoplanatic correction

Isoplanatic corrections represent an average correction for the whole FOV. This correction may be optimal for points near the middle of the FOV, but sub-optimal for points near the edges. Algorithm 1 and Fig. 4.2 below highlight the main steps to implement such corrections.

Algorithm 1: Isoplanatic correction pseudo-code

```
initialization: calculate CGH with CS-WGS algorithm and select 1 point to
 correct
for Zernike order j in [1, N] do
    for Zernike weight w_i in [−w, w] do
        add isoplanatic aberration w_i · Z_j on SLM
        acquire camera frame
        get ROI centered around the chosen point
        calculate metric on the ROI
    fit metric values and find optimal weight w_j
    load found optimal weight for Zernike Z_j as isoplanatic correction onto
     the SLM
acquire the corrected image
```

Anisoplanatic correction

The pseudo-code for Algorithm 2 gives the key steps of the algorithm for anisoplanatic AO. Being an extension of the previous case to multiple point-like features in the FOV, the anisoplanatic algorithm provides local corrections. This feature is an important factor to compensate spatially inhomogeneous aberrations induced by turbid media such as biological tissues. A drawback compared to the isoplanatic correction process is that the CGH is recalculated after optimization of each aberration mode to encode the corrections just found. This extra step increases the total optimization time by a factor 2.6.

4.1.4. Image processing

To compare the TPEF images before and after AO correction, the intensity of ROI sub-images are normalized with respect to the corrected ROI sub-image (I^n) with the following normalization formula:

$$I_{norm} = \frac{I^i - I^n_{min}}{I^n_{max} - I^n_{min}} \tag{4.9}$$

Algorithm 2: Anisoplanatic correction pseudo-code

initialization: calculate CGH with CS-WGS algorithm select n points to optimize
for *Zernike order* j *in* $[1, N]$ **do**
  for *Zernike weight* w_i *in* $[-w, w]$ **do**
    add isoplanatic aberration $w_i \cdot Z_j$ on SLM
    acquire camera frame
    for *point* h *in* $[1, n]$ **do**
      retrieve patch centered around each point h in the FOV
      measure the metric on each patch
  fit metric and find optimal weight w_j for each point in $[1, n]$
  calculate CGH with CS-WGS with 20 iterations adding the correction $w_j \cdot Z_j$ found for all points n
calculate CGH with CS-WGS with 100 iterations adding all N Zernike phases with their optimal weights found for all points n
acquire the corrected image

where I^i is the intensity of pixel i in the image to normalize and I^n_{min} and I^n_{max} are pixels with, respectively, minimum and maximum value in the corrected image. The intensity improvement is quantified at each ROI in the normalized image through a line profile across the pixel of maximum intensity. The line profile data points are then fitted with a combination of a Lorentzian function with a line as follows:

$$L(x) = \frac{a \cdot \sigma^2}{(x - x_0)^2 + \sigma^2} + bx \tag{4.10}$$

where a is the amplitude, x_0 the center of the curve, σ the width of the curve and b the slope of the line. The uncertainty on each fit parameter is given by the square root of the diagonal elements of the covariance matrix [24]. The same function is also used to fit the measured metric values.

4.1.5. Sample preparation

Anisoplanatic correction of CGH was performed on both synthetic and biological samples. The synthetic sample was a fluorinated ethylene propylene (FEP, Bola, S2022-04) tube with an internal diameter of 0.8 mm and an outer diameter of 1.6 mm. The FEP tube is attached to a needle (B. Braun, 100 Sterican, 21G x 1 ½") and to a syringe (Braun, Omnifix F Solo 1 ml) and filled with a diluted solution of fluorescein (Invitrogen, F 1300) dissolved in demineralized water. The colour of the solution was vibrant dark yellow with an optical density of 0.056 in 0.8 mm path length measured through a spectrometer (BioDrop, μLITE). The same type of FEP tube is used to hold biological samples.

The biological sample was made from fixed tissue of zebrafish embryos. Zebrafish embryos were obtained by inbreeding adult fish from the casper strain [25]. Larvae were euthanized at 5 days past fertilization (dpf), fixed in a 1:1 solution of

embryo water (DI water with Instant Ocean salts, (60 μg/ml) with 0.0002% methylene blue) and 4% para-formaldehyde in phosphate saline buffer (PBS) for 2 hours, rinsed 3x in PBS, and stored in PBS at 4°C until the experiment. For the experiment they were mounted into a straightened FEP tube in a solution of 1.5% low-melting temperature agarose (Sigma-Aldrich, A4018) in embryo water and fluorescein.

4.2. Results

4.2.1. Comparison of sensorless AO metrics for widefield TPEF

We first tested each of the metrics in the isoplanatic correction algorithm (Fig. 4.2). From each TPEF image, a 40x40 pixel sub-image was retrieved around a single ROI selected for isoplanatic correction (Fig. 4.2(a), left). The metric I_F was calculated from a 10x10 pixel patch centered around the ROI (Fig. 4.2(a), middle), while the area to compute the metric M_2 is evaluated on the binary image (Fig. 4.2(a), right). This image was obtained by applying a threshold to the original sub-image. A range of 15 bias coefficients in the interval $[-3, 3]$ μm was explored for each Zernike polynomial. Those trial aberrations were sequentially applied to the point chosen for the correction and an image collected as shown in the progression of 40 x 40 sub-images in Fig. 4.2(b), top. Once a progression of images as function of the bias aberration was acquired, we measured different metrics using Eq.6 – Eq.8. As seen in Fig. 4.2(c), each metric gives a different optimal coefficient to correct spherical aberration (Z_{12}).

4.2.2. Experimental validation of anisoplanatic AO

To validate the anisoplanatic AO method, we calculated a test pattern with specific aberrations simulated computationally. We then experimentally applied either the isoplanatic and anisoplanatic algorithm to optimize the reconstructed hologram based on its TPEF image. The test pattern consisted of a 16-point grid covering an area of 150 x 150 μm, where spherical aberration (Z_{12}) was introduced at point 1 and point 7 with weights w = -2 μm and w = 2 μm, respectively. This CGH was projected into a chamber filled with fluorescein solution, where sample-dependent aberrations were expected to be minimal. Figure 4.3 shows the results of both isoplanatic and anisoplanatic algorithms using the intensity-diameter metric, M_1. For both algorithms, the correction procedure started with Z_{12} and then cycled through Zernike coefficients up to the third aberration order (from Z_3 to Z_9). This order of modes was chosen *a priori* because first correcting for dominant modes improves the accuracy of the final correction [26]. In the initial TPEF image of the hologram (Fig. 4.3(a), left), points 1 and 7 are visibly distorted due to the added spherical aberration. As expected, when isoplanatic correction was performed for point 7, the intensity of point 7 improved by a factor of 10.6 whereas all the other points were degraded by this correction (Fig. 4.3(a), middle). In contrast, when anisoplanatic correction was performed on all points, the intensity of all spots improved by an average factor of 2.7 (Fig. 4.3(a), right).

Analysis of the retrieved Zernike coefficients, shown in Fig. 4.3(b), showed that the spherical aberrations (Z_{12}) retrieved for points 1 and 7 under anisoplanatic

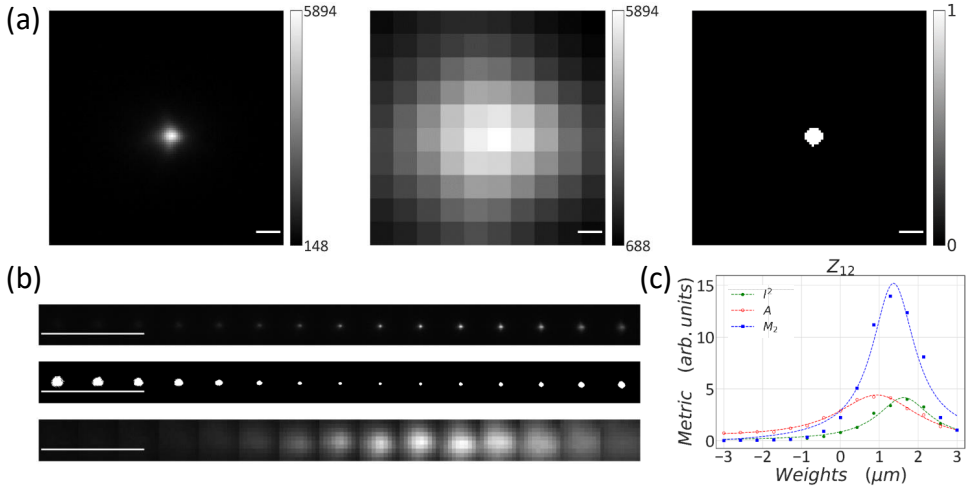

Figure 4.2: **Definition of image-based metric influences correction.** (a) Left: 40 x 40 pixel patch around the ROI is used for optimization. Scale bar: 2 μm. Middle: 10x10 patch to quantify the I_F metric. Scale bar: 0.2 μm. Right: binary image to measure the area metric. Scale bar: 2 μm. (b) Top: Progression of sub-images acquired as a function of spherical aberration (15 values for coefficients for Z_{12}). Scale bar: 50 μm. Middle: binarized version of the progression to compute the area metric. Scale bar: 50 μm. Bottom: progression of the 10 x10 patches around the ROIs to calculate the I_F metric. Scale bar: 5 μm (c) Metric values as a function of different bias spherical aberration, for Z_{12}. Area: red dots, I_F: green circles; combined metric (M_2): blue squares; dashed lines: Lorentzian fit.

algorithm (orange bars) were w = 2.34 μm and w = -1.87 μm, respectively, while contributions for other orders were non-zero. For comparison of the retrieved and simulated aberrations, we also obtained a baseline anisoplanatic correction of the system using a 4x4 test pattern with no added spherical aberration (blue bars). A slight positive spherical aberration was found in the baseline at the locations of points 1 and 7, respectively, w = 0.26 μm and w = 0.15 μm. This can explain why the retrieved coefficients for spherical aberration is slightly higher than w = 2 μm for point 1, and slightly higher than w = -2 for point 7. We estimated the error on the Zernike coefficient as the standard deviation in the lower orders (Z_3–Z_9) recovered from the three independent corrections for point 7 (baseline, isoplanatic, and anisoplanatic) to be 0.10 μm. Therefore, these data show that the anisoplanatic method accurately retrieves the applied Z_{12} coefficient. The anisoplanatic corrective phase patterns applied to the SLM are depicted in Fig. 4.3(c).

Closer inspection of the xy and yz projections of the TPEF image of point 1 (Fig. 4.3(d)) illustrates the improvement in intensity and shape after the anisoplanatic correction in both the lateral and axial direction. Both images are normalized with respect to the corrected image and the aberrated images are shown with a reduced dynamic range for the pixel values for visualization purposes. The intensity improvement and the spot size are quantified on the intensity profiles (Fig. 4.3(e)) taken from a line profile across the pixel of maximum intensity. The dashed lines on

the images in Fig. 4.3(e) reveal that spherical aberration displaced the point laterally along the y direction as well as axially. The axial displacement is compensated in the corrected image where intensity is also recovered. The small lateral displacement is most likely due misalignment between the rear pupil of the objective and the SLM plane.

The shape and size of the TPEF spots improved for all the points in the grid. Table 4.1 shows the reduction in mean lateral and axial dimensions determined as the full width half maximum (FWHM) of a Lorentzian fit to the measured line profile. The FWHM of points focused in the dye solution is an indication of the resolution of the holographic projections because the TPEF image of point-like features are the convolution between the excitation and emission point spread functions (PSFs). Since the sample is a homogeneous solution, TPEF can be generated throughout the geometrical focus. We can take the dimensions of the squared intensity distribution I_{ex}^2 as the upper bound for the spot diameter expected from an ideal Gaussian excitation focus with waist $w_o = \frac{\lambda}{\pi NA}$ and Rayleigh range $z_R = \frac{nw_o}{NA}$, where n represents index of refraction. The lower bound for the FWHM of the spots detected is limited by the dimension of the Airy disk of fluorescence generated by an infinitesimally small TPE focus, given by $R_{xy} \approx \frac{2}{3}\frac{1.22\lambda}{NA}$, and depth of field $R_z = \frac{2n\lambda}{NA^2}$, where λ_{em} = 520 nm. Noting that the size of the optimized TPEF spots is still larger than either the theoretical beam waist or PSF, we can conclude that the AO optimization of the excitation beam alone does not produce a diffraction-limited image. This can be expected because the system does not correct for aberrations in the pathway of the fluorescence.

	Raw FWHM	Corrected FWHM	$2w_o$	Ideal PSF_{em}
Lateral [μm]	0.93 ± 0.24	0.75 ± 0.05	0.51	0.42
Axial [μm]	1.85 ± 0.44	1.50 ± 0.11	0.67	1.38

Table 4.1: **Dimensions of two-photon excited fluorescence spots. FWHM values are the mean and standard error on the mean of spots in Fig. 4.3(a).**

4.2.3. Correction on synthetic sample: FEP tube filled with fluorescein

Next we characterized anisoplanatic AO in an aberrating sample, a FEP tube filled with a fluorescein solution (Fig. 4.4(a)). The FEP tube has an index of refraction of n = 1.344 at 589 nm, which is near to that of water (n = 1.3324) so introduces relatively weak aberrations compared to sample containers made of other common materials (e.g. borosilicate glass) [27]. We expect that the cylindrical geometry of the capillary affects vertical astigmatism [28] (see Appendix 4.A.2.) A CGH was calculated for a 4x4 grid with a spacing of 25 μm between points. The TPEF image of the CGH grid projected into the sample is showed in Fig. 4.4(b), left.

On this image we performed the anisoplanatic correction with the metric M_2, correcting up to the eighth aberration order, corresponding to Zernike coefficients Z_3–Z_{44}. The correction process took 30 minutes, corresponding to calculation of

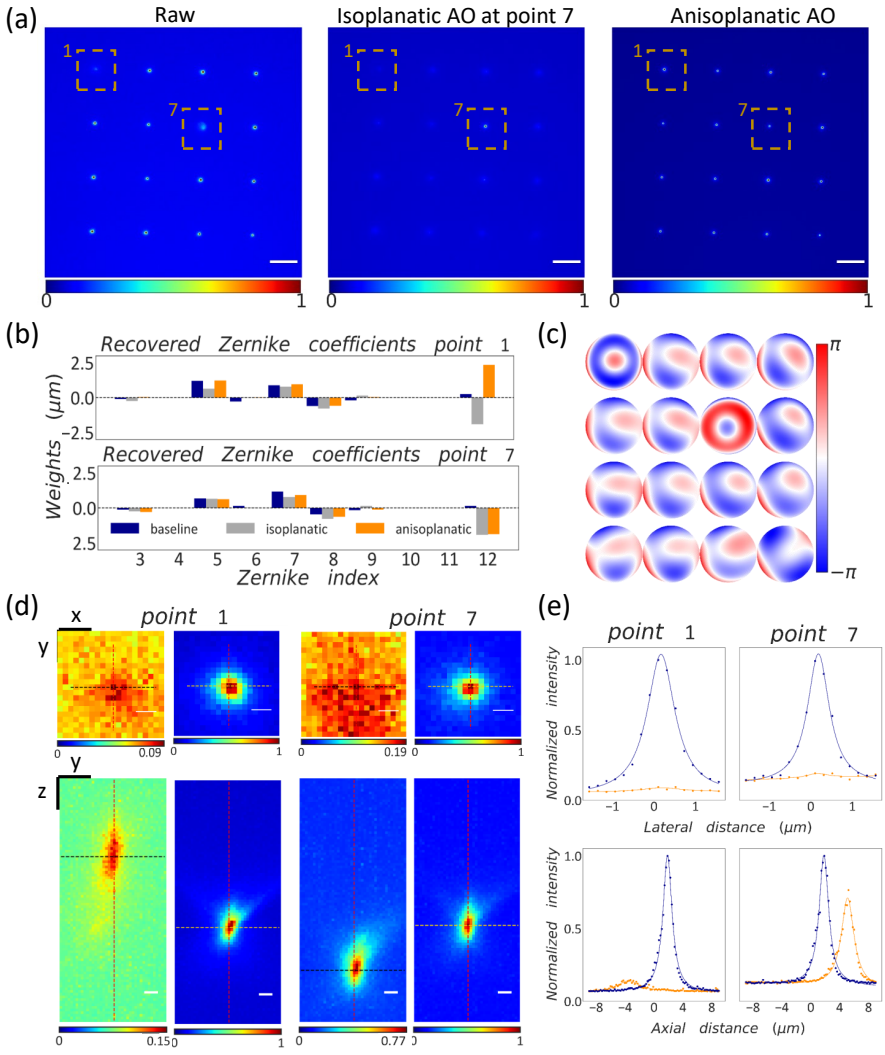

Figure 4.3: **Isoplanatic and anisoplanatic corrections applied to CGHs projected into free solution.** (a) TPEF images of 16-point grid CGH. Left: grid with -2 μm and 2 μm spherical aberration at points 1 and 7 respectively. Middle: grid with isoplanatic correction at point 7. Right: grid with anisoplanatic correction.The images are normalized with respect to themselves and they are enhanced by a factor of 3 to help the visualization. Scale bar: 25 μm. (b) Bar plot of Zernike coefficients for points 1 and 7. Blue bars correspond to the baseline anisoplanatic correction of the grid CGH; gray and orange bars, respectively, correspond to isoplanatic and anisoplanatic corrections of the CGH with simulated aberration. (c) Anisoplanatic phase maps at each point in the grid. (d) xy image and yz image of point 1 and 7 before and after anisoplanatic correction. Scale bar xy: 750 nm, scale bar yz: 1 μm. (e) xy (upper) and yz (bottom) line profiles of point 1 and 7 before and after correction. Blue dots: corrected line profile; orange dots: aberrated line profile; continuous lines: Lorentzian fit of the data points.

43 unique CGH and acquisition of 630 images testing 15 weights per order for 42 orders. The resulting corrected image is reported in Fig. 4.4(b), right. The corrective phase maps shown in Fig. 4.4(c) provide a full characterization of the sample-induced aberrations across the central 100 μm of the FOV. As anticipated, vertical astigmatism (Z_5) was one of the dominant aberrations given the cylindrical geometry of the sample under examination (see Appendix 4.A.2). Moreover, we also found a prominent contribution for spherical aberration (Z_{12}). As visible from the corrective phase maps (Fig. 4.4(c)), specific ROIs also had contributions from higher-order aberrations, as in the case of 3 μm coefficient for Z_{36} at point 11. The lines profiles across the pixel of maximum intensity for the raw (orange) and corrected (blue) spots represented in Fig. 4.4(d) reveal an average intensity improvement factor of 2.07 ± 0.33.

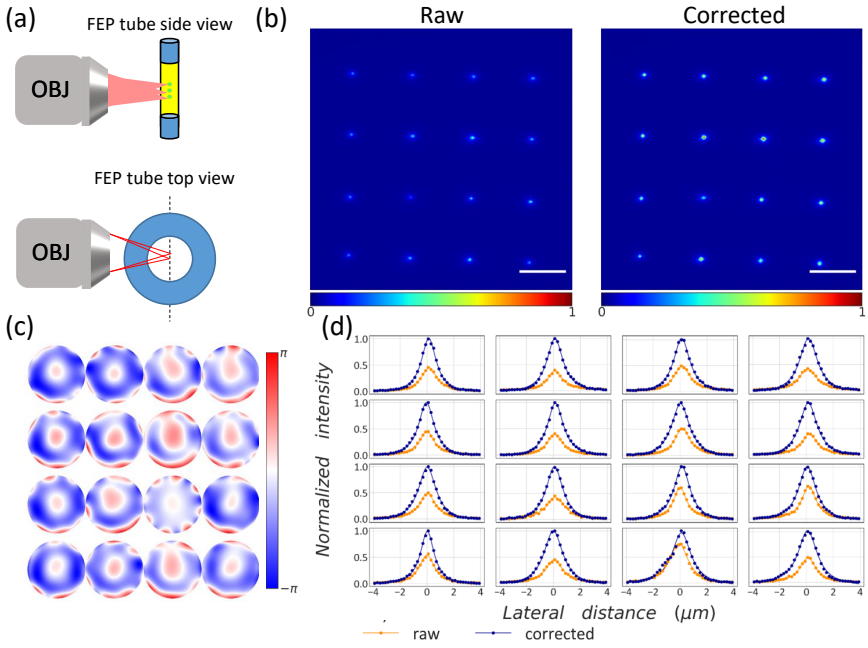

Figure 4.4: **Anisoplanatic correction on sample-induced aberrations in FEP tube.** (a) Top and side view sketches of the synthetic sample, a FEP tube with 0.4 mm thick wall. (b) Left: TPEF image of 16 points grid used to retrieve anisoplanatic correction. Right: Corrected TPEF image. Scale bar is 25 μm (c) Local phase maps retrieved for each point in the grid. (d) Line profiles across the pixel of maximum intensity of aberrated (orange dots) and corrected (blue dots) points show a 2-fold gain in intensity for most of the corrected points. Continuous lines show Lorentzian fit of data points.

We then asked whether the AO corrections obtained for one hologram would be sufficient to optimize a novel point cloud pattern extending over the same FOV. We calculated a second CGH of 12 points randomly distributed over the same 100 x 100 μm area, shown in Fig. 4.5(b), left, together with the location of reference points from the grid CGH (red dashed lines). For each point in the random pattern, the corrective phase was calculated as a distance-weighted average of the local

corrective phases found for all points in the reference grid. The weight coefficient was inversely proportional to the distance between the point to correct and each point in the reference grid CGH, as described in Fig. 4.5(a) and by the following formula:

$$w_i = \frac{\sum_k \frac{w_k}{d_{ki}}}{\sum_k \frac{1}{d_{ki}}} \tag{4.11}$$

where w_i is the coefficient of a given Zernike mode for a point i in the random pattern, w_k are the coefficients of a given Zernike mode for all the k points in the reference pattern, and d_{ki} is the distance between point i and point k.

Comparison of the TPEF images of the random points before and after AO correction (Fig. 4.5) indicates that the distance-weighted anisoplanatic correction improves the spot intensity. The resulting corrective phase maps in Fig. 4.5(c) are more homogeneous between the random ROIs compared to the ROIs in the reference grid. The weighted average of points from across the whole FOV can be seen as diluting each local correction. Nonetheless, by applying aberrations based on the distance-weighted average correction, the random points increased their average TPEF signal by a factor of 2.07 $\pm$ 0.17 on average, as depicted in (Fig. 4.5(d)). Since the average intensity improvement is comparable to the one obtained on the reference grid (Fig. 4.4), we can conclude that the reference set of anisoplanatic corrections sampled at 25 μm intervals are sufficient to correct for different patterns covering the original FOV. In a sample with greater complexity, the needed sampling distance can be expected to change. However, for points that are closer together we observed a coupling of the corrections even if the ROIs belong to different anisoplanatic patches (see Appendix 4.A.3).

The same approach can be extended to a 3D pattern. To test this experimentally, we first retrieved anisoplanatic corrections for a reference 3D CGH made of 10 points randomly distributed over a volume of 100 x 100 x 50 μm^3 where the axial direction was sampled at a spacing of Δz = 7 μm (Fig. 4.5(f)). Here we optimized up to the fourth aberration order, corresponding to Zernike modes in the interval Z_3–Z_{14}, testing 9 bias coefficients in the interval [-2, 2] μm for each mode. This smaller number of optimization parameters still provided good intensity improvement for this sample, while also reducing the number of measurements overall. In this case the correction process took 26 minutes. In three dimensions the correction process was longer compared to the two dimensional case since it was necessary to acquire an image at each depth by changing the ETL voltage. Hence, the optimization time increases linearly with the number of the z depths explored.

As in the 2D case, all points in the 3D reconstruction improved in TPEF intensity at the focal plane. On average the improvement factor was 1.76 ± 0.25, as reported in Fig. 4.5(g). Figure 4.5(h) shows that the ROIs after correction are displaced with respect to their positions in the original volume. Displacements were calculated as the distance between the centroids of spots retrieved from the starting image and centroids of spots retrieved from image following AO. The average lateral displacement was 0.6 μm while the average axial displacement was 0.9 μm. Lateral displacement can be introduced by Zernike polynomials (see Eq. 4.4) with

odd k index and $m = \pm 1$, such as coma aberration, while the axial shift can be addressed to radial Zernike modes with even k and $m = 0$.

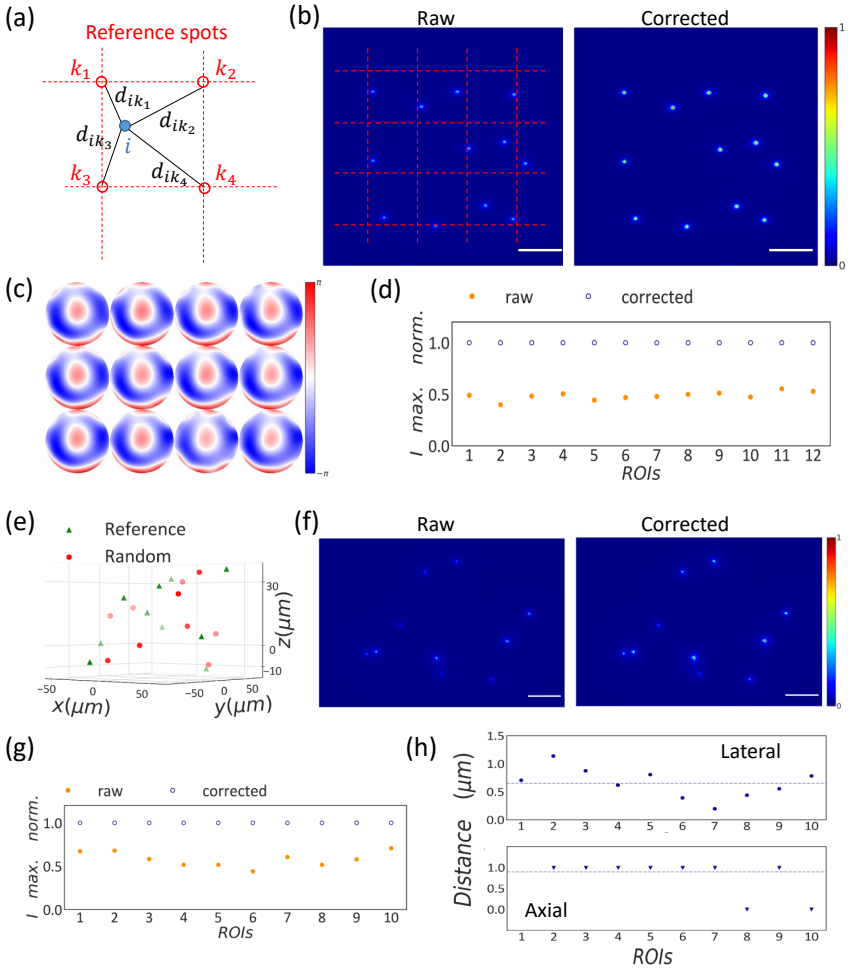

Figure 4.5: **Distance-weighted anisoplanatic correction on 2D and 3D CGH projected into FEP tube with uniform fluorescent solution.** (a) Calculation of the distance-based coefficients to apply the distance-weighted average anisoplanatic correction to point i using reference points k, where d_{ik} is the distance between points. (b) Left: TPEF image of 12 points randomly distributed across the same FOV of the reference grid (dashed red lines). Right: TPEF image corrected with the distance-weighted averaged anisoplanatic approach. (c) Local phase maps applied to each point in the random pattern. (d) Comparison of maximum intensity as a function of each measured spot before (orange dots) and after (blue circles) AO correction. (e) 3D plots of the reference (green squares) and random (red dots) coordinates for the CGHs. (f) Left: Maximum intensity projection of TPEF image of 10 points randomly distributed in 3D over a FOV of 100 x 100 x 50 μm^3. Right: Same image corrected with a distance-weighted average of the anisoplanatic corrections for the reference 3D pattern laying. (g) Comparison between maximum intensity before (orange dots) and after (blue circles) the weighted averaged anisoplanatic correction (h) Lateral (top) and axial (bottom) distance between the center of the spots before and after correction. The dashed lines show the average values. Scale bar is 25 μm.

4.2.4. Correction on fixed biological sample

Finally, to validate our method on highly aberrated samples we applied the aniso-planatic correction to a CGH projected through approximately 140 μm of tissue in the tail of a 5 dpf zebrafish embryo embedded in a mixture of 1.5% low-melting temperature agarose and fluorescein. As shown in Fig. 4.6(a), top, each point targets a different anatomical location in the tail. The lateral points are projected through muscles areas whereas the middle point passes through the notochord. The CGH extends over a lateral FOV of 115 μm. The TPEF signal generated behind the tissue, is degraded as shown in Fig. 4.6(a), second row. The middle point is brighter compared to the lateral ones revealing the inhomogeneity of the tissue.

To compensate for the aberrations we initially applied to each point the local corrections found for the same pattern projected into the FEP tube filled with fluo-rescein. Those corrections accounting for FEP-induced aberration already improve our pattern projected into the tissue as shown in Fig. 4.6(a), third row. Further improvement is achieved when we corrected for tissue-induced aberration by using as starting point the pattern corrected for the FEP-induced aberrations. This final result is shown in Fig. 4.6(a), bottom. To retrieve those corrections we optimized up to the eighth aberration order, corresponding to Z_3–Z_{44}, using the intensity-diameter combined metric M_1 (Eq. 4.7). Analysis of the xy profile of TPEF for each ROI, shown in Fig. 4.6(b), reveals that all three points improve in terms of intensity and shape. However, the correction has a stronger impact on the middle point than the lateral points, as confirmed by the intensity profiles in Fig. 4.6(c). The average intensity improvement was 3.09 ± 0.26.

Figure 4.6(d) shows the contribution to each local corrective phase in the case of FEP-induced (top) and tissue-induced (bottom) aberrations. In this experiment we observed that the improvement of the metric M_1 as function of Zernike order is different than in the case of FEP-induced aberrations. Here, as expected, we have an increase of about 2-fold when we use more than 10 Zernike modes and after this increase the correction reaches a plateau with little additional improvement from higher orders (see Fig. 4.6(e), top). On the other hand, the correction of tissue-induced aberrations starting from the FEP parameters, led to greater contributions from higher-order modes. From the bar plot of the Zernike coefficients in Fig. 4.6(f), we observed that vertical astigmatism (Z_5) has a prominent contribution, as well as higher order aberrations (Z_{27}, Z_{35} and Z_{36}).

Inspection of the full sequence of bias corrections tested during optimization, shown in the Appendix (Section 4.A.4, Fig. A4), casts doubt whether the hill-climbing algorithm finds a global maximum value across all Zernike modes. For comparison, the same experiment was also carried out by correcting for aberrations directly on the tissue without performing the extra step to compensate for the FEP tube. This approach provided a lower average improvement in the TPEF intensity, limited to a factor of 1.59 ± 0.04, as reported in Appendix (Section 4.A.4, Fig. A5).

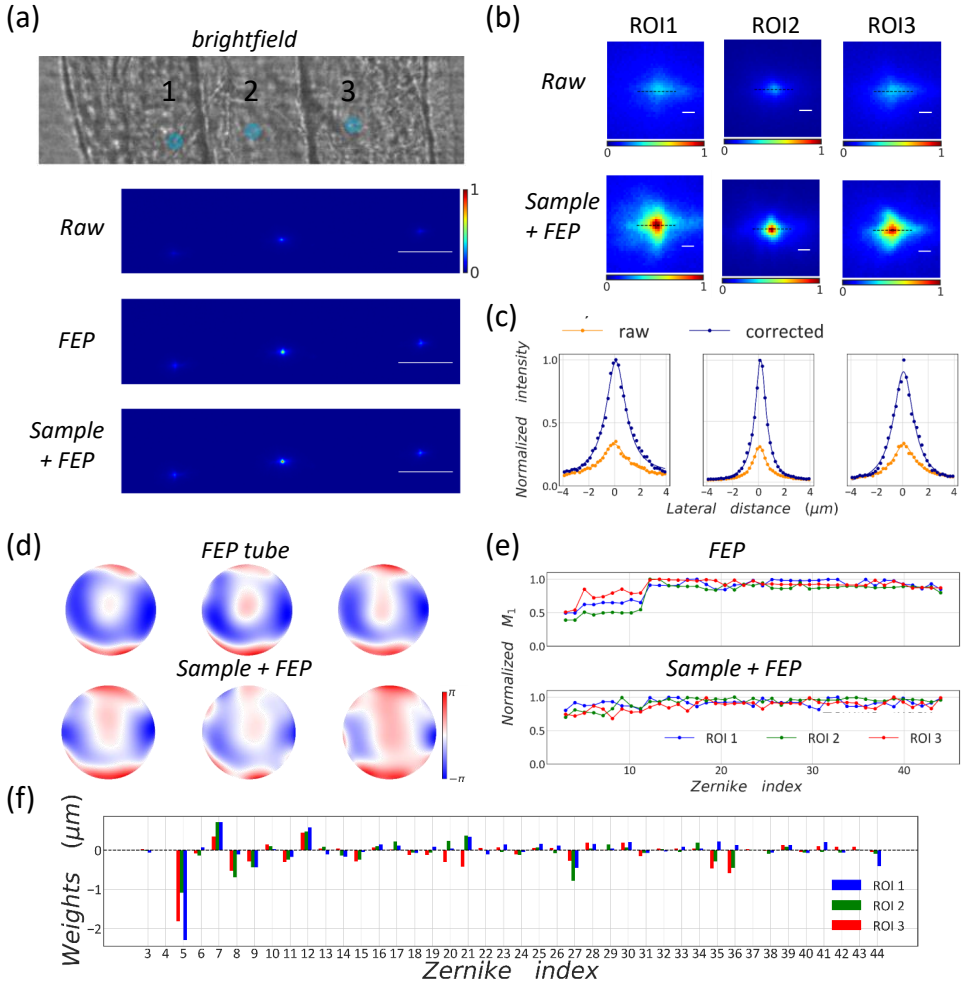

Figure 4.6: **Anisoplanatic correction through fixed zebrafish tissue.** (a) Brightfield image of the embryo tail (lateral view) showing the location of the targeted ROIs in cyan extending over a lateral FOV of 115 µm. Also shown are TPEF images of the uncorrected CGH projected into the embryo tail (row 2), and TPEF image following correction of FEP tubing only (row 3) and correction of both FEP tube and tissue (row 4). Scale bar is 25 µm. (b) Zoom in of xy images of the ROIs. Top: Aberrated case, bottom: corrected for FEP and tissue. Scale bars: 1 µm. (c) xy line profiles across the dashed lines in c. Blue dots: corrected, orange dots: aberrated, continuous lines: Lorenzian fit on the data points. (d) Corrective phase maps for each point. Upper row: FEP-induced aberrations, bottom row: tissue-induced aberrations. (e) Intensity improvement as function of the order of Zernike correction, tested in order of index in FEP tube only (FEP) or mounted issue (sample + FEP). (f) Bar plot of Zernike coefficients for each ROI corrected for FEP and tissue.

4.3. Discussion

Anisoplanatic adaptive optics has already been shown to improve image quality in laser scanning confocal microscopy where the anisoplanatic approach is used to

correct the one-photon excitation light of scanning lattice microscope using confocal detection [15]. There the anisoplanatic corrections were encoded, together with the spots forming the scanning lattice, as a CGH on a SLM. Differently, in this paper we applied anisoplanatic AO to arbitrary CGH projections using two-photon excited fluorescence as an indirect measure of peak pulse intensity. We demonstrated that correction of local aberrations in point-cloud CGHs projected into either synthetic and biological samples improved the TPEF signals by at least 2-fold. We also characterized the limitations of the approach using widefield camera-based imaging. While the dimensions of features in the corrected point cloud CGHs, quantified as FWHM of the TPEF spots, improved compared to the case before correction, diffraction limited spots were not obtained due to the residual aberrations in the fluorescence emission path of our optical system. In fact, the TPEF images depend on the convolution between the stimulation and the emission PSFs. Since the method described here addresses only aberrations in the stimulation path, images obtained following AO correction still appear aberrated, (e.g., the quality of AO-corrected spots projected into tissue in Fig. 6(a) is lower than spots projected into less complex sample of Fig. 4(b)). Remaining distortions could be compensated by installing an adaptive element along the detection path [15].

In this paper anisoplanatic adaptive optics is performed in a sensorless scheme, hence it does not require any additional component to measure the wavefront. This scheme supports a very simple optical setup where the adaptive optics element is the same SLM used to project and correct CGHs. Aberration corrections are simply included as a modification of a target CGH. This aspect highlights an advantage of sensorless approaches over direct wavefront sensing. In the latter, the wavefront distortion is directly measured (e.g. with a Shack-Hartmann sensor) on the light emitted by a guide star or on light back-scattered from the sample. Measured distortions are corrected through an adaptive element in a plane conjugated with both the objective rear pupil and the wavefront sensor. As demonstrated by Wang, *et al.* [29], direct wavefront sensing enables to recover diffraction limited resolution in living zebrafish embryos over large volumes (240 μm^3) in both laser scanning confocal and two-photon excited fluorescence microscopy. Nonetheless, wavefront sensors add an extra layer of complexity to the existing microscope and can introduce non-common-path errors. Scattering could make a wavefront sensor solution unfeasible when the scattering components prevail over the ballistic components in the wavefront measurement. Most importantly, Shack-Hartmann sensors measure the aberration of only one isoplanatic patch at a time [10] making it difficult to implement for anisoplanatic field corrections.

Notably, a recent work by Ancora and colleagues [30] presents a new method to measure locally the wavefront in a widefield microscope pupil and to apply anisoplanatic correction of aberration through a multi-region deconvolution approach. The aberration detection is based on a spinning subpupil aberration measurement (SPAM) where a subaperture is scanned across the microscope's pupil via a motorized device and it is able to measure local PSFs. This module can be integrated in the detection path of any fluorescent microscope as described in [31] where it is integrated into a light sheet microscope. Here, the SPAM module operates in closed

loop with a deformable lens to correct the aberrations in the center of the FOV while the residual distortions at the edges are compensated with the multi-region deconvolution approach.

Sensorless approaches have been realized in many flavors, from pupil segmentation zonal methods to modal-based AO. In pupil segmentation strategies, the objective pupil is divided into sub-regions to measure and correct aberrations. Those sub-regions are sequentially illuminated to measure the local wavefront slope from the image shift. Ji, *et al.* [8] implemented this technique in a two-photon microscope and corrected for complex aberrations in mouse cortical slices at 400 μm depth to provide near diffraction-limited resolution imaging. A generalized framework for sensorless approaches by Booth, *et al.* [32] concluded that in general pupil segmentation zonal methods, whereas they provide better performances for high order aberration, they are less robust to noise than modal methods.

As shown in a recent work by May, *et al.* [18], sensorless sample-conjugated AO enables to correct scattering on multiple anisoplanatic patches distributed over large FOVs for application on two-photon imaging on both fixed and living microglia in mouse hippocampal tissue. Here local corrections are provided within short time scales on the order of 10 s. Such correction speed is achieved thanks to the algorithm used for the correction search, which is a fast converging phase retrival method called Dynamic Adaptive scattering compensation Holography (DASH)[33]. Moreover the use of the photomultiplier tube (PMT) detector enables to collect fluorescent signals at a faster rate than an sCMOS camera.

In the work presented here, the speed of the optimization is constrained by the number of images acquired to assess the optimal correction as well as by the complexity of the aberration. When the sample introduces severe distortions an higher number of Zernike modes has to be included increasing the optimization time. The speed factor is particularly limiting when dealing with samples where the fluorescent signal comes from a limited pool of proteins. Here the results can be impaired by sample drift, photobleaching and other phenomena resulting in loss of intensity during the optimization process, as reported in Appendix (Section 5.A.5, Fig. A6). Moreover a faster optimization translates in a decreased exposure of the sample. This is a critical aspect when handling living samples where photodamage, both thermal and photochemical, could impair the normal physiology of the sample under investigation [34]. To speed up the correction process, we could retrieve an anisoplanatic correction on a reference CGH that samples the FOV and then apply this reference correction to other patterns, as demonstrated in Section 4.2.3. Applied to the context of holographic photostimulation in living tissue, the reference corrections would best be retrieved on the TPEF signal from guide-star fluorophores (e.g., beads injected in the tissue). The caveat of this solution is that the guide-stars need to be adequately distributed over the same FOV of the target ROIs to provide sufficient sampling of the local aberrations.

Another improvement to increase the speed of the correction process on complex samples, was to perform a step-wise correction of first the sample holder (e.g., FEP tube) and use these values as a starting point for tissue correction. We found this approach improved the overall performance of the optimization process com-

pared to a single-step correction of the full sample.

The AO algorithm itself may be sped up in several ways. For example, the calculation of CGHs can be accelerated by use of a GPU, as recently proposed by Pozzi, *et al.* [35]. During the optimization process an updated CGH is calculated after each Zernike mode correction. This step takes several seconds and this dead time could be reduced in the order of milliseconds by introducing the GPU calculation. Moreover, a non-iterative algorithm based on convolutional neural network with unsupervised learning is also available to compute CGHs at video rate reducing at least 10 times the computational time with respect to standard iterative algorithms as Gercheberg-Saxton [36]. A further possibility to speed up the whole correction algorithm is to replace the sequential search of Zernike modes, which is quite inefficient, with a smarter search algorithm. As shown in Appendix (Section 5.A.4, Fig. A4), most Zernike coefficients tested in the hill-climbing search algorithm yielded low metric values, whereas it may be more efficient to vary more than one coefficients value in combination, or in non-sequential order. For instance, in the work of Verstraete, *et al.* [37], the range of the coefficients explored for each Zernike mode is based on the previous measurement with a random perturbation to ensure an adequate exploration of the bias coefficients space.

Another limiting factor of our method is cross-talk between different modes. This drawback arises from lack of orthogonality in the polynomial base used to model the aberrations. In fact, orthogonality is a necessary property to express the metric as a quadratic function of the chosen base [23]. In our case, Zernike polynomials are not an orthogonal basis with respect to either of our combined metrics M_1 and M_2, and the order in which the modes are optimized and applied matters. Other aspects to consider are the accuracy of the correction, which is affected by different parameters such as noise and cross-talk between the modes. The major factors contributing to noise in such experiments are Poisson photon noise and changes of the sample over the optimization time, mainly due to sample drift and photobleaching. Noise in the image can induce the algorithm to find a wrong maximum. This effect is mitigated when the maximization of the metric is realized through a fitting process [38], but the number of data points per mode also affects the accuracy of the fit and, ultimately, the performance of the AO. As discussed in [26], the number of measurements for each point needs to be greater than the number of fit parameters.

Finally, we note some displacement of the spots after correction. For instance, with the distance-weighted average anisoplanatic correction to a 3D CGH, we observed that the corrected points were displaced laterally and axially from their original position. The shift is likely due to the polynomial base used, which does not guarantee invariance of the geometrical center of the PSF during the correction. This is a common problem in non-linear excitation schemes where the the PSF is non-linearly proportional to the light intensity. A solution to this problem could be to develop a polynomial base that conserves the first moment of the square intensity or implement an experimentally-calibrated shift-less basis set [39].

4.4. Conclusions

Sensorless adaptive optics techniques have been extensively employed to improve signal and optical resolution in the context of imaging though turbid samples. In this paper we apply sensorless AO techniques to correct local aberrations in the context of projection of multi-point holograms through turbid media. We demonstrated an anisoplanatic AO approach that can compensate for both system and sample-induced aberrations in synthetic and biological samples. Our strategy does not require additional elements to an existing optical setup for holographic projections, but rather uses optimization of two-photon excited fluorescence as a guide star. We can envision applications in optical trapping, parallel laser writing through two-photon polymerization and parallel photostimulation of optogenetics actuators in living cells or intact animals. If integrated with a light sheet microscope as a setup for optogenetics, the stimulation module presented can simultaneously excite multifocal points targeted to regions of interest within the sample, while the light sheet microscope provides flexibility to readout fluorescence signals, e.g., image calcium activity from small samples, such as larval zebrafish.

References

[1] J. E. Curtis, B. A. Koss, and D. G. Grier, "Dynamic holographic optical tweezers," *Optics Communications*, vol. 207, pp. 169–175, 2002.

[2] A. K. Jayasinghe, J. Rohner, and S. Hutson, "Holographic UV laser microsurgery," *Biomedical Optics Express*, vol. 2, no. 9, pp. 2590–2599, 2011.

[3] G. Vizsnyiczai, L. Kelemen, and P. Ormos, "Holographic multi-focus 3D two-photon polymerization with real-time calculated holograms," *Optics Express*, vol. 22, no. 20, pp. 24217–24223, 2014.

[4] V. Emiliani, A.E. Cohen, K. Deisseroth, and M. Häusser., "Symposium All-Optical Interrogation of Neural Circuits," *The Journal of Neuroscience*, vol. 35, no. 41, pp. 13917–13926, 2015.

[5] P. S. Salter and M. J. Booth, "Adaptive optics in laser processing," *Light: Science and Applications*, vol. 8, no. 1, pp. 24122–24128, 2019.

[6] M. J. Booth, "Adaptive optics in microscopy," *Philosophical Transactions of the Royal Society A: Mathematical, Physical and Engineering Sciences*, vol. 365, no. 1861, pp. 2829–2843, 2007.

[7] J. M. Beckers, "Adaptive Optics for Astronomy: Principles, Performance, and Applications," *Annual Review of Astronomy and Astrophysics*, vol. 31, no. 1, pp. 13–62, 1993.

[8] N. Ji, D. E. Milkie, and E. Betzig, "Adaptive optics via pupil segmentation for high-resolution imaging in biological tissues," *Nature Methods*, vol. 7, no. 2, pp. 141–147, 2010.

[9] O. Azucena, J. Crest, S. Kotadia, W. Sullivan, X. Tao, M. Reinig, D. Gavel, S. Olivier, and J. Kubby, "Adaptive optics wide-field microscopy using direct wavefront sensing," *Optics Letters*, vol. 36, no. 6, pp. 825–827, 2011.

[10] D. Wilding, P. Pozzi, O. Soloviev, G. Vdovin, and M. Verhaegen, "Adaptive illumination based on direct wavefront sensing in a light-sheet fluorescence microscope," *Optics Express*, vol. 24, no. 22, pp. 24896–24906, 2016.

[11] M. J. Booth, M. A. A. Neil, R. Juškaitis, and T. Wilson, "Adaptive aberration correction in a confocal microscope," *PNAS*, vol. 99, no. 9, pp. 5788–5792, 2002.

[12] D. Débarre, E. J. Botcherby, M. J. Booth, and T. Wilson, "Adaptive optics for structured illumination microscopy," *Optics Express*, vol. 16, no. 13, pp. 9290–9305, 2008.

[13] N. Olivier, D. Débarre, and E. Beaurepaire, "Dynamic aberration correction for multiharmonic microscopy," *Optics Letters*, vol. 15, no. 20, pp. 3145–3147, 2009.

[14] D. Débarre, E. J. Botcherby, T. Watanabe, S. Srinivas, M. J. Booth, and T. Wilson, "Image-based adaptive optics for two-photon microscopy," *Optics Letters*, vol. 34, no. 16, pp. 2495–2497, 2009.

[15] P. Pozzi, C. Smith, E. Carroll, D. Wilding, O. Soloviev, M. Booth, G. Vdovin, and M. Verhaegen, "Anisoplanatic adaptive optics in parallelized laser scanningmicroscopy," *Optics Express*, vol. 28, no. 10, pp. 14222–14236, 2020.

[16] T. L. Liu, S. Upadhyayula, D. E. Milkie, V. Singh, K. Wang, I. A. Swinburne, K. R. Mosaliganti, Z. M. Collins, T. W. Hiscock, J. Shea, A. Q. Kohrman, T. N. Medwig, D. Dambournet, R. Forster, B. Cunniff, Y. Ruan, H. Yashiro, S. Scholpp, E. M. Meyerowitz, D. Hockemeyer, D. G. Drubin, B. L. Martin, D. Q. Matus, M. Koyama, S. G. Megason, T. Kirchhausen, and E. Betzig, "Observing the cell in its native state: Imaging subcellular dynamics in multicellular organisms," *Science*, vol. 360, no. 6386, pp. 284 –284, 2018.

[17] J. H. Park, L. Kong, Y. Zhou, and M. Cui, "Large-field-of-view imaging by multi-pupil adaptive optics," *Nature Methods*, vol. 14, no. 6, pp. 581–583, 2017.

[18] M. A. May, K. K. Kummer, M.-L. Edenhofer, J. L. Choconta, M. Kress, M. Ritsch-Marte, and A. Jesacher, "Simultaneous scattering compensation at multiple points in multi-photon microscopy," *Biomedical Optics Express*, vol. 12, no. 12, pp. 7377–7387, 2021.

[19] P. Pozzi, L. Maddalena, N. Ceffa, O. Soloviev, G. Vdovin, E. Carroll, and M. Verhaegen, "Fast Calculation of Computer Generated Holograms for 3D Photostimulation through Compressive-Sensing Gerchberg-Saxton Algorithm," *Methods and Protocols*, vol. 2, no. 1, pp. 2–15, 2018.

[20] L. N. Thibos, R. A. Applegate, J. T. Schwiegerling, and R. Webb, "Standards for reporting the optical aberrations of eyes," *Journal of Refractive Surgery*, vol. 18, no. 5, pp. 652–60, 2002.

[21] C. Rodríguez and N. Ji, "Adaptive optical microscopy for neurobiology," *Current Opinion in Neurobiology*, vol. 50, pp. 83–91, 2018.

[22] E. Papagiakoumou, E. Ronzitti, I. W. Chen, M. Gajowa, A. Picot, and V. Emiliani, "Two-photon optogenetics by computer-generated holography," in *Neuromethods*, vol. 133, pp. 175–197, Humana Press Inc., 2018.

[23] A. Thayil and M. J. Booth, "Self calibration of sensorless adaptive optical microscopes," *Journal of the European Optical Society*, vol. 6, p. 11045, 2011.

[24] P. Virtanen, R. Gommers, T. E. Oliphant, M. Haberland, T. Reddy, D. Cournapeau, E. Burovski, P. Peterson, W. Weckesser, J. Bright, S. J. van der Walt, M. Brett, J. Wilson, K. J. Millman, N. Mayorov, A. R. Nelson, E. Jones, R. Kern, E. Larson, C. J. Carey, I. Polat, Y. Feng, E. W. Moore, J. VanderPlas, D. Laxalde, J. Perktold, R. Cimrman, I. Henriksen, E. A. Quintero, C. R. Harris, A. M. Archibald, A. H. Ribeiro, F. Pedregosa, P. van Mulbregt, A. Vijaykumar, A. P. Bardelli, A. Rothberg, A. Hilboll, A. Kloeckner, A. Scopatz, A. Lee, A. Rokem, C. N. Woods, C. Fulton, C. Masson, C. Häggström, C. Fitzgerald, D. A. Nicholson, D. R. Hagen, D. V. Pasechnik, E. Olivetti, E. Martin, E. Wieser, F. Silva, F. Lenders, F. Wilhelm, G. Young, G. A. Price, G. L. Ingold, G. E. Allen, G. R. Lee, H. Audren, I. Probst, J. P. Dietrich, J. Silterra, J. T. Webber, J. Slavič, J. Nothman, J. Buchner, J. Kulick, J. L. Schönberger, J. V. de Miranda Cardoso, J. Reimer, J. Harrington, J. L. C. Rodríguez, J. Nunez-Iglesias, J. Kuczynski, K. Tritz, M. Thoma, M. Newville, M. Kümmerer, M. Bolingbroke, M. Tartre, M. Pak, N. J. Smith, N. Nowaczyk, N. Shebanov, O. Pavlyk, P. A. Brodtkorb, P. Lee, R. T. McGibbon, R. Feldbauer, S. Lewis, S. Tygier, S. Sievert, S. Vigna, S. Peterson, S. More, T. Pudlik, T. Oshima, T. J. Pingel, T. P. Robitaille, T. Spura, T. R. Jones, T. Cera, T. Leslie, T. Zito, T. Krauss, U. Upadhyay, Y. O. Halchenko, and Y. Vázquez-Baeza, "SciPy 1.0: fundamental algorithms for scientific computing in Python," *Nature Methods*, vol. 17, no. 3, pp. 261–272, 2020.

[25] R. M. White, A. Sessa, C. Burke, T. Bowman, J. Leblanc, C. Ceol, C. Bourque, M. Dovey, W. Goessling, C. E. Burns, and L. I. Zon, "Transparent adult zebrafish as a tool for in vivo transplantation analysis," *Cell Stem Cell*, vol. 2, no. 2, pp. 183–189, 2008.

[26] A. Facomprez, E. Beaurepaire, and D. Débarre, "Accuracy of correction in modal sensorless adaptive optics," *Optics Express*, vol. 20, no. 3, pp. 2598–2612, 2012.

[27] A. M. Petzold, V. M. Bedell, N. J. Boczek, J. J. Essner, D. Balciunas, K. J. Clark, and S. C. Ekker, "SCORE Imaging: Specimen in a Corrected Optical Rotational Enclosure," *Zebrafish*, vol. 7, no. 2, pp. 149–54, 2010.

[28] C. Bourgenot, C. D. Saunter, J. M. Taylor, J. M. Girkin, and G. D. Love, "3D adaptive optics in a light sheet microscope," *Optics Express*, vol. 20, no. 12, pp. 13252–13261, 2012.

[29] K. Wang, W. Sun, C.T. Richie, B.K. Harvey, E. Betzig, and N. Ji., "Direct wavefront sensing for high-resolution in vivo imaging in scattering tissue," *Nature Communications*, vol. 6, p. 7276, 2015.

[30] D. Ancora, T. Furieri, S. Bonora, and A. Bassi, "Spinning pupil aberration measurement for anisoplanatic deconvolution," *Optics Letters*, vol. 46, no. 12, pp. 2884–2887, 2021.

[31] T. Furieri, D. Ancora, G. Calisesi, S. Morara, A. Bassi, and S. Bonora, "Aberration measurement and correction on a large field of view in fluorescence microscopy," *Biomedical Optics Express*, vol. 13, no. 1, pp. 262–273, 2022.

[32] Q. Hu, J. Wang, J. Antonello, M. Hailstone, M. Wincott, R. Turcotte, D. Gala, and M. J. Booth, "A universal framework for microscope sensorless adaptive optics: Generalized aberration representations," *APL Photonics*, vol. 5, no. 10, p. 100801, 2020.

[33] M. A. May, N. Barré, K. K. Kummer, M. Kress, M. Ritsch-Marte, and A. Jesacher, "Fast holographic scattering compensation for deep tissue biological imaging," *Nature Communications*, vol. 12, no. 1, p. 4340, 2021.

[34] A. Picot, S. Dominguez, C. Liu, I. W. Chen, D. Tanese, E. Ronzitti, P. Berto, E. Papagiakoumou, D. Oron, G. Tessier, B. C. Forget, and V. Emiliani, "Temperature Rise under Two-Photon Optogenetic Brain Stimulation," *Cell Reports*, vol. 24, no. 5, pp. 1243–1253, 2018.

[35] P. Pozzi and J. Mapelli, "Real Time Generation of Three Dimensional Patterns for Multiphoton Stimulation," *Frontiers in Cellular Neuroscience*, vol. 15, p. 1609505, 2021.

[36] M. Hossein Eybposh, N. W. Caira, M. Atisa, P. Chakravarthula, and N. C. Pégard, "DeepCGH: 3D computer-generated holography using deep learning," *Optics Express*, vol. 28, no. 18, p. 26636, 2020.

[37] H. R. G. W. Verstraete, S. Wahls, J. Kalkman, and M. Verhaegen, "Model-based sensor-less wavefront aberration correction in optical coherence tomography," *Optics Letters*, vol. 40, no. 24, pp. 5722–5725, 2015.

[38] D. Debarre, M. J. Booth, and T. Wilson, "Image based adaptive optics through optimisation of low spatial frequencies," *Optics Express*, vol. 15, no. 13, pp. 8176–8190, 2007.

[39] B. Talone, P. Pozzi, M. Cavagnini, D. Polli, G. Pozzi, and J. Mapelli, "Experimental determination of shift-less aberration bases for sensorless adaptive optics in nonlinear microscopy," *Optics Express*, vol. 29, no. 23, pp. 37617–37627, 2021.

4.A. Appendix

4.A.1. Aliasing as limiting factor to correct aberrations in computer generated holography

Limitations to the applicable patterns occur when the pixel density of the spatial light modulator (SLM) does not provide sufficient sampling for the hologram. Since the phase in the SLM projection is wrapped with values between 0 and 2π delay, errors arise when the local gradient of the hologram is greater, in absolute value, than the ratio $\frac{\pi}{pixel}$. When this condition is satisfied the lack of SLM sampling generates a local gradient different than the one required to compute the desired hologram. This phenomenon is called aliasing.

Aliasing can cause loss of signal and resolution as well as the appearance of undesired focal spots in the projected pattern. When displacing spots in both lateral and axial directions, or applying an aberration to a displaced spot, the gradients of the displacement and aberrations patterns are added together. In such situations aliasing may appear faster. Therefore, the usable lateral field of view (FOV) decreases as axial displacement increases, and spots at the edges of the FOV have less available "stroke" to correct aberrations. Figure A1(a) shows the effect of aliasing for points distributed at different horizontal positions in the lateral FOV. Here, aliasing arises when we apply 100 μm horizontal coma (Z_7) coefficient to the computer generated hologram (CGH).

When a single point belonging to multi-spot CGH is aliased this effect does not perturb all the others. In fact, multi-spot CGH are calculated as interference patterns of individual CGH encoding for single points. Moreover, aliasing is only present if the phase pattern generating one of the points is aliased. Adding other points neither solves, nor worsens the effect of aliasing. This behaviour is shown in Fig. A1(b) where we compare the image of a CGH encoding for 21 points with the image of the same CGH with 100 μm horizontal coma (Z_7) on one point. In the second case, only the aliased point shows loss of intensity and fidelity and it does not compromise the quality of the other spots.

Since aliased areas of the hologram generally show smooth phase variations, they can generate relatively low aperture spots in undesired positions in the sample, with the possibility of photostimulating additional region of interest (ROI). It is therefore recommended, especially when generating an hologram with aberration correction, to compute the hologram gradients. To deviate all the light in the aliased areas to the zero order block and avoid off-target stimulation, it is possible to mask the aliased areas with a constant phase value.

4.A.2. Aberration characterization on synthetic sample along vertical and horizontal direction

To fully characterize the local variation of aberrations along the horizontal and vertical direction of a synthetic sample. For this purpose we projected in a fluorinated ethylene propylen (FEP) tube filled with fluorescein an horizontal and a vertical line of points. In both configurations we have eight points covering a FOV of 150 μm along respectively vertical and horizontal directions, the distance between each

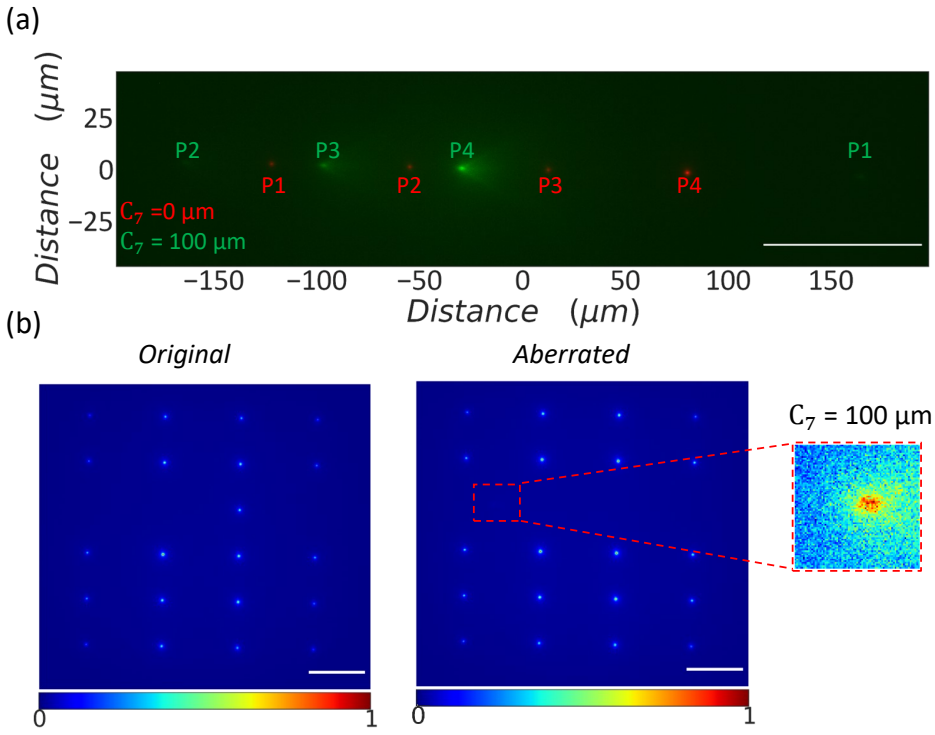

Figure A1: **Effect of aliasing on CGH**. (a) Two-photon excited fluorescence (TPEF) induced by 4-points CGH projected onto a Rhodamine slide. Red spots show the TPEF induced by aberration-free points (0 μm horizontal coma coefficient), whereas green spots are affected by 100 μm horizontal coma coefficient. Here, spots at the edges of the FOV have much lower intensity compared to the points in the middle. The effect of aliasing on points at the edges of the FOV is more prominent. Scale bar: 15 μm (b) Left: TPEF induced onto a Rhodamine slide by 21- points grid hologram. Right: TPEF induced by same pattern with 100 μm horizontal coma coefficient for the highlighted point. The additional coma phase degrades both shape and intensity of the interested point whereas the others are not affected. Both images are normalized with respect to themselves while the intensity of the area in the inset was not normalized and it was enhanced by a constant factor of 100. Scale bars: 50 μm

point with its nearest neighbour is alternatively 15 μm and 30 μm. Figure A2(a) and (d) show the TPEF image of each pattern before (left) and after (right) correction. The raw images were corrected with the anisoplanatic approach up to the fourth aberration order, corresponding to Zernike polynomials in the interval Z_3–Z_{14}. For each mode we tested 15 bias coefficients in the interval [-1.5,1.5] μm except for both oblique (Z_3) and vertical (Z_5) astigmatism where the bias coefficients spanned over a bigger range [-3,3] μm. For all the modes we found the best coefficient by maximizing the intensity-diameter combined metric M_1. As depicted in Fig.A2(b) the anisoplanatic phase maps for the vertical line of points appear rotated in opposite directions for the ROIs laying at the edges of the line. This effect is due to the oblique astigmatism coefficient which changes from positive to negative val-

ues moving down the line. This effect is confirmed by the local bar plots of the retrieved corrections in Fig.A2(c). A similar trend was observed for the horizontal line where the oblique astigmatism changes from negative to zero and then back to negative values moving along the line left to right as shown in Fig.A2(e)-(f). Moreover, for both the vertical and the horizontal lines, oblique and vertical astigmatism are the most prominent aberrations and they are more pronounced at the edges of respectively vertical and horizontal FOVs. This is most likely due to the curvature of the FEP tube and it gives a good overview of the local variation of lower order aberrations in this sample.

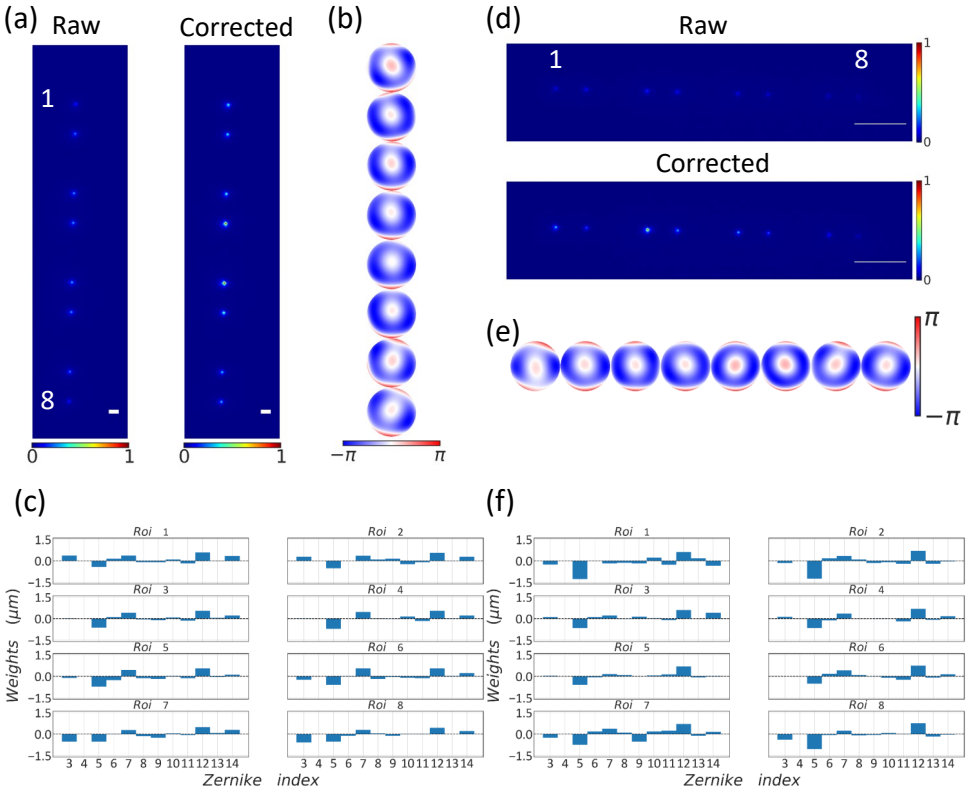

Figure A2: **Aberration characterization on synthetic sample along vertical and horizontal direction**. (a) TPEF images of 8 points with alternate spacing 15 and 30 μm extending over a vertical FOV of 150 μm. Left: raw image. Right: corrected image up to fourth order aberration (Z_3–Z_{14}). Scale bar: 5 μm. (b) Anisoplanatic correction phase maps at each ROI along the vertical line. (c) Bar plot of Zernike coefficients for each ROI in the vertical line. d) TPEF images of 8 points with alternate spacing 15 and 30 μm extending over a horizontal FOV of 150 μm. Left: raw image. Right: corrected image up to fourth order aberration (Z_3–Z_{14}). Scale bar 25 μm. (e) Anisoplanatic correction phase maps at each ROI along the horizontal line. f) Bar plot of Zernike coefficients for each ROI in the horizontal line.

4.A.3. Effect of spatial proximity between ROIs

The spatial variation of aberrations is an important property of the sample. We saw that in a fairly uniform fluorescent sample, such as the FEP tube filled with fluorescein, a lateral sampling of 25 μm was enough to characterize the aberrations induced by the system and to successfully apply the corrections to another pattern in the same FOV. In a more turbid sample, aberrations may change over smaller length scale (corresponding to a smaller isoplanatic patch size) and require adaptive optics (AO)characterization at more closely-spaced ROIs in order to correct for an arbitrary CGH. Because points near together in object space are produced by similar positional phase holograms $\phi_{POS,n}$, we reasoned that the limited bit-depth of the SLM would result in cross-talk between anisoplanatic AO corrections for nearby points.

Next we asked how the distance between ROIs influences the independence of AO corrections in the composite CGH. To test this aspect, we projected into our synthetic sample a CGH with ROIs spaced closely together. The TPEF image of this pattern is reported in Fig. A3(a), left. The paired ROIs have intra-pair distances of 12, 9 and 6 μm respectively, and they are vertically distributed along the cylindrical axis of the FEP tube to minimize the sample-induced aberrations between ROIs. Additionally the pattern includes a third column of points placed at a greater distance (30 μm) to monitor the quality of AO. Additional astigmatism (Z_3) with a coefficient $w = -2\mu$m is applied on the right-most column, labeled R in Fig. A3(a), left. This extra aberration is seen in Fig. A3(b) where the phase maps referring to the most right column appear rotated, but had little effect on the intensity of the TPEF of these points.

Anisoplanatic correction up to the fifth aberration order, corresponding to modes Z_3–Z_{20}, was performed using the metric M_2. Figure A3(a), right shows the pattern after correction. The comparison between the line profiles of aberrated (orange) and corrected (blue) ROIs (Fig. A3(d)) reveals an average intensity improvement of a factor 3.76 ± 0.84 , independently of the proximity between pairs of points.

Analysis of the recovered Zernike coefficients (Fig. A3(c)) shows the effect of spatial proximity. In each bar plot, the blue bars show the difference between corrections recovered for the right and the left points. The correction found for the left point represents the baseline aberration while the corrections for the right point should reveal the computationally-introduced astigmatism. As expected, the coefficients recovered for the points in the left and right columns are similar for most orders, resulting in $\Delta w \approx 0\mu$m, with the exception of Z_3. For Z_3, the recovered coefficient is close to the expected value of 2 μm for all pairs of ROIs, but progressively decreases as the distance between the points decreases from 12 μm to 6μm (Fig A3(c), top to bottom). The difference in astigmatism recovered at the pair of ROIs with closer distance is lower than expected ($\Delta w = 1.83 \pm 0.25\mu$m). The error bars on the corrective coefficient (in black) are calculated from the uncertainty in the parameters of the Lorentzian fit to metric M_2.

The same experiment was repeated several times, also with different patterns and the same observations were drawn. We can conclude that The cross-talk among corrections of ROIs close together ($\leq$ 9 μm) does not necessarily impair the final

degree of intensity improvement of TPEF from the points, but that the corrective CGHs for ROIs in close proximity are not independent. As reported in [1] living tissues are more complex than fixed tissue and hence the area where the local correction is valid is ten-fold smaller, on the order of 3 μm. In such samples the constraint on the proximity of the ROIs to correct becomes a limitation to consider.

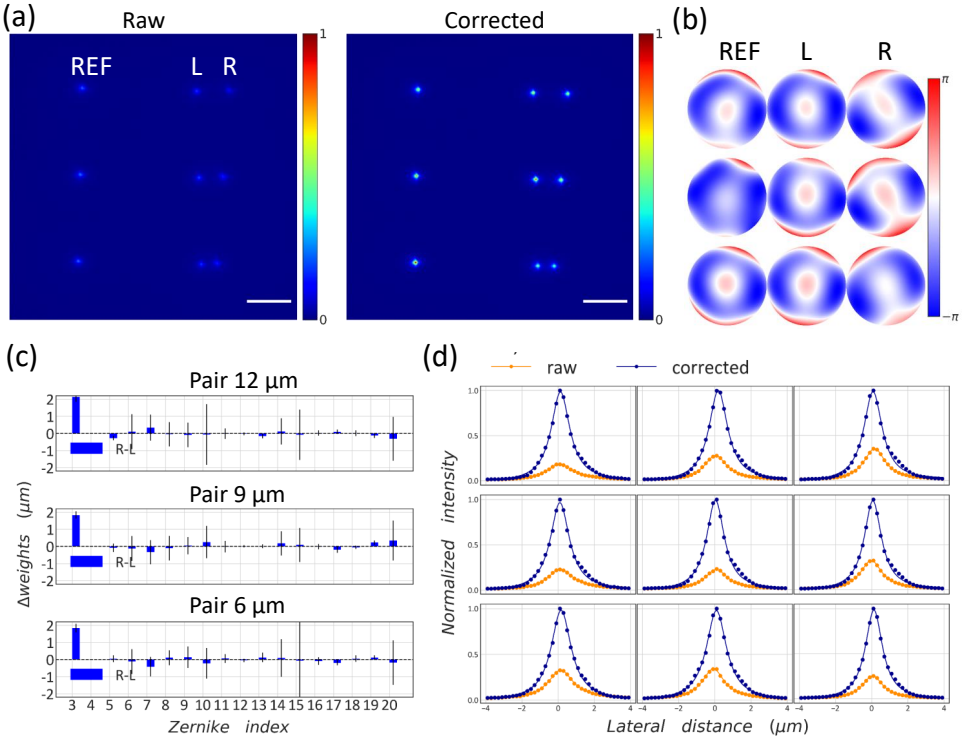

Figure A3: Effect of ROIs proximity on the anisoplanatic correction. (a) Left: Aberrated image, the most right column, labelled with R, is affected by oblique astigmatism Z_3 with a weight of -2μm. Right: Corrected image. Scale bar: 15 μm (b) Phase maps retrieved after correction. (c) Difference between correction coefficient on the three pairs of ROIs. Top, middle and bottom plots refer respectively to pair at distance 12μm, 9μm and 6μm. Bars represent the uncertainty on the corrective coefficients. (d) Line profiles comparison between aberrated (orange dots) and corrected (blue dots) ROIs. Continuous lines show Lorentzian fit on the data points.

4.A.4. Anisoplanatic correction on fixed zebrafish tissue in FEP tube

When the anisoplanatic approach was applied to both the FEP tube and to the same sample holder containing the fixed zebrafish embryo we assessed the efficiency of the sequential search of the optimal Zernike correction. This was accomplished by plotting the value of the normalized metric M_1 as function of each iteration in the optimization process. For an efficient search algorithm we expect quick rise that converges to the maximum value of the metric. Conversely the hill-climbing algorithm shows oscillations between low (nearly zero) and high (nearly 1) values of the normalized metric (Fig. A4). Hence, most of the Zernike coefficients explored in the hill-climbing search yielded low metric values making this search algorithm inefficient.

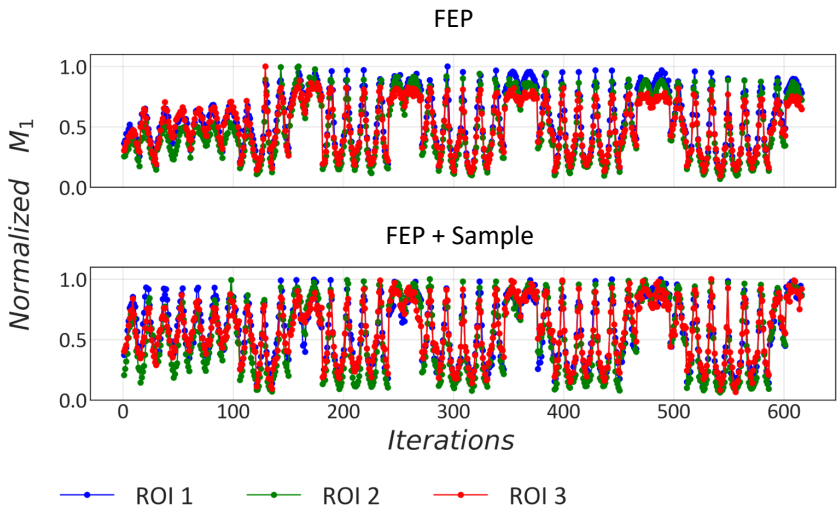

Figure A4: **Intensity-diameter combined metric M_1 as function of iterations in the optimization proces** Blue, green, red dots refer to the metric M_1 value measured at each ROIs as function of the iteration. Each iteration corresponds to a single coefficient for a single Zernike polynomial applied to the SLM. Top: Correction in FEP tube. Bottom: correction for tissue after the FEP-induced aberrations compensation.

The anisoplanatic correction on the FEP tube containing a fixed zebrafish embryo was also performed using a single-step approach. The preliminary correction on the sample holder was skipped and the anisoplanatic AO method was applied directly on the FEP tube with the sample. A CGH was projected through about 140 μm of tissue in the tail of a 5 dpf zebrafish embryo embedded in a mixture of 1.5% low-melting temperature agarose and fluorescein. As shown in Fig.A5(a), top the CGH is composed of three points extending over a over a lateral FOV of 115 μm. Each point hits different anatomical locations of the tail. The lateral points go through

muscles areas whereas the middle point is projected through the notochord. The TPEF signal coming from the fluorophore behind the tissue is degraded as shown in Fig.A5(a), middle. The middle point is brighter compared to the lateral ones revealing the inhomogeneity of the tissue. Figure A5(a), bottom shows the image after anisoplanatic correction. In this case the correction was performed in a single-step for both FEP and tissue-induced aberrations. We corrected up to the eighth aberration order, corresponding to Zernike polynomials in the interval Z_3–Z_{44} and we used the intensity-diameter combined metric M_1.

The resulting corrective phase maps are depicted in Fig.A5(b). Figure A5(c) offers a closer look on the individual ROIs before (top row) and after (bottom row) correction. It is clear that the correction improves the intensity of all the ROIs, as shown in the intensity profiles (see Fig. A5(d)). The intensity enhancement was about a factor of 1.56 for the lateral ROIs and 1.65 for the central point. Hence, we can conclude that the single-step correction for FEP and tissue-induced aberration is less effective than the two-step correction shown in Fig. 4.6. In this case the middle and the lateral points had an intensity enhancement of a factor of 3.44 and 2.83 respectively. The improvement of the metric M_1 as function of the Zernike index optimized in Fig.A5(e) reveals a behavior similar to the correction for FEP-induced aberration. After the first 12 Zernike polynomials we register an improvement of 2-fold on the metric value and then a plateau is reached. This observation confirms that the compensation for FEP-induced distortions has a decisive impact also in the single-step correction approach. The bar plot of the Zernike coefficients in Fig.A5(f) show the same prominent aberrations (vertical astigmatism Z_5,Z_{27}, Z_{35} and Z_{36}) observed in the case of the two-step correction (see Fig.4.6(e)).

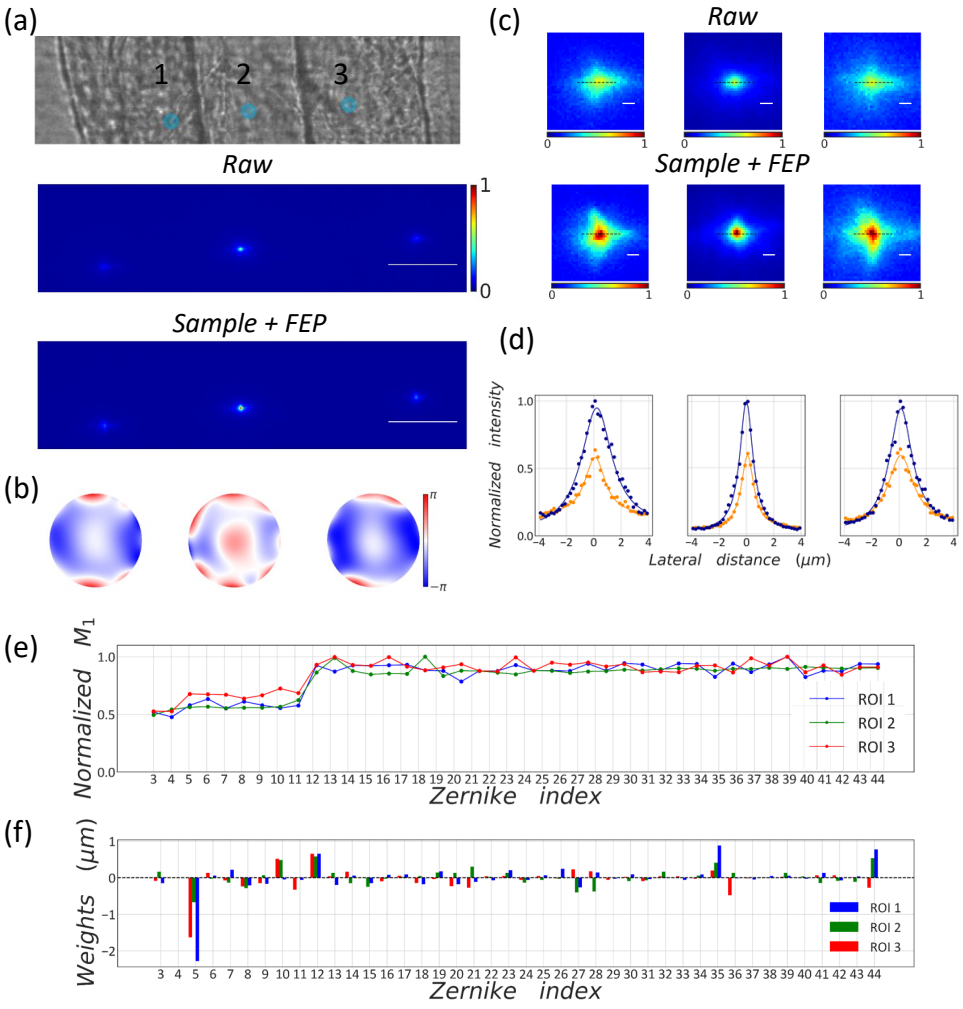

Figure A5: **Single-step anisoplanatic correction on fixed zebrafish tissue in FEP tube** (a) Top: Bright field image of the tail of the embryo tail (lateral view) showing the location of the targeted ROIs in cyan extending over a lateral FOV of 115x4 μm. Middle: xy images of the CGH projected into the embryo tail. Bottom: xy image of the CGH projected into the embryo tail corrected with anisoplanatic approach for FEP and tissue-induced aberrations. Scale bars: 25 μm. (b) Corrective phase maps for each point. (c) Zoom in of xy images of the ROIs. Top: Aberrated case. Bottom: corrected for FEP and tissue in one-shot. Scale bars: 1 μm. (d) xy line profiles across the dashed lines in (c). Blue dots: corrected, orange dots: aberrated, continuous lines: Lorentzian fit on the data points. (e) Normalized metric M_1 value as function of the Zernike correction. (f) Bar plot of Zernike coefficients for each ROI corrected for the FEP tube and tissue in one-shot.

4.A.5. Effect of photobleaching on anisoplanatic correction in fixed zebrafish embryo expressing pan-neuronal GCaMP6f

The anisoplanatic correction is applied here to correct a CGH projected into a fixed 3 dpf zebrafish embryo expressing GCaMP6f [2] in the cytosol of the neurons. The zebrafish embryo was fixed in a 1:1 solution of embryo water (DI water with Instant Ocean salt (60 μg/ml) with 0.0002% methylene blue) and 4% paraformaldehyde in phosphate saline buffer (PBS) for 2 hours, rinsed 3x5 minutes in PBS, and stored in PBS at 4° C until the experiment. For the experiment the fish was mounted into a FEP tube with 1.5 % low-melting agarose in embryo medium. The zebrafish embryo was obtained by breeding adult zebrafish from the Casper strain [3] with Tg(elavl3:GCaMP6f) nacre adults. Hence, we could acquire fluorescence images of the brain through the light sheet microscope coupled to our 2P-CGH module shown in Fig. A6(a). The GCaMP6f fluorescence signal is excited by a diode-pumped solid-state (DPSS) laser emitting 488 nm light. An image of the zebrafish optic tectum is reported in Figure A6(b),top where we can distinguish individual neurons, the cyan circles highlight the target ROIs for our holographic stimulation.

Figure A6(b) shows the TPEF image of CGH projected before (middle) and after (bottom) anisoplanatic correction. The anisoplanatic correction was performed up to the fifth aberration order (Z_3–Z_{21}) testing fifteen bias coefficient for each Zernike mode in the interval [-3,3] μm and using the intensity-diameter metric M_1. As we can observe comparing raw and corrected images in Fig. A6(b), the intensity of signal is diminished after correction, this is also confirmed by the plot of the normalized metric M_1 and normalized maximum intensity at each ROI as function of the Zernike correction (Fig. A6(d)). The progressive decrease of the maximum intensity and metric value during the correction procedure is due to the bleaching of the GCaMP6f signal. During the correction the exposure of the sample to the NIR stimulation light was minimized by gating the light with the mechanical shutter whenever we were not acquiring images. Moreover, we modified the value of the threshold applied to measure the ROIs diameter. For a low-signal to noise image the usual threshold ($\frac{1}{e} \cdot I_{max}$ would rapidly decrease below the minimum intensity value and this would hinder binarization of the image. In order to overcome this issue we modified the threshold value as follows: $\frac{1}{e} \cdot (I_{max} - I_{min}) + I_{min}$). However, those measures could not prevent the decrease of the TPEF intensity over time due to bleaching. Hence, we can conclude that to correct for aberration on samples where the fluorescent signal comes from a limited pool of protein *in vivo* either a faster optimization scheme is needed or we need to retrieve the correction on guide star fluorophores injected in the sample and then apply those corrections using the average distance -weighted correction.

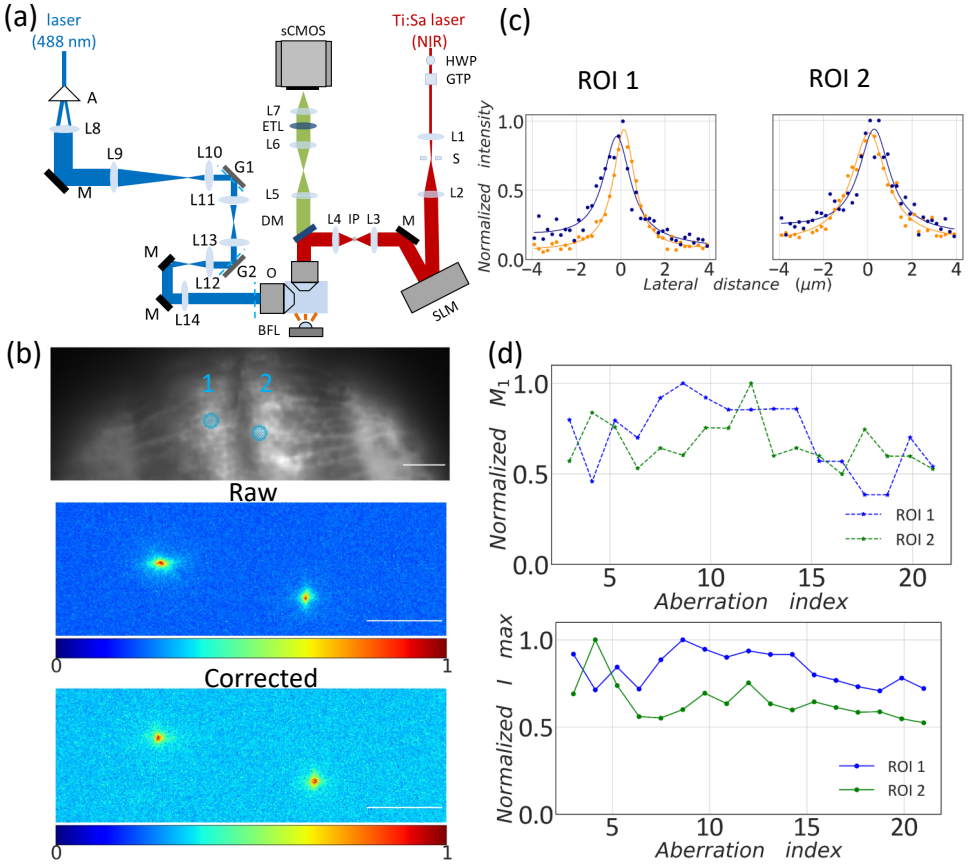

Figure A6: **Effect of photobleaching on anisoplanatic correction in fixed zebrafish embryo expressing pan-neuronal GCaMP6f.** (a) Layout of the 2P-CGH module (red path) coupled to a light sheet microscope (blue path). Figure not to scale. (b) Top: Light-sheet image of the optic tectum of a 3 dpf zebrafish embryo expressing cytosolic GCaMP6f pan-neuronally. Cyan circles show the target location for the CGH. Scale bars: 25 μm. Middle: xy TPEF image of the CGH projected into the embryo brain. Bottom: xy TPEF image of the CGH projected into the embryo brain after anisoplanatic correction. Scale bar: 15 μm. (c) xy line profiles across the pixel of maximum intensity at each ROI. Blue dots: corrected, orange dots: aberrated, continuous lines: Lorentzian fit on the data points. (d) Top: Normalized metric M_1 value as function of the Zernike correction. Bottom: normalized maximum intensity value as function of the Zernike correction.

References

[1] M. A. May, K. K. Kummer, M.-L. Edenhofer, J. L. Choconta, M. Kress, M. Ritsch-Marte, and A. Jesacher, "Simultaneous scattering compensation at multiple points in multi-photon microscopy," *Biomedical Optics Express*, vol. 12, no. 12, pp. 7377–7387, 2021.

[2] Junichi Nakai, Masamichi Ohkura, and Keiji Imoto, "A high signal-to-noise Ca2+ probe composed of a single green fluorescent protein," *Nature biotechnology*, vol. 19, pp. 137–141, 2001.

[3] R. M. White, A. Sessa, C. Burke, T. Bowman, J. Leblanc, C. Ceol, C. Bourque, M. Dovey, W. Goessling, C. E. Burns, and L. I. Zon, "Transparent adult zebrafish as a tool for in vivo transplantation analysis," *Cell Stem Cell*, vol. 2, no. 2, pp. 183–189, 2008.

5

Flexible control of pulse intensity and repetition rate for multiphoton photostimulation

In deep tissue imaging, pulsed near-infrared lasers commonly provide high peak powers needed for nonlinear absorption, but average power and linear absorption can be limiting factors for tissue damage through heat. We implemented intra-cavity dumping within a mode-locked Ti:Sapphire laser used for two-photon computer generated holography stimulation. This system enables photostimulation in which pulse energy, average power, and repetition rate can each be varied and harnessed as degrees of freedom. We demonstrate how this system provides a new dimension of temporal control in photostimulation experiments to alter the ratio of nonlinear to linear light-tissue interactions, namely by tuning the laser repetition rate between single-shot and ≈ 3 MHz. Repetition rates below 1 MHz, yielding pulse energies over 60 nJ, facilitated holographic projections with more regions of interest than the highest repetition rate of 3 MHz. Even lower repetition rates (≈10 kHz) diminished thermal load on the sample, as characterized by quantification of heat shock protein expression in zebrafish tissue.

This chapter is based on the work: *Flexible control of pulse intensity and repetition rate for multiphoton photostimulation.* Frontiers in Physics **10**(1005094),(2022)

5.1. Introduction

Optogenetics and photopharmacology are excellent tools to perturb and monitor cells in living animals to understand their specific function within complex neural circuits [1, 2]. Since their advent thirty years ago, many advancements on the sensor engineering and on the light-delivery methods have been made. Thanks to this progress it is currently possible to stimulate and monitor neuronal activity in living animals with single-cell precision and millisecond time resolution in three dimensions [3, 4]. Nonlinear photostimulation requires high peak power to elicit the activation of the optogenetic actuator. The number of photons absorbed per second is proportional to the two-photon (2P) absorption cross-section as well as the squared light intensity. The 2P absorption cross-section, measured in Goeppert-Mayer (GM) units, is typically many orders of magnitude smaller than one-photon (1P) cross-sections. For instance, Channelrhodopsin-2 has a relatively high 2P absorption cross-section of 260 GM at 920 nm [5] (1 GM = $10^{-50} cm^4 \cdot s/photon$), whereas typical 1P cross-sections range in the interval 10^{-15}–$10^{-17} cm^2$ [**?**]. As a consequence, linear absorption of near-infrared (NIR) light by highly prevalent molecular species like water (1P cross-section of approximately $2.25 \cdot 10^{-24} cm^2$ at 920 nm [6]) can be significant compared to the nonlinear absorption in photostimulation experiments.

Phototoxicity during multiphoton NIR excitation may result from two different scenarios occurring at different scales in biological tissues: local effects associated with nonlinear excitation and global effects induced by 1P absorption of NIR. Nonlinear effects are instantaneous and can be destructive due to multi-photon ionization, cell ablation, optical breakdown and even plasma formation [7]. Nonlinear absorption can also cause photochemical damage [8], such as DNA damage or formation of reactive oxygen species (ROS). Although wavelengths typically used for imaging and photostimulation lay in the so-called ”optical window for tissues”, linear absorption by endogenous molecules such as water contribute to sample heating [8]. The global effects of thermal damage occur at a slower time scale. Even slight heating can cause an alteration of the sample physiology such as instability of synaptic responses [9] or modulation of the firing rate [10]. Ultimately if the temperature increase is on the order of 8 °C, cell death due to protein denaturation is a possible consequence [11]. Picot and colleagues [12] studied extensively the temperature rise consequent to 2P optogenetics stimulation. The sample thermal load was both simulated in optically scattering samples and directly measured in living mouse exposed to different 2P photostimulation patterns. Thermal damages effects were also characterized in the context of multiphoton microscopy [13, 14].

This competing aspect of linear and nonlinear absorption is particularly important when parallel stimulation techniques (e.g. computer generated holography, CGH) are used. In parallel stimulation schemes the available power is divided among multiple target regions of interest (ROIs) [15], requiring high cross-section actuators and high laser peak powers. However, when these conditions are satisfied, the major limitation to the number of neurons that can be irradiated concurrently is light-induced tissue damage [16].

In this study, we investigate how short-pulse photostimulation parameters af-

fect tissue damage in the context of 2P stimulation with NIR light shaped with computer generated holography (2P-CGH). This technique is typically applied for optogenetic manipulations *in vivo* to study neural circuits. Long-duration experiments and repeated irradiation of multiple ROIs with long exposures (milliseconds to seconds) [12] are required to probe neural activity over time. To investigate the light-tissue interaction as function of the pulsed light parameters such as repetition rate, average power and pulse energy, we used a Ti:Sapphire mode-locked laser equipped with an intra-cavity dumping system based on acousto-optical modulation of the intra-cavity gain. The cavity dumper technology allows the user to flexibly reduce the laser repetition rate while at the same time increasing the pulse energy. Other methods are available to reduce the laser repetition rate, such as increasing the cavity length, are not practical to change "on the fly". Alternatively, a pulse picker [17] operating outside the cavity tends to decrease pulse energy through extra losses [18].

We evaluated the performance of the intra-cavity dumping laser shaped with CGH by measuring two-photon excited fluorescence (TPEF) in both synthetic samples and living zebrafish embryos. From literature [12, 17, 18] it is known that a reduced repetition rate decreases the thermal load generated by the pulses on the tissue. Hence, we hypothesized that lower repetition rates may mitigate the thermal damage induced by NIR light. This was verified by measuring the expression level of heat shock protein 70 (Hsp70), a histological marker of thermal damage, in the zebrafish embryos after laser irradiation at different repetition rates. We found that prolonged exposure to NIR light at a high laser repetition rate led to upregulation of Hsp70 expression, while this thermal damage was mitigated by a 300-fold lower repetition rate.

5.2. Materials and Methods

5.2.1. 2P-CGH module with scanning light sheet microscope

The optical setup shown in Figure 5.1(a) combines the 2P-CGH module for 2P photostimulation with a digitally scanned light sheet microscope. The light sheet microscope uses a Bessel beam excitation profile. The 488 nm excitation laser (DPSS, OBIS-488-LS, Coherent) is shaped as a hollow cylinder by the combination of an axicon (A) and a plano-convex lens (L8). The collimated ring is then conjugated with two scanning galvanometer mirrors (G1, G2, ax1210-A, Thorlabs) at the rear aperture of the excitation objective (E0, 10X/NA 0.3 CFI Plan Fluorite, Nikon). Fluorescence is collected through the detection objective (DO, 20X/NA 1.0 XLUMPLFLN, Olympus) after it passes through a low-pass dichroic mirror (DM, FF01-720/SP-25, Semrock). Finally an image is formed by a tube lens (L5, f= 300 mm) and relayed onto the sCMOS camera (Zyla 4.2, Andor) via a 1:1 telescope (L6 and L7, focal 150 mm). An electrically-tunable lens (ETL, EL-16-40-TC-VIS-20D, Optotune), positioned in the common focus of the telescope, is synchronized to the motion of G2 to enable imaging at different depths in the sample. Brightfield (BF) images are acquired by transmission of a white light LED (BFL, LEDW25E, Thorlabs) placed opposite to the detection objective.

The detection arm is shared between the microscope and the 2P-CGH photostimulation module. Here, a mode-locked Ti:Sapphire laser (Mira 900-F, Coherent) equipped with the the intra-cavity dumping system (pulseSwitch, APE) is pumped at 5 W with a continuous-wave laser (Verdi 10, Coherent). The output 800 nm light passes a combination of a half-wave plate (HWP, AHWP05M-980, Thorlabs) and a Glan-Laser calcite polarizer (GLP, GL5-B, Thorlabs) to control the average power, altered by changing the angle between the optical axis of the half-wave plate and polarizer. The beam, magnified by a telescope (lenses L1, f=25.4 mm and L2, f=150 mm) impinges on the chip of a liquid crystal on silicon spatial light modulator (SLM, P1920-600-1300-HDMI, pixel size: $9.2\mu m$, Meadowlark Optics) located in a plane where the incident light is collimated. The SLM is illuminated obliquely with an angle of 4.6° to be able to separate the modulated beam from the incident one. The NIR illumination is temporally gated with a response of 1 ms by a mechanical shutter (S, LS2S2Z1, Uniblitz), installed at the focal point of lens L1. A second telescope (lenses L3, f=250 mm and L4, f=500 mm) ensures that the beam fills the back aperture of the DO. An inverse pinhole (IP, custom tungsten deposition, diameter 1.3 mm, on glass window of thickness 0.5 mm), placed in the focal plane of lens L3, blocks the zero-order diffraction spot.

5.2.2. Cavity dumping technology

As shown in Figure 5.1(b), the intra-cavity beam enters a Bragg cell (B) driven with an acoustic signal, which causes a change in the refraction index of the crystal and hence diffraction of the incident light. This mechanism permits selection of specific pulses within the pulse train to be deflected as the output of the whole laser system. The acoustic wave is generated by an electrical radio-frequency (RF) signal applied through a transducer cemented at the base of the crystal. Compared to a standard Ti:Sapphire laser cavity, where the end mirror is an output coupler with roughly 20% transmission, here the end mirror is a high reflective mirror. This causes decreased losses and a consequent increase of intra-cavity energy that is dumped at specific times to form the output beam. The cavity dumping design here employed is double passed through the acousto-optic crystal and the output beam is the sum of the diffracted part interfering with the undiffracted one. By tuning the phase and the frequency of the RF signal we can get constructive interference and maximize the intensity of the output beam. This design allows to enhance the diffraction efficiency of the whole process as demonstrated in the following derivation of the dumped output beam.

The electrical field describing the intra-cavity optical beam is:

$$E(t) = E_0 cos(\omega t) \tag{5.1}$$

where ω is the laser carrier frequency and E_0 is the time dependent envelope. After the first pass through the Bragg cell, the electric fields denoting the diffracted and undiffracted beams are given by:

$$E_d = \sqrt{\eta} E_0 cos(\omega t + \Omega t + \phi) \tag{5.2}$$

$$E_u = \sqrt{(1-\eta)} E_0 cos(\omega t) \tag{5.3}$$

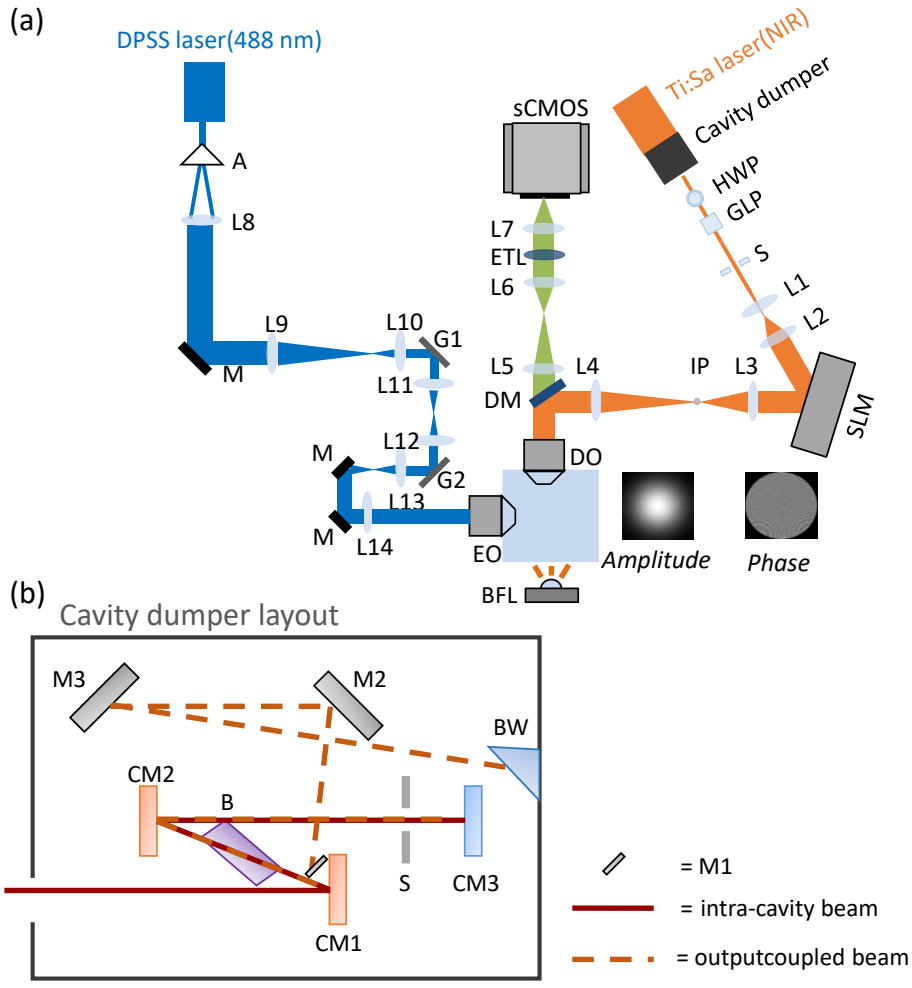

Figure 5.1: **Optical setup.** (a) Optical layout of the 2P-CGH module coupled to a light sheet microscope. Blue path: light sheet microscope; orange path: 2P-CGH module; green path: common fluorescence detection path. Not to scale. (b) Cavity dumping layout, not to scale. Red line: intra-cavity beam, dashed orange line: dumped beam. The intra-cavity beam is focused by the focusing mirror (CM1) into the Bragg cell (B) placed at Brewster's angle. The RF pulse applied to the Bragg cell deflects part of the beam in the first order of diffraction (dashed orange line). Both undiffracted and diffracted beam are collimated again by the collimating mirror (CM2) and retroreflected by the end mirror (CM3), passing through the slit (S). Then, both beams pass the Bragg cell a second time. The undiffracted part of the beam is retroreflected into the Ti:Sapphire cavity while the diffracted portion is reflected by mirror M1 towards mirrors M2 and M3. Finally the selected pulse leaves the cavity through the Brewster window (BW).

E_d is the electric field describing the diffracted beam which has been shifted in

frequency by the RF frequency Ω and it has an adjustable phase ϕ. E_u is the electric field associated with the undiffracted beam. In both equations η represents the efficiency of the diffraction process. After the second pass through the Bragg cell those beams interact once more with the acoustic wave, some of the diffracted beam will be undiffracted and part of the undiffracted beam will be diffracted. Hence the output dumped beam will be the sum of those contributions as follows:

$$\begin{aligned} E_{out}(t) = \sqrt{\eta}\sqrt{(1-\eta)}E_0 cos(\omega t + \Omega t + \phi) + \sqrt{(1-\eta)}\sqrt{\eta}E_0 cos(\omega t - \Omega t - \phi) = \\ \sqrt{\eta}\sqrt{(1-\eta)}E_0[cos(\omega t + \Omega t + \phi) + cos(\omega t - \Omega t - \phi)] = \\ \sqrt{\eta}\sqrt{(1-\eta)}E_{in} cos(\Omega t + \phi) \end{aligned} \tag{5.4}$$

The intensity of the output beam is given by :

$$I_{out} = 4\eta(1-\eta)|E_{in}|^2 cos^2(\Omega t + \phi) \tag{5.5}$$

The timing between the acoustic burst applied to the Bragg crystal and the intra-cavity optical pulse train traveling through the crystal is carefully tuned to maximize the energy of the dumped pulse. Specifically, the dumped intensity is highly sensitive to the phase ϕ of the RF signal.

5.2.3. Sample preparation

In this paper both synthetic and living samples were used. The synthetic sample was a diluted solution of fluorescein (F 100, Invitrogen) dissolved in demineralized water. The colour of the solution was vibrant dark yellow with an optical density of 0.056 in 0.8 mm path length measured through a spectrometer (μLITE, BioDrop).

Zebrafish embryos were obtained by inbreeding Tg(elavl3:GCaMP6f) adults [19]. Adult zebrafish were maintained under standard conditions in accordance with the EU directive 2014/63. Larvae were kept in embryo water (DI water with 60 μg/ml Instant Ocean salt and 0.0002% methylene blue) at 28°C until the experiment. The *in vivo* ablation experiments were carried out at 4 days past fertilization (dpf) while the *in vivo* laser irradiation experiments followed by western blot were conducted at 3 dpf. Before the *in vivo* ablation experiments embryos were anesthetized with 0.03 % tricaine (E10521, Sigma-Aldrich) in embryo water and mounted in a fluorinated ethylene propylene (FEP, S2022-04, Bola) tube in 2% low-melting temperature agarose (A4018, Sigma-Aldrich) supplemented with 0.03% tricaine. The FEP tube has an internal diameter of 0.8 mm and an outer diameter of 1.6 mm and was attached to a needle (100 Sterican, 21G x 1 ½", Braun) and syringe (Omnifix F Solo 1 mL, Braun) to be held vertically in the objective chamber.

5.2.4. Intra-cavity dumping characterization

The intra-cavity dumping performance was tested by changing the repetition rate in the range between 3 MHz and 5 kHz and recording in parallel the average power and the voltage generated by the output pulse train on a photodiode (DET10A2, Thorlabs) with 1 ns rise time. The average power was measured with the power

meter (Fieldmate, Coherent) after the the Glan-Laser calcite polarizer. For low average power (range 0.5-30 mW) a semiconductor power sensor head (OP-2VIS, Coherent) was used while for higher average power (above 30 mW) we used a thermopile power sensor head (PM10, Coherent). From the measured average powers for each repetition rate the corresponding pulse energy E_p was calculated with the following formula:

$$E_p = \frac{P_{av}}{f_{rep}} \tag{5.6}$$

The voltage measured by the photodiode gave an experimental indication of the pulse energy as a function of the repetition rate. The photodiode was placed on the exit window of the Glan-Laser calcite polarizer, so the measured voltage is a quantity proportional to the actual pulse energy.

To characterize the performance of the intra-cavity dumping system in synthetic samples, CGHs were projected into fluorescein solution in demineralized water at variable repetition rate. To guarantee a fixed number of laser pulses across the same CGH projected with different repetition rates the aperture of the shutter gating the NIR light was altered. TPEF images of the CGHs were acquired with the sCMOS camera by using the detection arm of the light sheet microscope. The camera exposure was synchronized with the shutter by using a DAQ card (National Instruments) to control both shutter and camera triggers. The camera trigger was activated by the DAQ card when an output wave form was fed to the shutter. The analysis on the TPEF images was performed on 16-bit raw images.

5.2.5. Photoablations

Single-cell ablation at variable repetition rates was performed on 4 dpf embryos. Baseline fluorescence time-lapse images of the brain were acquired with the light sheet microscope by using the 488 nm laser with 10 mW output power. The fluorescence signal was acquired by implementing confocal slit detection to suppress the signal generated by the side lobes of the Bessel beam. A slit was virtually generated using an active window on the camera chip rolled synchronously with the galvo mirror scanning the Bessel beam. The effective frame rate was 11 Hz. During the photostimulation experiment, a single-point CGH was targeted to a single neuron in the midbrain of each embryo. The targeted ROI were manually selected on the baseline fluorescence images through a graphical user interface. The chosen ROIs were located near the center of the lateral FOV (within 70 μm of the center) and appeared as cells in focus, with sharp and bright edges, at the selected plane.

Repetition rates of 1 MHz and 10 kHz were selected to ensure a comparable pulse energy across stimulation conditions (see Figure 5.2(a)). To guarantee that the sample receives the same number of pulses at each repetition rate we altered the opening time of the mechanical shutter gating the NIR light. This time was respectively 5 ms and 500 ms for 1 MHz and 10 kHz repetition rate. To probe the effect of the photostimulation time-lapse images are acquired over a time period of 1 minute starting before the photostimulation event. To analyze GCaMP6f traces, the average fluorescence within ROIs was calculated as $\Delta F/F_0$, where F_0 was the baseline signal prior to photostimulation. Pairwise comparison between the $\Delta F/F_0$

values at different time points was performed through the non-parametric Wilcoxon signed-rank test.

5.2.6. Protein isolation and western blot to detect Heat Shock Protein 70

As a molecular marker for thermal damage, the amount of Hsp70 was measured by fluorescence western blot. Groups of 40 embryos of the same genotype at 72 hours past fertilization (hpf) were irradiated for three hours under unfocused NIR laser light at either 3 MHz or 10 kHz repetition rates. Control groups with same genotype and age were not irradiated, but kept at the same ambient temperature as irradiated siblings. A positive control was made by heat treating 72 hpf embryos, with the same genotype used for other groups, for two hours in a mini-block heater (VWR) at 37 °C.

All groups of embryos were snap frozen with liquid nitrogen immediately after treatment and stored at -80°C. For protein isolation, 20 embryos per group were homogenized in lysis buffer (Ripa buffer, 20-188, Sigma-Aldrich) with a protease inhibitor cocktail (cOmplete, Mini EDTA-free Protease Inhibitor Cocktail, 11836170001, Roche) and phosphatase inhibitor (Phosphatase Inhibitor Cocktail 2, P5726, Sigma-Aldrich). The homogenate was sonicated (3s pulses, 2x) with a probe sonicator (Q125A, QSonica) and then centrifuged (16500 rpm, 20 minutes). The supernatant was collected and the protein concentration determined via a bicinchoninic assay (Pierce BCA protein assay kit, 23225, ThermoFisher Scientific) using bovine serum albumin as reference.

Extracted protein was diluted (1:1) in 2x Laemmli sample buffer (161-0747, Bio-Rad) supplemented with 5% 2-mercaptoethanol (M6250, Sigma-Aldrich) was then denaturated at 95 °C for 10 minutes. The denatured proteins were then separated by molecular weight through gel electrophoresis at 200 V for 45 minutes (Mini-PROTEAN Tetra cell system, 1658005 ;BioRad). Equal amounts of protein lysate (40 μg) were loaded onto 4–15% TGX stain-free precast gels (Mini-PROTEAN® TGX Stain-Free™ Protein Gels, 4568083, BioRad) together with a reference ladder (Precision Plus Protein All Blue standards, 1610373, Bio-Rad). Afterwards the proteins were transferred from gel to Polyvinylidene fluoride (PVDF) membranes (Trans-Blot Turbo 0.2 µm PVDF Transfer Packs, 1704156, BioRad) at 25 V and 1.3 A for 7 minutes via a transfer system (Trans-Blot Turbo Transfer System, 1704150, BioRad).

After transfer the membrane was imaged with a gel imaging system (Gel Doc XR+, 1708195, Bio Rad) to detect the protein loading in each lane and the efficiency of protein transfer from gel onto the PVDF membrane. The detected signal is fluorescence emitted by the proteins irradiated with UV light for 0.8 ms. The fluorescence signal comes from tryptophan residues covalently bound to the trihalo compound contained in the stain-free gel.

After imaging, the membrane was blocked for unspecific binding in phosphate saline buffer (PBS) with 5% skimmed milk (70166, Sigma-Adrich) for one hour at room temperature (20 °C) on a rocking table. The membrane was then incubated overnight at 4°C with an anti-Hsp70 antibody (1:1000, monoclonal anti-Hsp70 an-

tibody, H5147, Sigma-Adrich) in the blocking buffer, was washed 3x15 minutes in PBS with 0.01% Tween (PBSTw, 11332465001, Sigma Aldrich) and incubated in a secondary antibody (1:1000, goat anti-mouse Alexa Fluor 647, A-21236, ThermoFischer) for 2 hours at 20 °C. Finally after washing steps (3x15 minutes in PBStw) the membrane was imaged with a laser scanning fluorescence gel imager (Typhoon RGB, Amersham) using a PMT voltage of 350 V and 647 nm laser excitation.

To quantify the amount of Hsp70, the average intensity of the band at 70 kDa was determined from the image after subtracting an average background measured on a region without any band. Each band was normalized by the total protein as quantified from the image of the stain-free blot. For multiple comparisons among the different experimental groups the non-parametric Kruskal Wallis test was used. Post-hoc pairwise comparisons used the Mann-Whitney test with Bonferroni correction.

5.3. Results

5.3.1. Performance of intra-cavity modulation

The performance of the intra-cavity dumping system in terms of average power, voltage and calculated pulse energy was monitored daily over several weeks, as described in Section 5.2.4. Figure 5.2(a) reports the average values of all those data acquired over time and the corresponding standard deviation. As expected, the average power decreases with lowering the repetition rate while the pulse energy increases. The data show that pulse energy reaches a plateau value when the repetition rate is lower than 1 MHz. Discrepancies between the pulse energy calculated from average power and relative pulse energy measured by photodiode can be attributed to noise in the power meter measurement at very low duty cycles.

To confirm the pulse energy measurements through a nonlinear optical process, we compared the TPEF signal generated in a synthetic fluorescent sample by the intra-cavity dumped laser at different repetition rates: 500 kHz and 3 MHz. We projected a single-spot CGH into the sample chamber filled with fluorescein solution, and acquired TPEF images. On these images we then measured the average TPEF signal as a function of the average power of the laser, tuned at the two different repetition rates. The spot was positioned roughly at the center of the FOV and an image of the TPEF fluorescence was acquired using the sCMOS camera synchronized with the mechanical shutter which gates the stimulation light as described in Section 5.2.4. The exposure time of the camera and the opening time of the shutter were set to different values for the two repetition rates investigated to ensure that the sample was irradiated with the same number of pulses across different repetition rates. Specifically we used an exposure time of 100 ms and 600 ms at repetition rates of 3 MHz and 500 kHz, respectively. However, the precision of the shutter, namely 1 ms, is lower than the time between consecutive pulses. Hence, the total number of incident pulses can vary by 0.1%. Having the integration time fixed to 600 and 100 ms, the error on the number of pulses is respectively 0.017% and 0.1%. Hence, the uncertainty is higher in the case of 3 MHz repetition rate.

From the set of images collected, the average fluorescence intensity was mea-

sured within a ROI of 10 x 10 pixels, centered around the pixel of maximum intensity. Figure 5.2(b) shows the average TPEF intensity as function of average power for 3 MHz and 500 kHz repetition rates. The two quadratic curves show different curvatures because the repetition rate is inversely proportional to the number of absorbed photons. In case of 2P excitation, the number of photon pairs absorbed per second is described by the following equation [18]:

$$N_{abs} \propto \frac{E_p^2 \cdot f_{rep} \cdot \sigma_{2P}}{\tau \cdot A^2} = \frac{\sigma_{2P} \cdot P_{av}^2}{f_{rep} \cdot \tau \cdot A^2} \tag{5.7}$$

where E_p is the pulse energy, f_{rep} is the repetition rate of the laser, σ_{2P} is the 2P cross-section, τ is the pulse duration, P_{av} is the average power, and A is the spot size of the beam at the focus. This equation can be extended to higher order nonlinear absorption processes [20]. The average measured TPEF is proportional to the number of the absorbed photons and, hence, assuming that 2P cross-section σ_{2P}, pulse duration τ and beam focus size A are kept constant across the two series of measurement, the curvature (C) is inversely proportional to the repetition rate. The experimental data in Fig.5.2(b) was fitted with a quadratic function $y = Cx^2$, yielding C values of 2.49 and 55.37 for 3 MHz and 500 kHz data sets, respectively. This means that a 500 kHz pulse train needs 4.70 times lower average power than a 3 MHz pulse train to generate the same fluorescence signal. This result confirms that at lower repetition rate we achieve the same magnitude TPEF signal with lower average power.

5.3.2. Multi-spot CGHs as function of the repetition rate

We next asked whether a lower repetition rate facilitated the multiplexing of points in the CGHs. In parallel photostimulation methods, such as CGH, the available peak power is divided among many focal points. Hence higher peak power should facilitate the multiplexing of the stimulation light.

To answer this question, we projected point-cloud CGHs with progressively increasing number of points into the sample chamber filled with fluorescein solution. The point-cloud holograms had 12, 24, 48 points, respectively. The laser was adjusted to two different repetition rates: 3 MHz and 10 kHz. For each CGH and each repetition rate a TPEF image was acquired with the sCMOS camera. As in the previous experiment, the camera exposure time was synchronized with the aperture of the mechanical shutter gating the excitation light. The shutter opening and camera exposure times at 3 MHz and 10 kHz were both adjusted to guarantee that each image had the same number of NIR pulses at each repetition rate (see Figure 5.4(d)).

Figure 5.3 shows TPEF images of the point-clouds CGHs acquired with different laser repetition rates. Qualitatively, we observe that the images acquired at 10 kHz provide better contrast. Contrast was quantified on the lines profiles averaged across all the individual points, shown by the plots on the right side of Figure 5.3(a-c). These data points were fitted with a Lorentzian depicted as a continuous line and the standard error on the mean (s.e.m.) values are shown as the shadowed area.

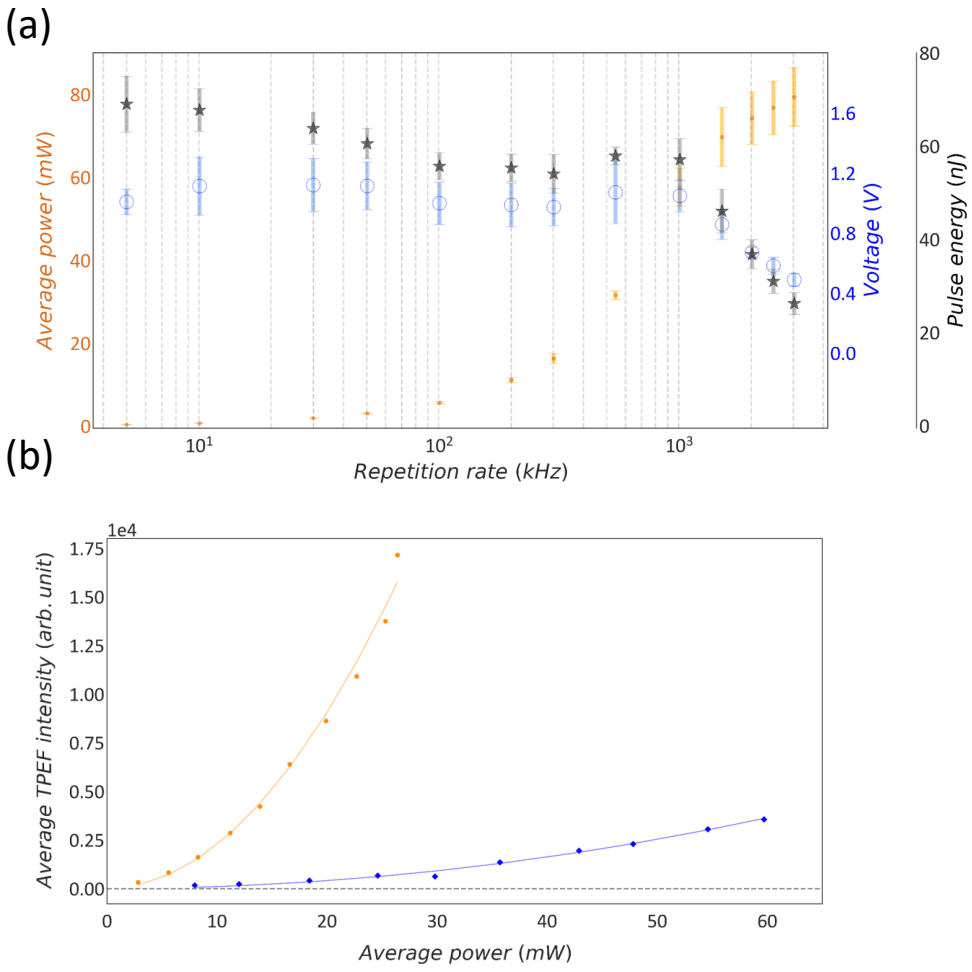

Figure 5.2: **Characterization of intra-cavity dumping in synthetic sample.** (a) Lin-log plot of measured average power, voltage and calculated pulse energy as function of the laser repetition rate. Orange dots: mean average power; blue circles: mean voltage; grey stars: calculated mean pulse energy. Error bars show the standard deviation; n = 13 measurements. (b) Average TPEF intensity as function of P_{av}. Blue rhombuses: 3 MHz repetition rate; orange dots: 500 kHz repetition rate; continuous lines: quadratic fit on the corresponding data points.

It is worth observing that the line profiles of points projected with lower repetition rate have an higher baseline TPEF level compared to their counterparts at higher repetition rate. This is due to the higher camera exposure times used for these acquisitions. In fact, an increase of the camera exposure time causes more background signal. Moreover, we observed variability on the background level across different patterns projected with same repetition rate as a consequence of different camera integration time used for the three patterns. Increasing the

number of points in each CGH pattern we correspondingly increased the laser irradiation time, and consequently the camera exposure. The contrast for each image was evaluated as the difference between the baseline and the maximum TPEF intensity in the average line profile. On those values the error was estimated by propagating the uncertainty on the means.

As reported in Figure 5.3(d), higher contrast TPEF was obtained for the CGHs projected at lower repetition rate compared to the case at higher repetition rate. In our system, the pulse energy associated with a 10 kHz repetition rate is 2.6 ± 0.4 times higher than its value at 3 MHz (see Figure 5.2(a)). The average improvement in contrast was 3.0 ± 0.4. Hence, the average improvement in contrast is comparable to the pulse energy improvement. These experimental results indicate that a lower repetition rate allows to stimulate more points simultaneously.

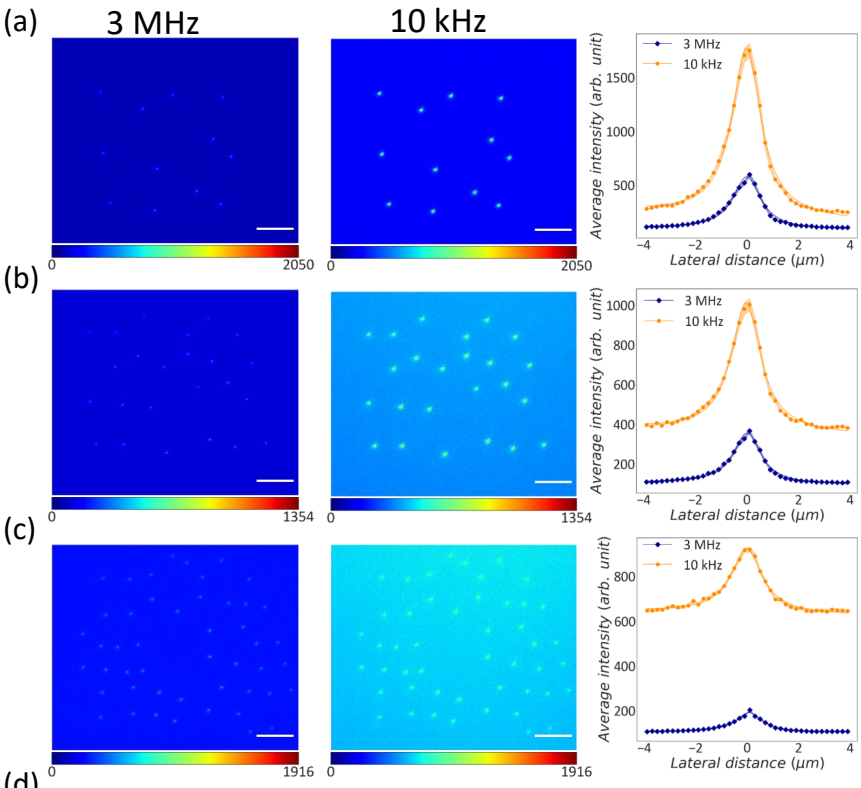

(d)

Points number	12		24		48	
Repetition rate	3MHz	10kHz	3MHz	10kHz	3MHz	10kHz
Exposure time	3 ms	12 ms	20 ms	6 s	40 ms	12 s
Contrast	481 ± 17	1555 ± 71	255 ± 10	645 ± 37	86 ± 3	288 ± 20

Figure 5.3: **Comparison between point-cloud CGHs projected into liquid fluorescein with different repetition rates.** (a) Left: TPEF image of 12-point CGH projected with 3 MHz repetition rate. Middle: TPEF image of the same CGH projected with 10 kHz repetition rate. Scale bar: 25 μm. Right: Average line profiles across the pixel of maximum intensity for all the points projected with 3 MHz (blue rhombuses) and 10 kHz (orange dots) repetition rate. Continuous lines: Lorentzian fit on the data points; shadow areas: s.e.m.; orange: 10 kHz; blue: 3 MHz. (b) Left: TPEF image of 24-point CGH projected with 3 MHz repetition rate. Middle: TPEF image of the same CGH projected with 10 kHz repetition rate. Right: Average line profiles across the pixel of maximum intensity for all the points projected with 3 MHz (blue rhombuses) and 10 kHz (orange dots) repetition rate. Continuous lines: Lorentzian fit on the data points; shadow areas: s.e.m.; orange: 10 kHz; blue: 3 MHz. (c) Left: TPEF image of 48-point CGH projected with 3 MHz repetition rate. This image was enhanced with a gamma factor of 1.2 for visualization. Middle: TPEF image of the same CGH projected with 10 kHz repetition rate. Right: Average line profiles across the pixel of maximum intensity for all the points projected with 3 MHz (blue rhombuses) and 10 kHz (orange dots) repetition rate. Continuous lines: Lorentzian fit on the data points; shadow areas: s.e.m.; orange: 10 kHz; blue: 3 MHz. (d) Table with experimental parameters used to acquire each grid image, contrast and corresponding s.e.m.

5.3.3. Performance *in vivo*

Single cell ablation with variable repetition rate

After the characterization of the intra-cavity dumped Ti:Sapphire laser performance in the synthetic sample, we focused on understanding the effect of the variable repetition rate on photoablation in living zebrafish embryos. For such a purpose we targeted single-point CGHs to single neurons in 4 dpf embryos expressing GCaMP6f in the cytosol with either 1 MHz or 10 kHz laser repetition rate. Before each photoablation, a baseline fluorescence image of the midbrain of the samples was acquired with the light sheet microscope to select the ROI for photostimulation. ROIs were selected to be somata in the optic tectum, near the center of the field of view. Repetition rates 1 MHz and 10 kHz were selected to ensure a comparable pulse energy across photostimulation conditions (see Figure 5.2(a)). To guarantee that the sample receives the same number of pulses in each stimulation configuration we altered the opening time the mechanical shutter gating the NIR light. The effect of the these photostimulations was probed by the simultaneous acquisition of time-lapse images on the same plane where the stimulation CGH was targeted with the conditions described in Section 5.2.5.

The data sets showed that both photostimulation conditions caused single-cell ablation of the targeted cell. In fact, by measuring the fluorescence intensity at the stimulation location over time we registered an increase of the signal at specific time points post stimulation as depicted in Figure 5.4(c). Although this result was consistent across all the data sets, the time course of the fluorescence signal at the stimulation location showed some variability across the different data sets due to the inherent diversity of the specific ROIs involved. Figure 5.4(a) shows two representative traces of the $\Delta F/F_0$ signal over time. The dashed blue trace is representative of the photostimulation at 1 MHz while the continuous orange trace refers to the 10 kHz case. In this specific case we observe that the generated fluorescence signal is comparable and in both cells the calcium response is durable over the recording time.

Figure 5.4(b) captures the $\Delta F/F_0$ for the two stimulation conditions for all the data sets at specific time points: 500 ms and 5s after the stimulation. The box plot highlights that at 10 kHz the median (horizontal blue bars) and the average values (magenta rhombuses) of TPEF signal are higher than their counterpart at 1 MHz. The $\Delta F/F_0$ signal at specific time points after the stimulation was compared among all the ablation experiments realized with the same laser repetition rate. The difference between the $\Delta F/F_0$ signals at the two different time points was not significant in the 1 MHz case, but was significant in the case of 10 kHz irradiation. This confirms that, whereas both conditions were capable of inducing single-cell ablation in living zebrafish embryos, the resulting dynamics of the fluorescence signal was different. More specifically simulations at 10 kHz repetition rate produced a statistically relevant alteration of the Ca^{2+} dynamics during the explored time window, namely 5 s after stimulation.

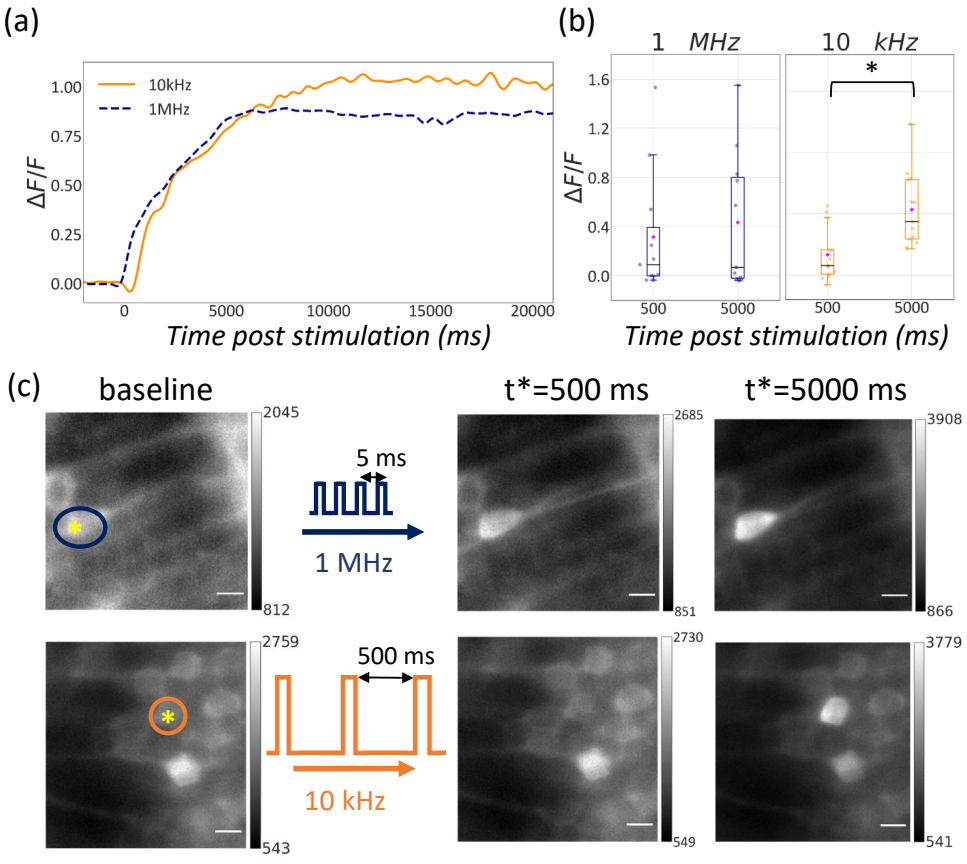

Figure 5.4: **Effect of single-neuron ablation in living zebrafish embryos with variable repetition rate.** (a) $\Delta F/F_0$ signal following photostimulation for two different repetition rates: 1 MHz (blue line), 10 kHz (orange line). (b) Box plots representing the $\Delta F/F_0$ signal at 500 ms and 5 s past stimulation for different repetition rates: 1 MHz (n = 11), 10 kHz (right, n = 13). Blue horizontal bars: median value; magenta rhombuses: mean values. Groups marked with star show statistical significance (Wilcoxon signed-ranked test, p = 0.007). (c) Light sheet images of recorded before and at 500 ms and 5s past stimulation at different repetition rates: 1 MHz (top), 10 kHz (bottom). The yellow asterisk in the baseline images shows the location of the stimulation while the colored circles highlight the cell body to monitor over time. The data sets here reported are the same shown in (a). Scale bar is 5 μm.

Thermal damage investigation under unfocused illumination with different repetition rate

To validate our hypothesis that a lower laser repetition rate makes the sample less vulnerable to thermal load and to the consequent damage, we assessed the expression level of Hsp70 as a function of laser repetition rate. Two groups of embryos were irradiated with unfocused NIR light at different repetition rate, while a third group was heated in a heat block for 2 hours at 37 °C.

We expected that any of these treatment would have increased the expression

level of Hsp70 over the endogenous level. We used unfocused light where no nonlinear absorption was expected, leaving only the thermal effect of NIR absorption. As depicted in Figure 5.5(a), an Eppendorf tube containing 72 hpf zebrafish embryos in 50 μl of embryo medium was placed at the output of the cavity-dumped laser for three hours. The laser beam at this point of the optical path has a diameter of roughly 0.8 mm and it covered the tip of the Eppendorf containing the embryos. For each repetition rate condition we had different average powers, 70 $\pm$ 1 mW and 0.73 $\pm$ 0.01 mW and, consequently, power densities of 13.92 $^{W}/_{cm^2}$ and 0.015 $^{W}/_{cm^2}$. Immediately after the irradiation the samples were prepared for biochemical evaluation of Hsp70 by fluorescence western blot as described in Section 5.2.6. The western blot experiment was repeated five times while the laser irradiation was performed twice. For each western blot experiment we used two different lysates from each group described above. The expression level of the Hsp70 protein over the total amount of protein was quantified as described in Section 5.2.6. A representative fluorescence blot is reported in Figure 5.5(b), top. Figure 5.5(b), bottom shows the total amount of protein used as a loading control to quantify the fluorescence band of the protein of interest.

Figure 5.5(c) shows a box plot of the ratio between the Hsp70 level and the total protein loaded for each group, the scatter plot shows the data points in each group with a different color code and the white rhombuses display the average ratio calculated in each group. Here we observe an higher average ratio for the group irradiated at 3 MHz (34.10 $\pm$ 9.85) compared to the control group (22.49 $\pm$ 5.80) and the group irradiated at 10 kHz (19.35 $\pm$ 5.71). The control group and the group irradiated at 10 kHz showed a lower average amount of Hsp70 compared to the heat-shocked group (34.17 $\pm$ 15.80). Embryos irradiated with 3 MHz light had significantly higher expression Hsp70 than embryos irradiated 10 kHz. Hence, we can conclude that the laser irradiation at 10 kHz repetition rate reduced the thermal load on the sample compared to the 3 MHz pulse train.

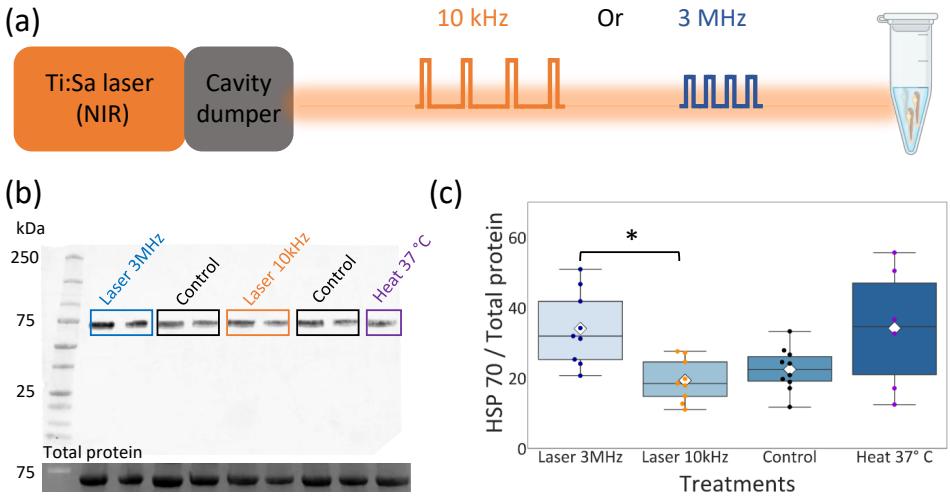

Figure 5.5: **Hsp70 expression level in zebrafish embryos upon NIR illumination.** (a) Layout of zebrafish embryos NIR radiation at different repetition rates. Eppendorf image created with BioRender.com. (b) Top: Representative western blot of whole protein extracted from 72 hpf zebrafish embryos probed with anti-Hsp70 antibody. Bottom: Corresponding stain-free western blot showing the total protein. (c) Box plot for the quantification of the ratio between the expression level of Hsp70 and the total amount of protein. Rhombuses: average values; horizontal black lines: median values; scatter plot: data points in each group with different color code. Groups labeled with star symbols are significantly different (Kruskal-Wallis test, p = 0.02, post-hoc Mann-Whitney test with Bonferroni correction, p = 0.002).

Multiphoton stimulation in living tissues requires a thorough choice of the laser parameters such as average power, repetition rate and pulse energy to perform experiments without alteration of the sample physiology. Podorski and Ranganathan [13] investigated sample heating in the context of scanning TPEF imaging in awake mouse. They reported thermal damage following twenty minutes imaging with an average power of 250–300 mW at 920 nm. Histological markers of thermal damage were observable after twenty minutes of continuous imaging at an average power of 420 mW. They found experimentally that thermal damage was mitigated by imaging at a reduced duty ratio of illumination (for one hour at 33% duty ratio at 400 mW).

Picot and colleagues [12] developed a model to simulate the heat diffusion in 3D in the context of 2P optogenetic stimulation with both extended CGH and scanning approaches. They provided a powerful simulation tool that given the stimulation parameters such as average laser power, irradiation wavelength, diffusion coefficient and density of the sample enables to predict beforehand the thermal heating induced in the sample. The results of this work suggest to use lower repetition rates (in the range 500 kHz–-2 MHz) in parallel stimulation illumination schemes.

In this paper we implemented intra-cavity dumping to introduce an additional

degree of freedom to control thermal damage effects during photostimulation of single cells or sub-cellular compartments in the brain of living zebrafish embryos. Intra-cavity dumping within mode-locked Ti:Sapphire lasers is an established technique to increase the pulse energy of the output laser beam at tunable repetition rates without changing the spectral characteristics of the light [21]. Here this technique enabled to tune the laser repetition rate (typically 76 MHz) in the interval between 5 kHz and 3 MHz achieving at the lower repetition rate an average pulse energy of 69 ± 6 nJ. Moreover, the laser source described can be tuned continuously in the range 720–920 nm, offering flexibility for photostimulation experiments that require less common wavelengths, like uncaging of MNI-glutamate (TPE typically uses 720–760 nm) [22, 23] or azobenzene-derived photoswitches (TPE around 850 nm) [24].

Pulse picking is an alternative approach to reduce the repetition rate of mode-locked lasers. This method is based either on acousto or electro-optical modulation of the laser beam. However, in contrast to the intra-cavity dumping design, the modulation device acts outside the cavity and does not increase pulse energy. Forli and colleagues [25] used pulse-picking to investigate the effect of the repetition rate when stimulating an actuator to induce action potentials. More specifically, they stimulated the somatically-target opsin stCoChR expressed in L2/3 pyramidal cells with holographic patterns delivered at 1 MHz and 50 kHz repetition rate via a fiber laser. They found out that action potentials are evoked with a similar probability when stimulating for 100 ms at 1 MHz (average power: 1 mW and pulse energy 1 nJ) and at 50 kHz (average power: 0.25 mW and pulse energy 5 nJ), hence the lower repetition rate permits to elicit action potentials using one-fourth of the average power.

The gain in terms of pulse energy achieved with intra-cavity dumping is particularly convenient for combination with holographic projections, where the available pulse energy is divided among multiple foci in the pattern. In fact, when the system was employed for point-cloud holographic projections we found that 10 kHz repetition rate eased the multiplexing of the holographic projections compared to the 3 MHz case. By comparing CGH projections with the same number of features at low and high repetition rate, respectively, we observed that the TPEF contrast of the CGH projected at lower repetition rate was higher (see Figure 5.3).

The pulse energy could be further increased by operating the Ti:Sapphire cavity in the positive dispersion regime [26]. In this case, the mode-locked pulse is not transform-limited, but instead positively chirped. Similar to chirped pulse amplification in a regenerative amplifier, the stretching of a chirped pulse allows greater amplification of the pulse before reaching the damage threshold of the gain medium. As reported by Zhou and colleagues [26], operating the Ti:Sapphire oscillator in the positive dispersion mode combined with the intra-cavity dumping enables a single-stage laser system to obtain stable and reliable high peak energies on the order of 450 nJ at variable repetition rates. The same strategy can potentially be applied in the pulseSwitch-Mira laser system by increasing the insertion of the intracavity prism controlling group velocity dispersion. In this approach, extra-cavity pulse compression is needed to obtain transform-limited pulse duration. Higher

peak intensities could be employed to elicit higher order nonlinear processes. For instance, three-photon excitation offers greater confinement of the excitation light, and when combined with longer wavelength light, it is particularly suited for imaging applications in deep tissue [27, 28].

Other laser technologies are also possible, depending on the desired wavelengths. In the Ti:Sapphire range (720-1080 nm), regenerative amplification is a well-known method to reach microjoule pulse energies at repetition rates in the interval 1–500 kHz. Optical parametric amplifiers are also common as a method to generate high energy pulses at longer wavelengths. Both of these methods utilize multiple stages of amplification, adding to the complexity of the laser system.

Irrespective of the light source technology, high energy pulses can produce various types of tissue damage. When a living sample is irradiated with high pulse energy a careful evaluation of the potential nonlinear damage at the geometrical focus in the sample should be performed [29, 30]. Hence, the choice of the laser parameters becomes a trade-off between thermal and nonlinear damage.

We tested the cavity-dumping system in the context of single-cell photoablation as example of powerful manipulation [31, 32]. The ablated cells were characterized by an increase in the fluorescence signal due to the disruption of the cell membrane and a consequent increase of calcium concentration detected by GCaMP6f. We observed that, although the pulses generated at 1 MHz and 10 kHz repetition rate had comparable pulse energy and were capable of inducing single-cell ablation, stimulation at 10 kHz repetition rate induced a relevant alteration of the fluorescence signal dynamics after the ablation event. This is likely due to subtle differences in the tissue damage mechanisms produced at high and low repetition rate. Finally, we investigated the thermal damage induced by NIR light irradiation by quantifying the expression level Hsp70 in living zebrafish. Hsp70 is expressed in zebrafish embryos during healthy development since it assists with folding of newly translated proteins and acts as a molecular chaperone by mediating the repair and degradation of denatured proteins [33]. In this endogenous form the protein is most commonly referred as heat shock cognate 70 and its expression level changes with the developmental stage of the embryo, reaching a peak at 84 hpf [34]. Hsp70 is upregulated under thermal stress conditions and it has the same functions as its non-induced form. As shown by Yeh and colleagues [35], exposing zebrafish embryos between 12 and 108 hpf to a temperature of 37 °C for at least 30 minutes causes increased expression of Hsp70. For such a reason the expression of the Hsp70 is used in this paper as a cellular marker of thermal damage.

The quantification of the Hsp70 via western blot is susceptible to different sources of noise such as the age of the embryos, the laser power stability during the irradiation and the amount of total protein extracted from the embryos. In the experimental design we aimed at minimizing each of these sources of noise to obtain more robust results. The embryos used in the four different groups, here analyzed, were from different clutches and they were carefully age matched to probe the expression level of Hsp70 at the same developmental stage. All groups were kept at the same temperature (20 °C) during the 3-hr irradiation period because temperature is a key parameter in embryonic zebrafish development [36]. In

fact, any temperature variation across the groups may cause a discrepancy in the development stage and hence affect the level of background Hsp70. Ultimately a variation of the non-induced Hsp70 level may impair the comparison between the protein level across the groups because it represents the baseline of the measurement of the induced-Hsp70. However, since at 72 hpf the level of non-induced Hsp70 is not negligible [35] performing the same experiment at an earlier developmental stage may highlight a more pronounced difference in the Hsp70 expression level in samples irradiated with different repetition rates.

Another source of noise is the stability of the average power delivered by the laser during the irradiation time. To take into account any variation in the average power we repeated the irradiation experiment twice and monitored the average power over time. The variability introduced by the efficiency of the protein extraction was mitigated by performing two different protein extractions for each group for each irradiation experiment. When we assessed the thermal damage on 72 hpf zebrafish irradiated for 3 hours by unfocused light at 10 kHz and 3 MHz repetition rates with, respectively, power densities of 0.015 $^{W}/_{cm^2}$ and 13.92 $^{W}/_{cm^2}$ we observed a significant difference in the expression level of the Hsp70. More specifically, the group irradiated at 10 kHz showed an expression level of Hsp70 significantly lower than the group irradiated at 3 MHz. These data confirm the hypothesis that a lower repetition rate drastically reduces the thermal stress on living zebrafish embryos. For such a reason, a lower repetition rate in the order of tens of kHz might be beneficial for optogenetic activation of opsins without thermal damage of the sample. Moreover, the majority of opsins have a photocycle longer (tens of milliseconds [37]) than the time between laser pulses with repetition rates below 1 MHz , hence the use of kHz repetition rates is suitable for the activation of most of the available opsins.

Another strategy to minimize the temperature rise under multi-spot holographic irradiation is to implement the ultra-fast light targeting (FLiT) approach to shape the stimulation light [38]. This method relies on a galvanometric mirror that scans the beam across the SLM tiled with multiple holograms aligned along the vertical dimension. This stimulation design allows to stimulate multiple ROIs in a cyclic fashion with microseconds light exposures while reducing the average power of a factor equal to the square root of the total number of spots.

Besides the application for minimally invasive optogenetics experiments the 2P-CGH module equipped with intra-cavity dumping could be used at higher repetition rate to irradiate zebrafish embryos that express a desired gene under the heat shock protein 70 (hsp70) promoter. This promoter is a tool to drive a transient gene expression in a specific time window given by the increase of temperature which activates the promoter [39]. Transient expression under the hsp70 promoter was realized by exposing the whole embryo to 38 °C temperature [39], via a temperature controlled needle [40] or via a dye-laser focused through a high NA objective of a microscope [41]. The system here presented offers the possibility to drive the hsp70-dependent expression at multiple locations simultaneously with single-cell precision.

5.4. Conclusion

Here we integrated an intra-cavity-dumped laser with variable repetition rate with a setup for all-optical studies in living animals to introduce a new dimension of control in photostimulation experiments. We tested the system in synthetic samples and we observed that a lower repetition rate eases the projection of multi-spots holographic patterns. Moreover we found that at lower repetition rate comparable TPEF signal can be elicited with lower average power. The same system was tested on living zebrafish embryos where a lower repetition rate allows to achieve similar performance in terms of single neurons ablation reducing drastically the average power. Finally, the investigation of thermal response upon low and higher repetition rate irradiation provided a significant difference in thermal stress. A low repetition rate (10 kHz) showed a lower expression level of the thermal damage molecular marker compared to an higher repetition rate (3 MHz). This study paves the way to the implementation of intra-cavity dumped lasers within optical modules for optogenetic simulations with minimally invasive thermal conditions. The same system operated with higher repetition rate and higher average power could be used for conditional gene expression under the hsp70 promoter with single-cell resolution. In conclusion a intra-cavity dumped laser integrated into an optical setup for all-optical studies in living animals allows to perform photostimulation experiments with progressively increasing thermal perturbation on the samples according to the specific application one wants to realize.

References

[1] V. Emiliani, A.E. Cohen, K. Deisseroth, and M. Häusser., "Symposium All-Optical Interrogation of Neural Circuits," *The Journal of Neuroscience*, vol. 35, no. 41, pp. 13917–13926, 2015.

[2] R. H. Kramer, A. Mourot, and H. Adesnik, "Optogenetic pharmacology for control of native neuronal signaling proteins," *Nature Neuroscience*, vol. 16, no. 7, pp. 816–823, 2013.

[3] M. Dal Maschio, J. C. Donovan, T. O. Helmbrecht, and H. Baier, "Linking Neurons to Network Function and Behavior by Two-Photon Holographic Optogenetics and Volumetric Imaging," *Neuron*, vol. 94, no. 4, pp. 774–789, 2017.

[4] A. R. Mardinly, I. A. Oldenburg, N. C. Pégard, S. Sridharan, E. H. Lyall, K. Chesnov, S. G. Brohawn, L. Waller, and H. Adesnik, "Precise multimodal optical control of neural ensemble activity," *Nature Neuroscience*, vol. 21, no. 6, pp. 881–893, 2018.

[5] J. P. Rickgauer and D. W. Tank, "Two-photon excitation of channelrhodopsin-2 at saturation," *Proceedings of the National Academy of Sciences of the United States of America*, vol. 106, no. 35, pp. 15025–15030, 2009.

[6] J. A. Curcio and C. C. Petty, "The Near Infrared Absorption Spectrum of Liquid Water," *Journal of the Optical Society of America*, vol. 41, no. 5, pp. 302–304, 1951.

[7] M. Rauzi and P. F. Lenne, "Cortical Forces in Cell Shape Changes and Tissue Morphogenesis," *Current Topics in Developmental Biology*, vol. 95, pp. 93–144, 2011.

[8] K.König, "Multiphoton microscopy in life sciences," *Journal of Microscopy*, vol. 200, no. 2, pp. 83–104, 2000.

[9] P. Andersen and E. I. Moser, "Brain temperature and hippocampal function," *Hippocampus*, vol. 5, no. 6, pp. 491–498, 1995.

[10] J. M. Stujenske, T. Spellman, and J. A. Gordon, "Modeling the Spatiotemporal Dynamics of Light and Heat Propagation for InVivo Optogenetics," *Cell Reports*, vol. 12, no. 3, pp. 525–534, 2015.

[11] W. Deng, E. M. Goldys, M. M. Farnham, and P. M. Pilowsky, "Optogenetics, the intersection between physics and neuroscience: Light stimulation of neurons in physiological conditions," *American Journal of Physiology - Regulatory Integrative and Comparative Physiology*, vol. 307, no. 11, pp. R1292–R1302, 2014.

[12] A. Picot, S. Dominguez, C. Liu, I. W. Chen, D. Tanese, E. Ronzitti, P. Berto, E. Papagiakoumou, D. Oron, G. Tessier, B. C. Forget, and V. Emiliani, "Temperature Rise under Two-Photon Optogenetic Brain Stimulation," *Cell Reports*, vol. 24, no. 5, pp. 1243–1253, 2018.

[13] K. Podgorski and G. Ranganathan, "Brain heating induced by near-infrared lasers during multiphoton microscopy," *Journal of Neurophysiology*, vol. 116, no. 3, pp. 1012–1023, 2016.

[14] T. Wang, C. Wu, D. G. Ouzounov, W. Gu, F. Xia, M. Kim, X. Yang, M. R. Warden, and C. Xu, "Quantitative analysis of 1300-nm three-photon calcium imaging in the mouse brain," *eLife*, vol. 9, no. e53205, 2020.

[15] E. Chaigneau, E. Ronzitti, M. A. Gajowa, G. J. Soler-Llavina, D. Tanese, A. Y. Brureau, E. Papagiakoumou, H. Zeng, and V. Emiliani, "Two-photon holographic stimulation of ReaChR," *Frontiers in Cellular Neuroscience*, vol. 10, p. 234, 2016.

[16] E. Ronzitti, R. Conti, V. Zampini, D. Tanese, A. J. Foust, N. Klapoetke, E. S. Boyden, E. Papagiakoumou, and V. Emiliani, "Submillisecond optogenetic control of neuronal firing with two-photon holographic photoactivation of chronos," *Journal of Neuroscience*, vol. 37, no. 44, pp. 10679–10689, 2017.

[17] B. R. Masters, P. T. C. So, C. Buehler, N. Barry, J. D. Sutin, W. W. Mantulin, and E. Gratton, "Mitigating thermal mechanical damage potential during two-photon dermal imaging," *Journal of Biomedical Optics*, vol. 9, no. 6, pp. 1265–1270, 2004.

[18] P. G. Antal and R. Szipocs, "Tunable, low-repetition-rate, cost-efficient femtosecond Ti:sapphire laser for nonlinear microscopy," *Applied Physics B: Lasers and Optics*, vol. 107, no. 1, pp. 17–22, 2012.

[19] T.-W. Chen, T. J. Wardill, Y. Sun, S. R. Pulver, S. L. Renninger, A. Baohan, E. R. Schreiter, R. A. Kerr, M. B. Orger, V. Jayaraman, L. L. Looger, K. Svoboda, and D. S. Kim, "Ultra-sensitive fluorescent proteins for imaging neuronal activity," *Nature*, vol. 499, no. 7458, pp. 295–300, 2013.

[20] L.-C. Cheng, N. G. Horton, K. Wang, S.-J. Chen, and C. Xu, "Measurements of multiphoton action cross sections for multiphoton microscopy," *Biomedical Optics Express*, vol. 5, no. 10, 2014.

[21] M. Ramaswamy, M. Ulman, J. Paye, and J. G. Fujimoto, "Cavity-dumped femtosecond Kerr-lens mode-locked Ti:Al2O3 laser," *Optics Letters*, vol. 18, no. 1822, pp. 1822–1824, 1993.

[22] G. C. R. Ellis-Davies, "Two-Photon Uncaging of Glutamate," *Frontiers in Synaptic Neuroscience*, vol. 10, no. 48, 2019.

[23] V. Nikolenko, B. O. Watson, R. Araya, A. Woodruff, D. S. Peterka, and R. Yuste, "SLM microscopy: Scanless two-photon imaging and photostimulation with spatial light modulators," *Frontiers in Neural Circuits*, vol. 2, 2008.

[24] E. C. Carroll, S. Berlin, J. Levitz, M. A. Kienzler, Z. Yuan, D. Madsen, D. S. Larsen, E. Y. Isacoff, and W. Denk, "Two-photon brightness of azobenzene photoswitches designed for glutamate receptor optogenetics," *Proceedings of the National Academy of Sciences of the United States of America*, vol. 112, no. 7, pp. E776–E785, 2015.

[25] A. Forli, M. Pisoni, Y. Printz, O. Yizhar, and T. Fellin, "Optogenetic strategies for high-efficiency all-optical interrogation using blue-light-sensitive opsins," *eLife*, vol. 10, no. e63359., 2021.

[26] X. Zhou, H. Kapteyn, and M. Murnane, "Positive-dispersion cavity-dumped Ti: sapphire laser oscillator and its application to white light generation," *Optics Express*, vol. 14, no. 21, pp. 9750–9757, 2006.

[27] N. G. Horton, K. Wang, D. Kobat, C. G. Clark, F. W. Wise, C. B. Schaffer, and C. Xu, "In vivo three-photon microscopy of subcortical structures within an intact mouse brain," *Nature Photonics*, vol. 7, no. 3, 2013.

[28] T. Wang, D. G. Ouzounov, C. Wu, N. G. Horton, B. Zhang, C. H. Wu, Y. Zhang, M. J. Schnitzer, and C. Xu, "Three-photon imaging of mouse brain structure and function through the intact skull," *Nature Methods*, vol. 15, no. 10, 2018.

[29] L. E. Russell, H. W. Dalgleish, R. Nutbrown, O. M. Gauld, D. Herrmann, M. Fişek, A. M. Packer, and M. Häusser, "All-optical interrogation of neural circuits in behaving mice," *Nature Protocols*, vol. 17, pp. 11579—1620, 2022.

[30] E. Ronzitti, V. Emiliani, and E. Papagiakoumou, "Methods for three-dimensional all-optical manipulation of neural circuits," *Frontiers in Cellular Neuroscience*, vol. 12, no. 469, 2018.

[31] G. de Medeiros, D. Kromm, B. Balazs, N. Norlin, S. Günther, E. Izquierdo, P. Ronchi, S. Komoto, U. Krzic, Y. Schwab, F. Peri, S. de Renzis, M. Leptin, M. Rauzi, and L. Hufnagel, "Cell and tissue manipulation with ultrashort infrared laser pulses in light-sheet microscopy," *Scientific Reports*, vol. 10, pp. 1–12, 12 2020.

[32] S. Peron, R. Pancholi, B. Voelcker, J. D. Wittenbach, H. F. Ólafsdóttir, J. Freeman, and K. Svoboda, "Recurrent interactions in local cortical circuits," *Nature*, vol. 579, pp. 256–259, 3 2020.

[33] N. Basu, A. E. Todgham, P. A. Ackerman, M. R. Bibeau, K. Nakano, P. M. Schulte, and G. K. Iwama, "Heat shock protein genes and their functional significance in fish," *Gene*, vol. 295, no. 2, pp. 173–183, 2002.

[34] L. Y. Hsu, F. L. Yeh, T. Y. Cheng, Y. H. Chang, S. M. Liu, and T. Hsu, "A spontaneous high expression of heat shock cognate 70 (HSC 70) in zebrafish Danio rerio larvae arising from tissue-specific translation of preexisting mRNA," *Fisheries Science*, vol. 76, no. 5, pp. 857–864, 2010.

[35] F. L. Yeh and T. Hsu, "Detection of a spontaneous high expression of heat shock protein 70 in developing zebrafish (danio rerio)," *Bioscience, Biotechnology and Biochemistry*, vol. 64, no. 3, pp. 592–595, 2000.

[36] C. B. Kimmel, W. W. Ballard, S. R. Kimmel, B. Ullmann, and T. F. Schilling, "Stages of embryonic development of the zebrafish," *Developmental Dynamics*, vol. 203, no. 3, pp. 253–310, 1995.

[37] F. Zhang, J. Vierock, O. Yizhar, L. E. Fenno, S. Tsunoda, A. Kianianmomeni, M. Prigge, A. Berndt, J. Cushman, J. Polle, J. Magnuson, P. Hegemann, and K. Deisseroth, "The microbial opsin family of optogenetic tools," *Cell*, vol. 147, no. 7, pp. 1446–1457, 2011.

[38] G. Faini, C. Molinier, C. Telliez, C. Tourain, B. C. Forget, E. Ronzitti, and V. Emiliani, "Ultrafast Light Targeting for High-Throughput Precise Control of Neuronal Networks," *bioRxiv*, 2021.

[39] W. Shoji and M. Sato-Maeda, "Application of heat shock promoter in transgenic zebrafish," *Development, growth & differentiation*, vol. 50, no. 6, pp. 401–406, 2008.

[40] M. E. Hardy, L. V. Ross, and C. B. Chien, "Focal gene misexpression in zebrafish embryos induced by local heat shock using a modified soldering iron," *Developmental Dynamics*, vol. 236, no. 11, pp. 3071–3076, 2007.

[41] W. Shoji, S. Isogai, M. Sato-Maeda, M. Obinata, and J. Y. Kuwada, "Semaphorin3a1 regulates angioblast migration and vascular development in zebrafish embryos," *Development*, vol. 130, no. 14, pp. 3227–3236, 2003.

6

Conclusions and outlook

This thesis focused on developing optical techniques to perform all-optical studies of physiology in living animal models with specific emphasis on sub-cellular optogenetics on larval zebrafish brain. In this context, I improved the existing technology on three aspects: I sped up the hologram computation, I compensated for aberrations on the reconstructed holographic stimulation, and finally, I investigated the thermal damage caused by NIR irradiation on the living samples as function of the laser parameters. In this chapter I summarize the results achieved and I provide a possible outlook for the research in this field.

6.1. Conclusions

The main focus of this thesis was to implement and improve upon optical technologies to perform sub-cellular optogenetics experiments in living animals. The optical tools developed were applied in living zebrafish embryos but they can also be extended to physiological studies in other model animals. Such experiments require a microscope to visualize fluorescence from the sample and an optical module to stimulate the optogenetic tools within a single instrument. The microscope needs to provide fast (on the order of 10 Hz), large field of view (on the order of 500 μm to encompass the lateral extension of the larval zebrafish brain) and low photoxicity imaging. The light delivery method to stimulate the optogenetic actuators within a densely packed environment, as the brain of a larval zebrafish, should be able to flexibly produce user-defined patterns targeting multiple cells simultaneously using tightly focused light deep in the tissue. For such reasons holographic shaping of pulsed near infrared (NIR) light was here employed.

In this parallel stimulation scheme, the computational cost of the hologram calculation should be minimized while the fidelity between the target and the reconstructed pattern should be maximized ensuring high diffraction efficiency and uniformity. Ideally, in real-time optical interrogation of neurons, the goal is to switch between different stimulation patterns with high precision to match the time scale of the dynamically changing target structures.

Regardless of the computational method adopted, the quality of the reconstructed hologram is compromised when the holographic projections propagate through turbid media. Hence, a method to counteract these distortions is required to restore the optimal efficiency of the holographic stimulation. Another limitation that may occur when exposing living samples to NIR light is thermal damage. Sample heating can alter the physiology of the sample and thus impair the results of an *in vivo* experiment.

To tackle these challenges, this thesis work addressed three distinct building blocks to improve the existing optical technologies towards sub-cellular optogenetics. In Chapter 3, I implemented a faster algorithm to compute holographic patterns. In Chapter 4, I developed a method to compensate aberrations in holographic projections propagating through turbid media. Finally, in Chapter 5, I presented a flexible method to control the NIR pulse parameters for stimulation and I measured the effect of those parameters on the thermal damage occurred to zebrafish embryos.

Before diving into the details, in Chapter 2 I described the instrument used in this work to test the development of such improvements. More specifically, I addressed the benefits and the technical aspects to successfully integrate an optogenetics module within a light sheet microscope.

In the following I provide a summary of each chapter along with possible upgrades and future directions for the research here described.

6.1.1. Integration of optogenetics module into a light sheet microscope

In all-optical studies of living animal brain one of the fundamental technological challenges is to incorporate a photostimulation module into a microscope for functional imaging. Such a compact instrument enables for fully-optical perturbation and monitoring of the living brain in three-dimensions (3D). The fundamental characteristic of the instrument is the capability of independently manipulate and image the structures of interest.

In Chapter 2 a review of the state-of-the-art technology for variations of light sheet microscopy is provided. Light sheet microscopy is based on illumination of a specific plane with a thin sheet of light and orthogonal detection. Thus, this design offers intrinsic optical sectioning, reduced phototoxicity [1] for long term imaging and increased speed compared to confocal point-scanning microscopies. The faster acquisition is mainly due to the wide field detection of the fluorescent signal usually realized through scientific complementary metal-oxide-superconductors (sCMOS) cameras. A comparative study between light sheet and spinning disc confocal microscopy revealed that comparable imaging time of bones in developing zebrafish embryos produced alteration in the bones morphology when the imaging was performed with the spinning disc confocal method rather than with light sheet [2]. Building upon previous work [3, 4] the essential focus of Chapter 2 is to describe how an optogenetics module can be integrated into a light sheet microscope. The instrument here presented is suitable for 3D cellular or sub-cellular optogenetic stimulation in living zebrafish embryos. The microscope illumination light is engineered to produce a Bessel beam which offers, for the same lateral field of view (FOV), superior axial resolution compared to Gaussian illumination [5]. To date other light sheet configurations could be employed for the same application such as lattice light sheet microscopy [6]. This microscope design provides increased resolution in both cellular samples and *in toto* animals while its implementation may reduce the FOV. Moreover, the same SLM used to generate the lattice can be employed as adaptive element to compensate aberrations on the excitation arm of the imaging module.

The light sheet I designed uses a fixed, common-path objective lens for both detecting fluorescence and reconstructing the 3D hologram. In contrast, approaches where the volumetric imaging is realized through fast axial movement of the objective lens with piezoelectric actuators could make the combination with the photostimulation module cumbersome. In such configurations the same objective is used for imaging and to deliver the stimulation, hence the photostimulation foci need to be readjusted to compensate the movement of the objective, making this solution not ideal for many planes acquisition [7]. The volumetric imaging is performed with an electrically tunable lens and the optogenetic stimulation module uses the high numerical aperture (NA) detection objective of the microscope to focus NIR light shaped with computer generated holography (CGH). Another solution to implement 3D imaging is to include in the detection path a remote focusing unit which allows to perform 3D imaging without moving the main objective used to focus the photostimulation [8]. Light field microscopy is another alternative to acquire 3D

images using lenslets arrays at the camera plane and a software to reconstruct the images. Whereas the imaging speed is only limited by the camera acquisition rate this strategy struggles to image highly scattering specimens and it is restricted to quasi-transparent ones [9].

On the photostimulation side, CGH provides exquisite flexibility being able to shape the stimulation light according to user defined patterns targeting either multiple single somata or multiple sub-cellular regions. For real-time manipulation in vivo the stimulation pattern needs to adapt over time to match the target structures that change dynamically. Hence the stimulation module should be able to refresh the holograms with a temporal precision on the order of seconds. Here the limiting factor is the SLM refresh rate and the speed of the algorithm to compute computer generated holograms (CGHs).The improvements on the speed of the CGH computation are addressed in Chapter 3 while the refresh rate of the SLM is an intrinsic feature of the modulator and it can be increased by modifying the hardware.

In optogenetic stimulation Liquid Crystal (LC) on Silicon SLMs are typically used. Nematic LC are usually employed since they ensure high diffraction efficiency and reasonable time response. Whereas ferroelectric LC have the best time response (kHz refresh rate) they allow only binary phase modulation which is not suitable to support the high diffraction efficiency needed to generate complex excitation patterns and aberration correction in two-photon systems [10].

The overall response time or frame rate of LC-SLMs depends on two main factors: the response time of LC molecules and the speed of communication between the modulator controller and the computer used to load the patterns. The time response of the LC depends on the transition time of the LC molecules, namely the time needed to reorient between two different voltages applied, and the hardware interface used to transfer the CGH to the device. The typical time response for LC is approximately up to 30 ms depending on the light wavelength, longer wavelength imply longer time response.

Another limitation on the speed is imposed by the video interface to establish the communication between the controller of the modulator and the computer. Standard video interfaces such as DVI or HDMI provide an update rate of the CGH limited by the graphic card of the computer. If a custom graphic card is used the hardware interface can support up to 200 Hz refresh rate whereas for a standard graphic card the refresh rate can be up to 60 Hz. These rates combined with the LC time response give a pattern refresh rate in the range of 30-60 Hz. Differently PCI Express interface provide update rates in the order of tens kHz. These interfaces are usually exploited in a method called overdrive which has been widely used to increase the refresh rate of LC-SLMs. In this method instead of switching directly to the final voltage associated with the desired phase, the maximum (or minimum, depending on the direction of the phase change) voltage available is imposed on the device until the final voltage is achieved.

The phase transition becomes faster if larger voltages are transiently applied to the silicon back-plane. In order to implement this technique the SLM back-plane has to be driven with sufficient voltage stoke and with a fast hardware interface. Specifically the driving electronics has to be faster than the typical transition time.

To this end, PCI Express interfaces provide a good refresh rate which combined with the faster response LC response can give a pattern refresh rate of hundreds of Hz.

The Ritsch-Marte research group combined the overdrive approach with the phase change reduction method where the phase stroke between two consecutive pattern is minimized by extending the phase range to intervals higher than 2π. The synergy between overdrive and phase change reduction permitted to obtain a LC-SLM with 250 Hz refresh rate and an increased diffraction efficiency when switching between different patterns [11]. Boulder Nonlinear Systems by implementing this method designed and tested an SLM with 500 Hz refresh rate [12]. Currently Meadowlark optics offers LC-SLMs with PCI Express interfaces that can support frames rates up to 700 Hz.

However, a further improvement on the refresh rate might come from the research and development on SLMs based on micromechanical system (MEMS) mirrors which could potentially offer refresh rates in the order of kHz. Recently piston motion MEMS mirrors were employed as axially focusing devices with update rates of 10 kHz [13].

The SLM currently used in the instrument here presented has a maximum refresh rate of 31 Hz, hence replacing it with an SLM equipped with PCI Express interface with at least 100 Hz refresh rate will increase the temporal performance of the optogenetic stimulation module.

Another limiting aspect on the temporal performance of the stimulation module is the light gating device here used: a mechanical shutter with time precision of 1 ms. The mechanical shutter could be replaced with an electo-optical modulator or Pockels cell which operates at frequencies on the order of hundreds of kHz. Pockels cells rely on the electro-optical effect, hence the light traveling through the modulator experiences the electrically-induced birefringence of the material. More specifically, when the impinging light is plane polarized after propagating into the modulator it is resolved into two orthogonal components that acquire a mutual phase retardation proportional to the applied electric field. When this retarder is placed between two crossed polarizers with their transmission axes at 45° with respect to the retarder axes it acts as a fast shutter. The transmittance of this whole system is a periodic function of the voltage applied to the Pockels cell, hence changing the voltage we can switch between open-close configurations.

These two design upgrade would boost the ability of the stimulation module here described to switch between different stimulation patterns ”on-the-fly” to target structures with dynamics on the millisecond time scale.

6.1.2. Fast holograms calculation

As described in Chapter 3, improvements on the calculation speed of CGHs have been made by developing a new algorithm for hologram calculation, namely compressive sensing weighted Gerchberg–Saxton (CS-WGS). This algorithm reduced the computational time by at least 10 fold compared to the standard Gerchberg–Saxton algorithm without compromising the hologram brightness and uniformity. The hologram can either be a multi-spot pattern or an extended pattern matching

the size of the cell bodies of interest. In the case of extended patterns the CGH is calculated as the convolution between a multi-spot CGH targeting the center of the regions of interest (ROIs) and an extended CGH (calculated via image-based method) located in the center of the FOV with the size matching the ROIs of interest. The CS-WGS algorithm allows to compute CGH "on-the-fly" during *in vivo* photostimultion experiments. However, the speed of the hologram generation can be further improved by implementing the calculation on a consumer graphical processors (GPU) as recently reported by Pozzi *et al.* [14]. The GPU calculation allows the generation of holograms at video rate.

6.1.3. Correct for aberrations on holographic projections

As described in Chapter 4, any CGH propagating though turbid media is distorted by optical aberrations. In order to overcome the detrimental effect in terms of photostimulation efficiency, I implemented a sensorless adaptive optics (AO) approach to counteract aberrations on the photostimulation light. The AO method here presented can correct local aberrations for both system and sample induced aberrations. In both cases the anisoplanatic correction improves the intensity of the stimulation pattern at least two-fold. This method is easy to implement since it does not require any additional element to the existing photostimulation module, but rather uses optimization of two-photon excited fluorescence as a guide star.

However, the algorithm here implemented suffers from a limited speed in retrieving the optimal correction. The speed factor is particularly relevant when dealing with living samples where sample drift, photobleaching and other phenomena can impair the correction search due to loss of intensity during the process. Moreover, a living sample imposes also constraints on the amount of delivered light to minimize photo-toxic effects. In this picture it would be beneficial to speed up the whole correction algorithm. This can be accomplished by replacing the sequential search of the optimal correction by the hill-climb method which is quite inefficient. A valid alternative is an approach similar to the one described in [15] where the range of the coefficients explored for each Zernike mode is based on the previous measurement with a random perturbation to ensure an adequate exploration of the bias coefficients space.

6.1.4. Flexible control of the NIR laser stimulation parameters

In Chapter 5, an intra-cavity dumping system is implemented within the mode-locked Ti:Sapphire laser used for two-photon stimulation. This technology allows to control directly pulse energy, average power and repetition rate of the stimulation light providing a new dimension of control in photostimulation experiments. Here, I demonstrated that a lower repetition rate implies higher pulse energy and thus it facilitates the multiplexing performances of holographic projections. At the same time the average power of the laser is reduced and consequently also the thermal load on the sample.

Further improvements in terms of higher pulse energy could be achieved by operating the laser cavity in positive dispersion regime which in combination with the intra-cavity dumping enables to obtain stable and reliable high peak energies,

in the order of 450 nJ at variable repetition rates [16]. However, extra-cavity pulse compression is needed to obtain transform-limited pulse duration. Moreover, when a living sample is irradiated with high pulse energy a careful evaluation of the potential non-linear damage on the sample should be performed [17, 18].

The intra-cavity dumping system allowed to investigate the effect of NIR laser parameters such as average power and repetition rate on the thermal damage on living zebrafish embryos. After the NIR irradiation of living zebrafish embryos with different laser parameters I assessed the thermal damage by quantifying the expression level of a molecular marker of thermal damage: the heat shock protein 70 (Hsp70). Lower repetition rate (10 kHz) associated with lower average powers ($\sim 0.77 \pm 0.01$ mW) resulted to induce an expression level of the Hsp70 comparable to the level in the samples which were not exposed to NIR light. Contrarily, higher repetitions rates (3 MHz) with corresponding higher average powers ($\sim 70 \pm 1$ mW) proved to up regulate the expression level of the Hsp70. Hence, those figures help to draw the minimally invasive laser parameters, in terms of thermal harm, for photostimulation experiments *in vivo*.

Indications to use lower repetition rates (in the range 500 kHz–2 MHz) in parallel stimulation approaches is given also by Picot and colleagues [19]. They studied extensively the temperature rise consequent to 2P optogenetics stimulation both in the case of parallel stimulation with extended CGHs and scanning approaches. They developed a model to simulate the propagation and heat diffusion in 3D under different illumination conditions. This work provided a powerful simulation tool that given the stimulation parameters such as average laser power, irradiation wavelength, diffusion coefficient and density of the sample enables to predict beforehand the thermal heating induced in the sample. Ultimately the experimenter can choose the laser parameters to perform minimally invasive experiments.

The same research group offered another strategy to minimize the temperature rise under multi-spot holographic irradiation. This approach called ultra-fast light targeting (FLiT) acts on the method to shape and deliver the stimulation light [20]. It relies on a galvanometric mirror which scans the beam across the SLM tiled with multiple holograms aligned along the vertical dimension. This stimulation design allows to stimulate multiple ROIs in a cyclic fashion with microseconds light exposures while reducing the average power of a factor equal to the square root of the total number of spots.

The optical system presented in Chapter 5 could also be used with more invasive laser parameters (higher average power and higher repetition rate) to intentionally increase the temperature to express an exogenous gene under the hsp70 promoter. This promoter is a tool to drive a transient gene expression in a specific time window given by the increase of temperature which activates the promoter [21].

In synthesis, the intra-cavity dumping system integrated to the 2P-CGH stimulation module offers the possibility to dynamically control the stimulation laser parameters to induce in the sample either minimal alteration of temperature or heating. Both conditions have a direct application. In the first case, this system can be used as optogenetics module to study physiology *in vivo* with minimal thermal damage. In the latter case the 2P-CGH module can be employed to drive transient gene

expression with single cell precision in living embryos expressing the construct of interest under the hsp70 promoter.

6.2. Outlook

This thesis work provides three improvements upon the existing optical technology for all-optical interrogation of neurons *in vivo*. A faster algorithm to calculate computer generated holograms, a method to correct local aberrations in the stimulation light and, finally, minimally invasive laser parameters to focus ultrashort pulses of NIR light in living animals. These methods were characterized and validated in living zebrafish brain separately but they can be used in combination to attain higher precision and flexibility in optogenetic experiments. In practice, further work is needed to improve the speed of the local aberration correction and additional upgrades to the experimental setup can be envisioned to increase the temporal resolution. Nonetheless, the optical tools developed here take the field of all-optical interrogation of neural circuits one step closer to real-time control over neuronal physiology and development at the sub-cellular level.

In recent studies sub-cellular optogenetics has been applied to manipulate second messengers as reported by Tanwar [22] and colleagues where they optically modulated a second messenger such as Adenosine 3',5'-cyclic monophosphate (cAMP) to gain insight into the dynamics of ion channels as Hyper polarization-activated cyclic nucleotide gated channels (HCN). This approach required the combination of the optogenetics toolkit with super-resolution microscopy.

The synergy between these techniques paves the way to relevant innovations in the study of synapses formation and growth in developing animals. A single neuron has up to thousands of synapses where Ca^{2+} signals are received and processed. Hence, an optical instrument able to image photoactivatable calcium reporters with the high resolution provided by nanoscopy techniques could reveal the mechanisms underlying single synapses development. Such an instrument could be a light sheet microscope implementing photo-activated localization microscopy (PALM). At the same time the stimulation confinement should be pushed as close as possible to the diffraction limit with the use of adaptive optics to ensure precise targeting of sub-cellular domains.

References

[1] P. J. Keller, A. D. Schmidt, J. Wittbrodt, and E. H. Stelzer, "Reconstruction of zebrafish early embryonic development by scanned light sheet microscopy," *Science*, vol. 322, no. 5904, pp. 1065–1069, 2008.

[2] M. Jemielita, M. J. Taormina, A. Delaurier, C. B. Kimmel, and R. Parthasarathy, "Comparing phototoxicity during the development of a zebrafish craniofacial bone using confocal and light sheet fluorescence microscopy techniques," *Journal of Biophotonics*, vol. 6, no. 11-12, pp. 920–928, 2013.

[3] C. Pantoja, A. Hoagland, E. C. Carroll, V. Karalis, A. Conner, and E. Y. Isacoff,

"Neuromodulatory Regulation of Behavioral Individuality in Zebrafish," *Neuron*, vol. 91, no. 3, pp. 587–601, 2016.

[4] B. R. Rost, F. Schneider-Warme, D. Schmitz, and P. Hegemann, "Optogenetic Tools for Subcellular Applications in Neuroscience," *Neuron*, vol. 96, pp. 572–603, 11 2017.

[5] E. Remacha, L. Friedrich, J. Vermot, and F. O. Fahrbach, "How to define and optimize axial resolution in light-sheet microscopy: a simulation-based approach," *Biomedical Optics Express*, vol. 11, no. 1, pp. 8–26, 2020.

[6] B. C. Chen, W. R. Legant, K. Wang, L. Shao, D. E. Milkie, M. W. Davidson, C. Janetopoulos, X. S. Wu, J. A. Hammer, Z. Liu, B. P. English, Y. Mimori-Kiyosue, D. P. Romero, A. T. Ritter, J. Lippincott-Schwartz, L. Fritz-Laylin, R. D. Mullins, D. M. Mitchell, J. N. Bembenek, A. C. Reymann, R. Böhme, S. W. Grill, J. T. Wang, G. Seydoux, U. S. Tulu, D. P. Kiehart, and E. Betzig, "Lattice light-sheet microscopy: Imaging molecules to embryos at high spatiotemporal resolution," *Science*, vol. 346, no. 6208, p. 1257998, 2014.

[7] G. Katona, A. Kaszás, G. F. Turi, N. Hájos, G. Tamás, E. S. Vizi, and B. Rózsa, "Roller coaster scanning reveals spontaneous triggering of dendritic spikes in CA1 interneurons," *Proceedings of the National Academy of Sciences of the United States of America*, vol. 108, no. 5, pp. 2148–2153, 2011.

[8] F. Anselmi, C. Ventalon, A. Bègue, D. Ogden, and V. Emiliani, "Three-dimensional imaging and photostimulation by remote-focusing and holographic light patterning," *Proceedings of the National Academy of Sciences*, vol. 108, no. 49, pp. 19504–19509, 2011.

[9] M. Broxton, L. Grosenick, S. Yang, N. Cohen, A. Andalman, K. Deisseroth, and M. Levoy, "Wave optics theory and 3-D deconvolution for the light field microscope," *Optics Express*, vol. 21, no. 21, pp. 25418–25439, 2013.

[10] L. Golan, I. Reutsky, N. Farah, and S. Shoham, "Design and characteristics of holographic neural photo-stimulation systems," *Journal of Neural Engineering*, vol. 6, no. 66004, 2009.

[11] G. D. L. Gregor Thalhammer, Richard W. Bowman and Miles J. Padgett and Monika Ritsch-Marte, "Speeding up liquid crystal SLMs using overdrive with phase change reduction," *Optics Express*, vol. 21, no. 2, pp. 1779–1797, 2013.

[12] J. C. Shane, D. J. McKnight, A. Hill, K. Taberski, and S. Serati, "Designing a new spatial light modulator for holographic photostimulation," 2019.

[13] C. Yalcin, N. T. Ersumo, G. Bocchetti, M. M. Ghanbari, N. Antipa, S. F. Alamouti, L. Waller, D. Lopez, and R. Muller, "19.3 A MEMS-Based Dynamic Light Focusing System for Single-Cell Precision in optogenetics," in *Digest of Technical Papers - IEEE International Solid-State Circuits Conference*, vol. 64, 2021.

[14] P. Pozzi and J. Mapelli, "Real Time Generation of Three Dimensional Patterns for Multiphoton Stimulation," *Frontiers in Cellular Neuroscience*, vol. 15, 2 2021.

[15] H. R. G. W. Verstraete, S. Wahls, J. Kalkman, and M. Verhaegen, "Model-based sensor-less wavefront aberration correction in optical coherence tomography," *Optics Letters*, vol. 40, no. 24, pp. 5722–5725, 2015.

[16] X. Zhou, H. Kapteyn, and M. Murnane, "Positive-dispersion cavity-dumped Ti: sapphire laser oscillator and its application to white light generation," *Optics Express*, vol. 14, no. 21, pp. 9750–9757, 2006.

[17] L. E. Russell, H. W. Dalgleish, R. Nutbrown, O. M. Gauld, D. Herrmann, M. Fişek, A. M. Packer, and M. Häusser, "All-optical interrogation of neural circuits in behaving mice," *Nature Protocols*, vol. 17, pp. 11579—1620, 2022.

[18] E. Ronzitti, V. Emiliani, and E. Papagiakoumou, "Methods for three-dimensional all-optical manipulation of neural circuits," 2018.

[19] A. Picot, S. Dominguez, C. Liu, I. W. Chen, D. Tanese, E. Ronzitti, P. Berto, E. Papagiakoumou, D. Oron, G. Tessier, B. C. Forget, and V. Emiliani, "Temperature Rise under Two-Photon Optogenetic Brain Stimulation," *Cell Reports*, vol. 24, pp. 1243–1253, 7 2018.

[20] G. Faini, C. Molinier, C. Telliez, C. Tourain, B. C. Forget, E. Ronzitti, and V. Emiliani, "Ultrafast Light Targeting for High-Throughput Precise Control of Neuronal Networks," *bioRxiv*, 2021.

[21] W. Shoji and M. Sato-Maeda, "Application of heat shock promoter in transgenic zebrafish," *Development, growth & differentiation*, vol. 50, no. 6, pp. 401–406, 2008.

[22] M. Tanwar, S. Kateriya, D. Nair, and M. Jose, "Optogenetic modulation of real-time nanoscale dynamics of HCN channels using photoactivated adenylyl cyclases," *RSC Chemical Biology*, vol. 2, no. 3, pp. 863–875, 2021.

Summary

Optogenetics is a powerful addition to the spectrum of techniques available in neuroscience to investigate neurophysiology and unravel how neural circuit structure is related to circuit function. This technique relies on introducing light-sensitive proteins or molecules as actuators to transduce an optical signal into a physiological perturbation of a living cell *in vitro* or in a living animal. To date, optogenetics has allowed remote control of neural activity in living and awake animals at different scales from single cells to complex networks of neurons to the investigation of animal behaviours. This wide range of experimental scales has been accomplished through joint progress on engineering the biological sensors and the optical design of instruments capable of manipulating with cellular spatial precision and millisecond temporal resolution.

The approach used in cellular-scale optogenetics experiments is to selectively photostimulate cell bodies expressing genetically-encoded actuators to trigger or silence action potentials and then record the effect of those events with fluorescent sensors. In order to mimic realistic physiology of neurons in a network, the photostimulation light needs to simultaneously excite different regions of interest, which may be separated by distances of many micrometers. For such a reason, patterning of the light via computer generated holography is often adopted as a method to produce multiple focal points. In thick tissues, photostimulation is also usually realized with ultrashort pulses of near infrared (NIR) light to excite optogenetics tools through multiphoton absorption. This nonlinear process, when focused at the target region of interest, facilitates optical sectioning, which is particularly relevant when the optogenetics tools are broadly distributed in tissue.

Despite the last decade of progress towards cellular-scale optogenetics, the application of optogenetics to sub-cellular domains remains limited. Sub-cellular optogenetics could potentially be used to investigate synapse formation and growth in developing neural circuits where axons and dendrites undergo rapid remodeling. This thesis work addresses several technological challenges to improve the optogenetics stimulation towards manipulations at the sub-cellular level. The optical tools developed are general and applicable to study physiology in any animal model, but here they are applied in zebrafish embryos.

To this end, an imaging system was developed that integrated a photostimulation module to perturb the physiology of the sample, with a light microscope to visualize the effect of those perturbations in real time. Chapter 2 describes the combination of light sheet microscopy with a stimulation module based on NIR light shaped with three dimensional computer generated holography. The characteristics of this instrument are specifically tailored to perform imaging and optogenetics stimulation in living zebrafish embryos.

One of the main challenges in designing a photostimulation module for real-time

manipulation is to be able to generate different stimulation patterns with dynamically changing target structures. For such a reason the calculation of different stimulation patterns during the experiment must be on the order of seconds. However, traditional methods such as Gerchberg-Saxton and Weighted Gerchberg-Saxton are able to provide high quality holograms with relatively high computational time, ranging from seconds to minutes. In this context, Chapter 3 presents an algorithm for calculating computer generated holograms at least 10-fold faster compared to the traditional algorithms mentioned above.

Another major difficulty posed by sub-cellular optogenetics is to focus the stimulation patterns to diffraction-limited volumes deep in tissue. Variations in the refractive index of inhomogeneous tissues distort the stimulation light traveling through it. These distortions, known as optical aberrations, will cause a loss of spatial confinement in the stimulation pattern and lower efficiency for nonlinear excitation. To tackle this issue, Chapter 4 illustrates an adaptive optics method to compensate local aberrations in stimulation patterns projected into the zebrafish tissue. The method developed is able to improve the intensity of the stimulation pattern after correction by at least two-fold.

A further aspect to consider when performing optogenetics stimulation of cellular and sub-cellular compartments in living animals is the potential harm of the stimulation light on the animal exposed to repeated irradiation. Damage induced by prolonged NIR light exposure needs to be investigated and quantified in order to assess the minimally invasive laser parameters. To this end, Chapter 5 introduces an intra-cavity dumping mode-locked laser system that offers the possibility to alter repetition rate, peak power and average power as independent experimental degrees of freedom. The effects of variable laser repetition rate and average power on both thermal damage and nonlinear damage are then characterized in zebrafish embryos.

This thesis work provides three main improvements upon the existing optical technology for all-optical interrogation of neurons *in vivo*. A faster algorithm to calculate computer generated holograms, a method to correct local aberrations in the stimulation light and, finally, minimally invasive laser parameters were defined to focus ultrashort pulses of NIR light in living animals. These methods were characterized and validated in living zebrafish brain separately but they can be used in combination to attain higher precision and flexibility in optogenetics experiments. In practice, further work is needed to improve the speed of the local aberration correction and additional upgrades to the experimental setup can be envisioned to increase the temporal resolution. Nonetheless, the optical tools developed here take the field of all-optical interrogation of neural circuits one step closer to real-time control over neuronal physiology and development.

Samenvatting

Optogenetica is een krachtige aanvulling op het bestaande aanbod van technieken dat in de neurowetenschappen wordt gebruikt om de fysiologie van neuronen te onderzoeken en te ontrafelen hoe neurale netwerkstructuur gerelateerd is aan netwerkfunctie. Deze techniek berust op het introduceren van lichtgevoelige eiwitten of moleculen als actuatoren om een optisch signaal om te zetten in een fysiologische verstoring van een levende cel, zowel in vitro als in een levend organisme. Tot heden heeft optogenetica het mojelijk gemaaht om de neurale activiteit op afstand te controleren bij levende en wakkere dieren en op verschillende schalen, van afzonderlijke cellen en complexe neurale netwerken tot het onderzoek van dierlijk gedrag . Dit brede scala aan experimentele mogelijkheden is mogelijk gemaakt door voortgang in zowel de ontwikkeling van biologische sensoren als van optische instrumenten die in staat zijn tot manipulatie met cellulaire precisie op een schaal van milliseconden.

In cellulaire optogenetica-experimenten worden cellichamen, die genetisch gecodeerde actuatoren tot expressie brengen, selectief gestimuleerd om actiepotentialen te genereren of te dempen. Vervolgens wordt het effect van die gebeurtenissen gemonitord met behulp van fluorescerende sensoren. Om de fysiologie van neuronen in een netwerk na kunnen te bootsen, moet het licht tegelijkertijd verschillende doelgebieden activeren, die op vele micrometers van elkaar af kunnen liggen. Dit wordt vaak gerealiseerd door een methode toe te passen waarbij met behulp van computergegenereerde holografie een lichtpatroon wordt gevormd om zo meerdere brandpunten voor fotostimulatie te creëren. In dikke weefsels wordt fotostimulatie gewoonlijk bereikt door optogenetische actuatoren te exciteren met ultrakorte nabij-infrarood (NIR) lichtpulsen, via een proces genaamd multifoton-absorptie. Dit niet-lineaire proces, wanneer gericht op het doelgebied van belang, vergemakkelijkt het maken van optische doorsnedes van het weefsel, wat met name relevant is wanneer de actuatoren in het gehele weefsel zijn geïntroduceerd.

Ondanks de vooruitgang in de richting van cellulaire optogenetica in het laatste decennium, blijft de toepassing van optogenetica op subcellulaire domeinen beperkt. Dit proefschrift richt zich op verschillende technologische uitdagingen in het verbeteren van optogenetische stimulatie in de richting van manipulatie op subcellulair niveau. De hier ontwikkelde optische instrumenten zijn algeemen toepasbaar voor het bestuderen de fysiologie in verschillende diermodellen, maar in dit onderzoek worden ze voor zebravisembryo's gebruikt.

Voor dit doel is een beeldvormingssysteem ontwikkeld dat beschikt over zowel een geïntegreerde fotostimulatiemodule om de fysiologie van het preparaat te verstoren, als een lichtmicroscoop om het effect van die verstoringen in realtime te visualiseren. Hoofdstuk 2 beschrijft de combinatie van lichtschijfmicroscopie (Light sheet microscopy) met een stimulatiemodule op basis van NIR-licht gevormd met

driedimensionale computergegenereerde holografie. De kenmerken van dit instrument zijn specifiek afgestemd op het uitvoeren van beeldvorming en optogenetische stimulatie in levende zebravisembryo's.

Een van de belangrijkste uitdagingen bij het ontwerpen van een fotostimulatiemodule voor realtime manipulatie is de mogelijkheid om verschillende stimulatiepatronen te kunnen genereren die voor dynamisch veranderende doelstructuren worden gebruikt. Om die reden moet de berekening van verschillende stimulatiepatronen tijdens het experiment binnen seconden gemaakt kunnen worden. Echter, traditionele methoden zoals Gerchberg-Saxton en Weighted Gerchberg-Saxton produceren hologrammen van hoge kwaliteit met een relatief hoge rekentijd, variërend van seconden tot minuten. In deze context wordt in Hoofdstuk 3 een algoritme gepresenteerd voor het 10 keer sneller berekenen van computergegenereerde hologrammen in vergelijking met de traditionele algoritmen die hierboven zijn genoemd.

Een andere grote uitdaging van subcellulaire optogenetica is om de stimulatiepatronen te concentreren op diffractiegelimiteerde volumes diep in het weefsel. Variaties in de brekingsindex van inhomogene weefsels vervormen het stimulatielicht dat er doorheen gaat. Deze vervormingen, ook wel bekend als optische aberraties, leiden tot een verlies van ruimtelijke begrenzing in het stimulatiepatroon en een verminderde efficiëntie van de niet-lineaire excitatie. Om dit probleem aan te pakken, stelt Hoofdstuk 4 een adaptieve optische methode voor om lokale aberraties in stimulatiepatronen die in het weefsel van de zebravis worden geprojecteerd te compenseren. De ontwikkelde methode is in staat om de intensiteit van het stimulatiepatroon na correctie met ten minste het dubbele te verhogen.

Een ander aspect waarmee rekening moet worden gehouden bij het uitvoeren van optogenetische stimulatie van cellulaire en subcellulaire compartimenten bij levende dieren, is de mogelijke schade aan die wordt aangericht door herhaalde blootstelling aan het stimulatielicht. Schade veroorzaakt door langdurige blootstelling aan NIR-licht moet worden onderzocht en gekwantificeerd om zo de minst invasieve laserparameters te kunnen bepalen. Hiertoe introduceert Hoofdstuk 5 een intra-cavity dumping-mode-locked lasersysteem, dat de mogelijkheid biedt om de herhalingssnelheid, het piekvermogen en het gemiddelde vermogen onafhankelijk van elkaar te wijzigen. De effecten van variabele herhalingssnelheid en gemiddelde vermogens op zowel thermische als niet-lineaire schade worden vervolgens gekwantificeerd in zebravisembryo's.

Dit proefschrift biedt drie belangrijke verbeteringen ten opzichte van de bestaande optische technologie voor het in vivo volledig optisch uitlezen van neuronen. Een sneller algoritme om computergegenereerde hologrammen te berekenen, een methode om lokale aberraties in het stimulatielicht te corrigeren en ten slotte minimaal invasieve laserparameters werden gedefinieerd om ultrakorte pulsen van NIR-licht in levende organismen te focussen. Deze methoden zijn afzonderlijk gekarakteriseerd en gevalideerd in levende zebravishersenen, maar ze kunnen ook in combinatie worden gebruikt om hogere precisie en flexibiliteit in optogeneticaexperimenten te bereiken. In de praktijk is verder onderzoek nodig om de snelheid van de lokale aberratiecorrectie te verbeteren en kunnen aanvullende upgrades van de experimentele opstelling worden overwogen om de temporele resolutie te

verhogen. Desalniettemin brengen de hier ontwikkelde optische instrumenten het vakgebied van volledig optisch uitlezen van neurale circuits een stap dichter bij realtime controle over neuronale fysiologie en ontwikkeling.

Curriculum Vitæ

Laura Maddalena was born in Teramo, Italy on 15 February 1991. She obtained her bachelor degree in Physics and master degree in Biophysics at University La Sapienza in Rome. In April 2016, she joined the lab of Prof. Maria Garcia-Parajo at the Institute of Photonic sciences (ICFO) in Barcelona for her MSc research. She contributed to the study of single receptors dynamics in living cell membranes by means of multi-color single particle tracking. Later she moved to Delft, the Netherlands, to join the lab of Prof. Nynke Dekker at the Bionanoscience department at Delft University of Technology as optics lab technician.

In May 2017, she started her PhD with Dr. Elizabeth Carroll at the Department of Imaging Physics at Delft University of Technology. Her project was about optical engineering towards the improvement of optogenetics stimulation in the living larval zebrafish brain, as described in this thesis.

Currently she is a post-doctoral researcher in the lab of Dr. Elizabeth Carroll at the Department of Imaging Physics at Delft University of Technology.

List of Publications

5. **L. Maddalena**, M. Ouwehand, H. Safdar, E.C. Carroll. *Flexible control of pulse intensity and repetition rate for multiphoton photostimulation.* Frontiers in Physics **10**(1005094), (2022)

4. **L. Maddalena**, H. Keizers, P. Pozzi, E.C. Carroll. *Local aberration control to improve efficiency in multiphoton holographic projections.* Optics Express **30**(16), 29128-29147, (2022)

3. **L. Maddalena**, P. Pozzi, N.G. Ceffa, B. van der Hoeven, E.C. Carroll. *Optogenetics and Light Sheet Microscopy.* In: Papagiakoumou E. (eds) All-optical methods to study neuronal function, To appear in Neuromethods **Vol. 191**, Humana Press, New York, NY (2022)

2. P. Pozzi*, **L. Maddalena***, N.G. Ceffa, O. Soloviev, G. Vdovin, E.C. Carroll, M. Verhaegen. *Fast Calculation of computed generated holograms for 3D Photostimulation through Compressive-Sensing Gerchberg–Saxton Algorithm.* Methods and Protocols **2**(1), 2-15, (2019).

1. I. Carmi, M. De Battista, **L. Maddalena**, E.C. Carroll, M.A. Kienzler, S. Berlin , *Holographic two-photon activation for synthetic optogenetics.* Nature Protocols **14**, 864–900, (2019)

* These authors contributed equally to this work.

Acknowledgments

Above all I want to thank my promotor Dr. ir. Jacob Hoogenboom and my co-promotor and supervisor Dr. Elizabeth Carroll for welcoming me when I joined the Microscopy Instrumentation & Techniques group, for supporting me at all times during this PhD journey. Thanks for the time you dedicated to me as a PhD student and as a person.

It was a pleasure to share with you Elizabeth the excitement of building up the Zebrafish Neurodevelopment Lab "from scratch". It was a challenging and stimulating experience. I am grateful to you for trusting me from day one as first lab member. Thanks for all your teachings and discussions during our long meetings.

Then more lab members joined: Dr. Leonie Gouweleeuw, Dr. Nicolò Ceffa, Dr. Huma Safdar, Arent Kievits and Mette Dekkers. I am thankful to them for the time spent together inside and outside the lab.

Thanks to Leonie and Huma for the help taking care of the zebrafish facility and giving trainings in the wet lab. Thanks to Nicolò for sharing your knowledge about light sheet microscopy, python programming and patisserie. Thanks for supporting the critical moments while aligning the microscope and facilitating the process by playing Ramsteins' songs. Thanks to Huma for your kindness and for being eager to share your lab and cooking skills. Thanks Arent for helping with the dutch translations of the propositions and the summary of this thesis. And especially, for the nice conversations about the music scene in the Netherlands.

I want to thank all the students that joined and are still part of the "Zebrafish Neurodevelopment Lab". I really enjoyed working with you all and from each of you I learnt something. In particular I would like to acknowledge: Sanne Thewessem, Hidde Keizers, Alexandra van Dongen and Quenteijn van Cooten. I was glad to supervise your work. This thesis would not have been the same without your dedicated collaboration. Among the students I want to thank also: Bas van der Hoeven, Quincy Buuron, Danin Dharmaperwira and Mariska Ouwehand. Thanks to you Bas, for the effort you put into the the Neuromethods book chapter and for testing the GUI to control the microscope. Thanks Quincy and Danin for giving me a hand with the sample preparation during the such long experiments. Thanks Mariska for your patience and commitment during the Western Blot experiments.

Thanks to the Brinks Lab and Maresca Lab for sharing the lab equipment and human resources in the k-wing labs.

Thanks to all the k-wing crew: Vidya, Xin, Marco, Zhenzhen, Qiangrui, Apilena, Ian, Dion, Tara and Gréta for the good company during long working days in the lab and for the happy moments shared outside the lab enjoying life. Thanks Vidya for all the nice conversations about the most diversified topics from neuroscience to music passing by art and cooking, of course. Thank you for your positive attitude which often made me seeing things from another perspective. Thanks Xin for all

the discussions about python programming and most importantly for your kindness and peacefulness that truly inspires me. Thanks Marco for being a patient office mate towards all my requirements: low noise and high temperature above all.

Thanks to all the current and previous members of the broader Microscopy Instrumentation & Techniques group: PIs, technicians, secretaries, post-docs, PhDs and students technicians and for creating a friendly and pleasant working environment. In particular I would like to thank: Han van der Linden, Aya Mahgoub, Ryan Lane, Cristiano Glessi, Ernest van der Wee and Daan Boltje. Thank you Han for being always there to help whenever an IT or electronics problem popped up. I really enjoyed all our conversations about travelling. I am fascinated by your deep knowledge of all the italian regions. Thank you Aya for sharing the PhD journey with me from day one, since we met in the corridors of the building. Since the very first moment I have been impressed by your kindness and empathy. You were a great support for me throughout those years. I am grateful for our friendship. Thank you Ryan for sharing the last mile of the PhD race, talking with you about the last refinements was very helpful and made this last period smoother and less stressful. Thank you Cristiano for all the time spent together during lunch and coffee breaks chatting about food, wines, liquors, sun and music: the Italians favourites. Thank you Ernest and Daan for sharing the PSF analysis tool it was an important resource for the work presented in this thesis.

A super huge thank you to Dr. Paolo Pozzi for the precious and fruitful collaboration over the years beyond the geographical distance. Thank you Paolo for sharing your broad knowledge about optics and the tips and tricks of computer generated holography. Thanks for introducing me to the world of adaptive optics. I really enjoyed working with you.

Another big thank to friends and relatives outside the lab.

Thanks Pamina for all our existential conversations, we have a very similar way of feeling things and I am so happy to share my thoughts and emotions with you. Thanks for keeping up our friendship besides the distance, I am very proud of it

Thanks Nicole for our weekly discussions about PhD life and struggles and about life in general, I really admire your calm attitude and your perseverance. I also enjoyed all our fun activities from ballet classes to Spanakopita workshops, I hope many more have to come :)

Grazie a Elisa & Vincenzo per essere stati una costante durante il periodo olandese, per tutte le risate spensierate assieme durante le nostre cenette superlative piene di prodotti a Km 1600. Spero di condividere con voi altrettanti bei momenti, magari riducendo le distanze un giorno.

Grazie a Betta per il tuo entusiasmo e per le tue parole sempre positive, ogni volta che parliamo o spendiamo tempo assieme è un'esperienza rigenerante.

Grazie agli amici di tarebook, gli amici di una vita ormai: Angela, Albano, Panda, Anna e Riccardo. Con ognuno di voi ho un rapporto diverso ma con ognuno di voi mi sento a casa anche se in questi anni ci siamo sempre visti al di la' delle Alpi. Grazie per esserci sempre, sia per le risate leggere che per un conforto.

Grazie a Francesca per tutte le chiacchierate e le risate da sedici anni a questa parte. Grazie per la bellissima copertina realizzata per questa tesi e per la pazienza

con cui hai soddifatto le mie richieste.

Grazie a Isa per essere un punto di riferimento costante nella mia vita indipendentemente dalla latidudine geografica. Grazie per tutti i bei momenti vissuti assieme sin dagli indimenticabili e pazzi anni a viale Ippo 76. Grazie per tutte le tue premure e il tuo affetto incondizionati.

Grazie alla famiglia Guardiani allargata: Nilla & Mario, Nico,Aziz & Daria, Leo & Cons. Ormai siete per me una seconda famiglia.

Grazie alla mia famiglia: nonna Maria, zia Tetta, zii e cugini, per tutto l'amore incodizionato da quando sono nata. Vi voglio tanto bene!

Grazie a Mamma e Papà, per avermi cresciuto nel migliore possibile dei modi, per avermi insegnato la dedizione verso gli impegni e la curiosita'.

Grazie al mio compagno di vita Antonio, per tutto l'amore e la stima che mi dimostri ogni giorno. Grazie per avermi supportato e sopportato durante tutta la durata del dottorato, in particolare per tutti i weekend che ho passato in lab e per aver spesso adattato i tuoi tempi a quelli degli zebrafish.

Thank you, Bedankt, Grazie to you all: my PhD experience would not have been the same without all the different people I met during those years, you were an important addition and enrichment to my life!